In The Name of God

Journal of
Interfaces, Thin Films and Low dimensional systems

Volume 4, Issue 1, Summer and Autumn, 2020

Publisher: **Alzahra University**

Contents

Journal of Interfaces, Thin films, and Low dimensional systems 4 (1) Summer and Autumn (2020) 311-322

The effect of hydrostatic pressure on the radiative recombination rate of InGaN/GaN multiple quantum well solar cells

Scientific research paper

Rajab Yahyazadeh*, Zahra Hashempour

Department of Physics, Khoy Branch, Islamic Azad University, Khoy, Iran

ARTICLE INFO

Article history:
Received 3 May 2021
Revised 28 May 2021
Accepted 5 August 2021
Available online 22 October 2021

Keywords:
Recombination rate
Solar cell
Optical absorption
Multi-quantum well

ABSTRACT

In this paper, a numerical model is used to analyze photovoltaic parameters according to the electronic properties of InGaN/GaN multiple-quantum-well solar cells (MQWSC) under hydrostatic pressure. Finite difference techniques have been used to acquire energy eigenvalues and corresponding eigenfunctions of InGaN/GaN MQWSC, where all eigenstates are calculated via a 6×6 k.p method under an applied hydrostatic pressure. All symmetry-allowed transitions up to the fifth subband of the quantum wells (multi-subband model) with barrier optical absorption are considered. The linewidth due to the carrier-carrier and carrier-longitudinal optical (LO) phonon scattering are also considered. A change in pressure up to 10 GPa increases the intraband scattering time up to 38 fs for heavy holes and 40 fs for light holes. The raise in the height of the Lorentz function reduces the excitonic binding energy and decreases the radiative recombination rate up to $0.95\times10^{25}\mathrm{cm}^{-3}\mathrm{s}^{-1}$. The multi-subband model has a positive effect on the radiative recombination rate.

1 Introduction

Recently, indium gallium nitride alloys have attracted much attention for optoelectronic applications [1–4] due to their tunable energy bandgap varying from 0.7 eV to 3.4 eV [5-6]. The absorption range covers a significant portion of the solar spectrum, making InGaN a promising candidate for multi-junction solar cell systems. Moreover, with high radiation resistance, thermal stability, and chemical tolerance, InGaN solar cells could operate in extreme conditions [7]. The temperature and polarization dependence are considered preeminent tools in evaluating optical and electronic characteristics in III-V nanodevices (e.g., solar cells and transistors) [8,9]. The optical absorption coefficients are one of the significant parameters in calculating the recombination rate in InGaN/GaN Multi-quantum solar cell. Therefore, to study the recombination rate in detail, we must calculate the absorption coefficients in InGaN/GaN MQWSC. The effect of alloy on InGaN/GaN MQWSC has been investigated by Deng et al. [10]. Also, the temperature effect on InGaN/GaN MQWSC has been studied by Belghouthi et al. [11] where its efficiency in different wells and temperatures has been considered by Chouchen et al. [12]. In all these studies, a simple analytical relation of quantum well absorption coefficient has been used to obtain the electrical and electronic characteristics; however, the role of quantum barrier absorption coefficient has still not been taken into account. Also, in our previous work [13], the absorption coefficient of quantum wells has been

*Corresponding author.
Email address: Rajab.yahyazadeh@iaukhoy.ac.ir
DOI: 10.22051/jitl.2021.35972.1053

calculated for the first subband transition without considering other subbands. We had not considered the effect of barrier optical absorption, three-dimensional exciton binding energy, and the linewidth due to the carrier-carrier and carrier-longitudinal optical (LO) phonon scattering under external disturbances. This paper aims to perform these corrections under an external perturbation (e.g., hydrostatic pressure). In solar cells with a single-quantum well in the intrinsic region, due to the low absorption coefficient of second- and higher-order subbands, these energy transitions are not very effective in the recombination rate; however, in multi-quantum wells in the intrinsic region, the second-and higher-order transitions significantly affect the recombination rate due to more quantum wells. The linewidth function (Lorentz function) is one of the most important functions for calculating optical parameters, such as optical absorption coefficient and gain. The optical absorption coefficient is one of the significant parameters in calculating photocurrent density in the InGaN/GaN Multi-quantum solar cell. The Lorentz function also depends on the scattering time and the transition energies. In all the work done on solar cells, this transition time under external perturbations is fixed and often considered to be 0.1ps; in the present study, we examine its dependence on pressure. The most important advantage of this numerical method and the aspect of innovation in this work is the use of five important parameters, including effective mass, energy gap, lattice constants, dielectric constant and quantum barrier, and well thickness, all of which are simultaneously dependent on hydrostatic pressure and temperature. We also consider the effect of hydrostatic pressure on the energy of heavy and light holes and the transition energy of the subbands. In this model, the conduction band energy, wave functions, and energy subbands are obtained from the self-consistent solution of the Schrodinger and Poisson equations. The hole valance bands (heavy and light hole) energy, wave functions, and energy subbands are calculated using a 6×6 k.p method. The sample used in the modelling is the p–i–n solar cells with an InGaN/GaN MQWSC structure within the i-region. The p and n regions are based on GaN. The donor and acceptor concentrations in the n- and p-region materials are assumed to be equal to $0.1\times10^{18}cm^{-3}$, and 10 wells are considered in the present work. It should be notified that the calculated built-in polarization field for the structures is about $\sim10^{8}Vm^{-1}$. In the present study, atmospheric and hydrostatic pressures are taken into account, i.e., at zero hydrostatic pressure only the atmospheric pressure is applied. The results and discussions are obtained by calculating and drawing the figures.

2 Calculation Model

2.1 Self-consistent solution of Schrödinger-Poisson equations

The quantum well solar cell (QWSC) consists of a multiple quantum well structure in the intrinsic region of a p–i–n. The MQW structure introduced for the model is constructed by $In_mGa_{1-m}N$ with lower indium molar fraction (m=0.5) for wells and m=0.4 for barriers, as shown in Fig. 1. To obtain accurate values for Fermi energy, the energies of quantized levels within the two-dimensional electron gas (2DEG), potential profiles, wave function, and the sheet carrier concentration for the 2DEG in InGaN/GaN heterostructures for both Schrodinger and Poisson equations must be solved. This is achieved by solving Schrodinger's equation and simultaneously taking into account the electrostatic potential obtained from Poisson's equation, as well as the image and exchange-correlation potentials using the three-point finite difference method [14]. In the Schrodinger equation, eF_zz is the potential energy induced by the polarization charges, F_z is the electric fields in the well, F_w, and barrier, F_b, caused by the spontaneous (SP) and piezoelectric (PZ) polarization [15-17]. In this work, five parameters, including effective mass, energy gap, lattice constants, dielectric constant and quantum barrier, and well thickness are used which are simultaneously dependent on the hydrostatic pressure and temperature as follows:

1- The basal strain represented as of the form $\grave{o}(T,P,m)=\left(a_s-a_e(T,P,m)\right)/a_e(T,P,m)$ is expressed from the lattice of the substrate a_z and the epilayer $a_e(T,P,m)=a_0(m)\left[\left(1+\beta\left(T-T_{ref}\right)\right)\left(1-P/3B_0\right)\right]$. The lattice constants, as a function of temperature, indium molar fraction and the hydrostatic pressure [18-20], where $B_0=239GPa$ is the bulk modulus of sapphire, $\beta_{GaN}=5.56\times10^{-6}K^{-1}$ is the thermal expansion coefficient at $T_{ref}=300K$, $a_0(m)=0.13989m+0.03862$ is the equilibrium lattice constant as a function of the indium molar fraction [19,20].

2- Here $\mathcal{E}_{GaN}(T,P)$ and $\mathcal{E}_{InGaN}(m,T,P)$ are the dielectric constants of GaN and InGaN while $L_{In_mGa_{1-m}N}(T,P)$ and L_{GaN} are respectively the thickness of InGaN and GaN as given by [20]:

$$\varepsilon_{GaN}(T,P)=10\times\exp\left(10^{-4}\left(T-T_0\right)-6.7\times10^{-3}P\right) \quad (1)$$

$$\varepsilon_{InGaN}(m,T,P)=\varepsilon^{GaN}(T,P)+6.4m \quad , \quad (2)$$

$$L_b = L_{In_mGa_{1-m}N}(T,P) = L_{InGaN}(0)\left[-\left(S_{11}^{In_mGa_{1-m}N} + 2S_{12}^{In_mGa_{1-m}N}\right)P\right], \quad (3)$$

$$L_w = L_{GaN}(T,P) = L_{GaN}(0)\left[-\left(S_{11}^{GaN} + 2S_{12}^{GaN}\right)P\right] . \quad (4)$$

Here, $L_{InGaN}(0)$ and $L_{GaN}(0)$ are the InGaN and GaN layers thickness without hydrostatic pressure and temperature. S_{11} and S_{12} are the elastic compliance constants.

3-The band gap energy of InGaN/GaN is as follows [15, 18, and 20]:

$$E_g(T,P) = E_g(0,0) + \gamma P + \sigma P^2 + \left(\alpha T^2\right)/(T + T_e) , \quad (5)$$

where $E_g(0,0)$ stands for the band gap energy of GaN or InGaN in the absence of the hydrostatic pressure at temperature 0K. The suggested parameters used in Eq. (5) have been taken from Ref 24. In this work the parameters α, σ, γ etc. are independent of the electron concentration.

4-In the Schrödinger equation the electron effective mass m^* can be written as [21]:

$$\frac{m_0}{m_e^*(P,T,m)} = 1 + \frac{E_P^{\Gamma}\left(E_g^{\Gamma}(P,T,m) + 2\Delta_{S0}/3\right)}{E_g^{\Gamma}\left(E_g^{\Gamma}(P,T,m) + \Delta_{S0}\right)} , \quad (6)$$

where m_0 is the free electron mass, E_P is the energy linked to the momentum matrix element, Δ_{S0} is the spin-orbit splitting, and $E_g^{\Gamma}(P,T,m)$ is the band gap variation as a function of the hydrostatic pressure and temperature. The whole wave functions and energy subbands are calculated along the z-axis using a $\times 6$ k.p method [22,23].

The optical absorption expression as a function of the photon energy E' is calculated as [24,25]:

$$\alpha_W(E') = \frac{\pi\hbar q^2}{E'\varepsilon_0 m_0^2 c n_{eff}} \times \sum_{i,j}^{n} \int_{E_{g,w}}^{g,b} D_{r,ij}^{2D} |Mij|^2 \left(f_{i_v} - f_{j_c}\right) L\left(E' - E_{ij}\right) dE_{ij}, \quad (7)$$

where q and c are respectively the electron charge and light vacuum speed; i and j are respectively the conduction and valance subband number.

$L\left(E' - E_{ij}\right) = \left(\Gamma_{hom}^2\right)/2\pi\left[\left(E' - E_{ij}\right)^2 + \Gamma_{hom}^2\right]$ is the Lorentzian function, $D_r^{2D} = m_{r,ij}/\left(\pi\hbar^2 W\right)$ is the reduced density of the allowed transition of each subband while $|M_{ij}|$ represents the transition strengths. These three parameters are important in optical absorption. The Lorentz function depends on parameters Γ_{hom} and E_{ii}, where Γ_{hom} represents the linewidth of the conduction and the valance bands that is related to scattering of all carriers (electrons, light, and heavy holes) and phonons (see Appendix A) [26,27]. The intraband relaxation time τ_{in} is obtained from Eqs. (A1) and (A4) as $\hbar/\tau_{in} = \Gamma_{cjk_\square}(E) + \Gamma_{vjk_\square}(E)$. Another effective parameter regarding the Lorentz function is $E_{ij} = E_i^e + E_j^h + E_g^{GaN} - E_b^{ij} - eF_W L_W$ [28]. That is the transition energy of the electron from the conduction band to the valance band, where E_i and E_j are respectively the subband energy of the electron and holes in the triangular quantum well while E_b is the bounding energy of excitons which is dependent on external perturbations such as pressure and temperature through electron and hole effective masses [28-30]. Exciton energies are determined by employing a variational procedure [31]. Restricting ourselves to the analysis of s-like excitons implies the proposal of a normalized trial wavefunction, $|\Psi_x\rangle$, built from the product of uncorrelated electron and hole subband states together with the inclusion of a hydrogenic-s-like factor [32-34]. Then, the exciton energy is obtained by minimizing the functional $E_x = \langle\Psi_x|H_x|\Psi_x\rangle/\langle\Psi_x|\Psi_x\rangle$ where $H_x = H_e + H_{hh,lh} + H_\perp$ is the exciton Hamiltonian that includes the electron one-band Hamiltonian from the Schrodinger equation (H_e), the heavy and light hole six-band Hamiltonian from the K.P model $(H_{hh,lh})$, and the electron-hole interaction Hamiltonian $(H_\perp)$ [31-34]. The binding energy of the s-like exciton resulting from the coupling of the electron in the i-th subband and the hole in the j-th subband is then given by $E_b^{ij} = E_i^e + E_j^h - E_x$ [31]. The carrier effective mass in the i-th sub band can be calculated as follows [35,26]

$$\frac{1}{m_i^*} = \frac{1}{m_b^*}\left[1 - P_{iw}\right] + \frac{1}{m_w^*}P_{iw} , \quad (8)$$

where m_b^* and m_w^* are the barrier and well carrier effective masses, $P_{iw} = P_{iw}(\psi_{iw})/\left(P_{ib}(\psi_{ib}) + P_{iw}(\psi_{iw})\right)$ is the probability of finding an electron in the quantum

well at the level with energy E_i. $P_{iw}(\psi_{iw}) = \int_0^{d_{GaN}} dz|\psi_{iw}|^2$ and $P_{ib}(\psi_{ib}) = \int_{-d_{InGaN}}^{0} dz|\psi_{ib}|^2$ respectively represent the wave function of the electron in the i-th subband and the wave function penetrating towards the quantum barrier. The value of the penetrating wave function in the barrier $(P_{ib}(\psi_{ib}))$, is the criterion for calculating the quantum confinement that is effective on the effective masses of the carriers in subbands. The effective masses of light and heavy holes are obtained using the ×6 k.p method [36]. The numerical values of the valance band effective mass parameters (Ai) and deformation potentials (Di) are taken from reference [21]. By determining the effective masses of carriers in quantum wells, through ternary formula $1/m^*_{In_xGa_{1-x}N} = \left((1-x)/m^*_{InN}\right) + x/m^*_{GaN}$, the effective masses in $m^*_{In_xGa_{1-x}N}$ barriers can be obtained [37]. By determining the effective mass of the electron in the i-th conduction subband and the effective mass of the hole in the j-th valance subband, the reduced effective mass $m^{*-1}_{r,ij} = m_i^{-1} + m_j^{-1}$ can be calculated. As a result, the reduced density of the allowed transition can be calculated where W is the thickness of quantum well. The transition matrix element $|M|^2$ is a measure for the strength of stimulated electron transitions in a given material. This strength does not depend on the direction of the intraband transition; it is the same for emission and absorption. However, the transition strength does depend on the angle between the electron wave vector $\vec{k}$ and the optical field vector $\vec{E}$. Any polarization direction of the optical field encounters a variety of electron $\vec{k}$ vectors that needs to be averaged at the given photon energy. For bulk zinc blende semiconductors, averaging over all possible $\vec{k}$ vectors results in an isotropic transition matrix element that is equal to the momentum matrix element given by $M_b = (m_0 E_p)/6$ [25]. E_p, is the energy parameter whose numerical value is given in Table One. For quantum well structures, the transition matrix element is anisotropic while the absorption coefficient depends on the optical polarization. Commonly, one distinguishes two polarization modes, in which either the electric field (TE mode) or the magnetic field (TM mode) lies within the quantum well *xy*-plane (transversal plane). The compression strain increases the mean band gap and splits the degeneracy of the valence band maximum and introduces an anisotropic valence band structure. Note that the highest band is now heavy along, $k_\perp$, the strain axis (growth direction) with light holes along $k_\parallel$. Consequently, the light beam has TE mode. The transition strengths of the TE mode are different for heavy (hh) and light holes (lh) Which are calculated as [25, 38]

$$\left|M^{TE}_{e-hh}\right|^2 = \left(3+3\cos^2(\theta_e)\right)C_{ij}\left|M_b^2\right|/4, \quad (9)$$

$$\left|M^{TE}_{e-lh}\right|^2 = \left(5-3\cos^2(\theta_e)\right)C_{ij}\left|M_b^2\right|/4, \quad (10)$$

where $\cos(\theta_e) = E_{ij}/E'$ is the angular factor. $C_{ij} = \int \psi_i^*(x)\psi_j(x)dx$ is the electron-hole overlap integral. For the TM mode, the relationships are similar to Eqs. (17) and (18), except that the inside of the parentheses in Eq. (8) is $3-3\cos^2(\theta_e)$ (for heavy holes) and $1+3\cos^2(\theta_e)$ (for light holes). It should be noted that due to the finiteness of the quantum barriers, the orthogonal condition in the overlap integral as well as selection rule (i=j) is no longer imposed as all symmetry-allowed transition are considered. $f_{i_c} = 1/1+\exp\left(E_{i_c} - E_{f_c}\right)/k_bT$ and $f_{j_v} = 1/\left[1+\exp\left[\left(E_{j_v} - E_{f_v}\right)/k_bT\right]\right]$ are the Fermi-Dirac distribution for electrons in the i-th subband of the conduction bands and holes in the j-th subband of valance bands, respectively. E_{i_c} and E_{j_v} are the quantized electron and hole energy levels, respectively. E_{f_c} and E_{f_v} are the electron and hole quasi-Fermi levels, respectively. Finally, Adach's refractive index model for $In_mGa_{1-m}N$ is given by [25]:

$$n_{eff} = \sqrt{A\left(\hbar\omega/E_g\right)^{-2}\left\{2-2\sqrt{1+\left(\hbar\omega/E_g\right)}\right\}+B}. \quad (11)$$

Here $A = 9.827(1-m)-53.57m$ and $B = 2.736(1-m)-9.19m$ are alloy-dependent parameters that are true for $m<0.38$. The absorption coefficient of the quantum barrier for continuous states is as follows [42]:

$$\alpha_B(E') = \frac{e^2|\hat{e}\cdot\vec{p}_{cv}|^2}{n_{eff}c\varepsilon_0 m_0 E' R_y a_0^3} \times \left(\int_{E_g^{In_{0.4}Ga_{0.6}N}}^{\infty} \frac{d\varepsilon'}{1-\exp\left(-2\pi/\sqrt{\varepsilon'}\right)} \frac{\Gamma_{\text{hom}}}{(\varepsilon-\varepsilon')^2+\Gamma^2_{\text{hom}}}\right), \quad (12)$$

where R_y and a_0 are the exciton Rydberg energy and Bohr radius, respectively, $\varepsilon = \left(E'-E_g\right)/R_y$ is the normalized energy measured from the bandgap, and

$\left|\hat{e}.p_{cv}\right|^2 = m_0 E_p/6$ is the momentum-matrix element of the bulk quantum barrier. The radiative recombination rate is given by [43]:

$$U_{rad} = B_{rad}(np - n_i^2)\,. \tag{13}$$

Here n and p are the densities of electrons and holes in the conduction and valance bands, respectively, while n_i is the intrinsic densities of the carriers. The recombination coefficient depends on the absorption coefficient is calculated from the following equation

$$B_{rad} = \frac{2\pi}{n_i^2 h^3 c^2}\int_{E_g^{11}}^{\infty} n_{eff}^2\,\alpha(E)e^{-E/k_B T}E^2 dE\ . \tag{14}$$

If we calculate B_{rad} in a quantum barrier or well, we put their absorption coefficients in Eq. (14). The lower limits of the integral, n_i and n_{eff}, are also functions of the quantum barrier and well areas. The exponential term means that, relative to absorption, the contribution from the energy level closer to the band edge is much more important.

3 Results and Discussion

In this paper, a numerical model is presented to calculate the optical parameters of InGaN/GaN MQW Solar Cells (MQWSC) in order to investigate the effect of hydrostatic pressure. The Schrodinger and Poisson differential equations are solved by the finite difference method. Regarding the self-consistent solution of Schrodinger-Poisson equations, the iterative method mentioned in Refs. [39] and [40] is used. The convergence is obtained when the difference on the Fermi level associated with two consecutive iterations ($E_{F(n)} - E_{F(n-1)}$) is smaller than $10^{-4}eV$; also, during the calculations, the same grid mesh is used for both Poisson and Schrödinger equations. The hole eigenstates are calculated along the z-axis using a $\times 6$ k.p method. Figure 1 shows the dependence of the conduction band offset, the bandgaps of InGaN, and GaN on the hydrostatic pressure. The increase in the hydrostatic pressure with a range of 0-10Pa leads to increased conduction band offset. This is attributed to an increase in the bandgap energy of GaN and InGaN with increased hydrostatic pressure. This phenomenon is related to the correction of the atomic distances of the crystal lattice by external pressure, leading to a change in polarization. Conduction and valance bands with the location of quantum wells (electrons and holes), as well as valance bands for light and heavy holes, are shown in Fig. 2. The optical absorption equation is proportional to the spatial overlap of electron-hole wave functions, $C_{ij,P}$ (P = 0, 5, 10), with 0 corresponding to the device under no pressure. The overlap regarding different pressures relative to $C_{ij,0}$ is extracted and plotted for the first and second subbands in Fig. 3. As can be seen, the increase in the pressure decreases the spatial overlap while it increases the depth of quantum wells. Increased depth of the wells leads to increasing the electron and hole densities while decreasing the propagation of the wave functions (electrons and holes). As a result, the quantum confinement increases and decreases the overlap. The Lorentz function is one of the most influential parameters in the optical absorption equation in addition to its shape. To examine this function in detail, the pressure dependence of the conduction and valance linewidths is calculated, as illustrated in Figs. 4 and 5, respectively. In particular, line widths have a decreasing trend with increasing pressure. This is since the spatial separation of wave functions decreases with increasing carrier density. In the case of scattering carriers with phonons (electron-phonon, heavy hole-phonon, light hole-phonon), the decrease in linewidths is due to decreasing the term related to the Fermi function in the second term in the square bracket of Eq. (A4). The difference between the subband energy and the Fermi energy increases with increasing hydrostatic pressure, resulting in the decrease in the term related to the Fermi function. A reduction in the linewidths of the conduction and the valance bands increases the intraband relaxation time between the electrons and the light and heavy holes, as shown in Fig. 6, due to the inverse relationship of intraband relaxation time with linewidths. According to Fig. 6, an increase in the pressure by 10 GPa changes the relaxation time to a mean of 38fs for heavy holes and 40fs for light holes. These changes are taken into account in the calculation of the Lorentz function. At zero pressure for heavy holes, this value is equal to 0.97 ps, approximately 0.1ps. In the calculations of other studies (mentioned in the introduction) under changes such as barrier width, well width, various barrier alloys, and external perturbation, this value is considered constant and equal to 0.1ps. Transition energy is an effective parameter in calculating the Lorentz function, which also depends on the exciton binding energy and the subbands energy of the quantum wells. To better show the changes in these parameters, the second and third subbands are illustrated; however, in the calculations, symmetric-allowed transitions up to the fifth subband are entered. Of course, it should be noted that the first and second subbands have the greatest effect (due to their high density). The binding energy of excitons as a function of hydrostatic pressure is shown in Fig. 7. As seen Fig. 7, the decrease in the binding energy of excitons dependence with increasing pressure can be explained by the band offset and the internal

electric fields (F_w and F_b). With increasing pressure, the spontaneous and piezoelectric polarization increase, increasing the internal electric fields. The electric fields separate the electron and holes in the opposite direction, which reduces the overlap of electron and hole wave functions (Fig. 3), thus decreasing the binding energy of excitons. As the pressure increases, the band offset increases (Fig. 1), which expands the distance between the electrons and holes, thus reducing the Coulomb interaction. It also increases the depth of quantum wells, electron density, and quantum confinement, thus ultimately reducing the exciton binding energy. By determining the energy of the subbands related to the carriers and the binding energy of excitons, the transition energy of the carriers can be calculated, as shown in Fig. 8. According to the figure, with increasing pressure, the transition energies increase. By determining the transition energies and the linewidths of the carrier, the Lorentz function for light and heavy holes of all symmetry-allowed transitions can be obtained. For example, the Lorentz function of the first subband transition corresponding to light and heavy holes is plotted in Fig. 9. According to Fig. 9, with increasing pressure, the height of the Lorentz function increases while its width decreases. They shift to higher energies as the pressure increases. As the pressure increases to 10, the height of the Lorentz function increases to $27eV^{-1}$ for heavy holes and $16eV^{-1}$ for light holes. This increase, along with the decrease in width, is related to the decrease in linewidths, as illustrated in Figs. 4 and 5. The Lorentz function transfer to high energies is associated with the increase of transition energies with increasing pressure. By determining the Lorentz and the overlap function, as well as other parameters, the well absorption coefficient in terms of wavelength is plotted in Fig. 10. In Fig. 10, the well absorption coefficient of other electronic transitions is also considered. The pressure effect on the absorption coefficient of quantum wells is illustrated. According to Fig. 10, the absorption coefficient decreases by increasing pressure, which is related to the increase in the energy gap. Light holes have more energy gaps than heavy holes; thus, they have less absorption. Consequently, the smaller peak corresponds to a light hole.

Table 1. Suggested parameters for GaN and InN

Parameters(unit)	GaN	InN	References
$\mathbf{E_P^{\Gamma}(eV)}$	14.0	14.5	[21]
$\mathbf{E_g^{\Gamma}(0K=0GPa)(eV)}$	3.42	0.7	[21]
$\mathbf{\Delta_{s0}(eV)}$	0.014	-0.001	[21]
$\boldsymbol{\gamma}\mathbf{(meV.GPa^{-1})}$	31.8	16	[19]
$\boldsymbol{\delta}\mathbf{(meV.GPa^{-2})}$	-0.23	-0.02	[19]
$\mathbf{S_{11}(10^{-2}GPa)}$	0.55	1.15	[16]
$\mathbf{S_{12}(10^{-2}GPa)}$	0.19	0.46	[16]
$\boldsymbol{\alpha}\mathbf{(10^{-3}eV.K^{-1})}$	0.909	0.245	[21]
$\mathbf{T_e(K)}$	830	624	[21]
$\boldsymbol{\varepsilon_{\infty}}$	5.39	6.7	[44]

The absorption coefficient of a bulk quantum barrier in terms of wavelength at different pressures is shown in the inset. In this figure, there are two peaks but very close to each other, which is due to the proximity of the energy levels of the light and heavy holes at the band adage $k_{\|}$ (unlike GaAs degenerated in $k_{\|}$). Also, the absorption coefficient decreases with increasing pressure. The reason is the same as for the decrease in the absorption coefficient of the quantum well and is related to the increase in the energy gap. By determining the absorption coefficients, the recombination coefficients can be calculated, as observed in Fig. 11. In Fig. 11, the recombination coefficients according to Eq. (14) are dependent on the absorption coefficients. Therefore, with increasing pressure, the recombination coefficients decrease as the adsorption coefficients decrease. The main reason for this decrease is related to the increase in the depth of quantum wells and quantum confinement. As the pressure increases to 10 Gpa, the recombination coefficients decrease to $0.5\times10^{10}cm^3s^{-1}$ for quantum wells (B_w) and $0.4\times10^{10}cm^3s^{-1}$ for quantum barriers (B_b). Finally, the radiative recombination rate in terms of the distance at different pressures is illustrated in Fig. 12. In Fig. 12, the radiative recombination rate decreases with increasing pressure, which is also related to the decreasing changes of the recombination coefficient with increasing pressure. As the pressure increases by an order of magnitude, the radiative recombination rate decreases by an average of $0.95\times10^{25}cm^{-3}s^{-1}$.

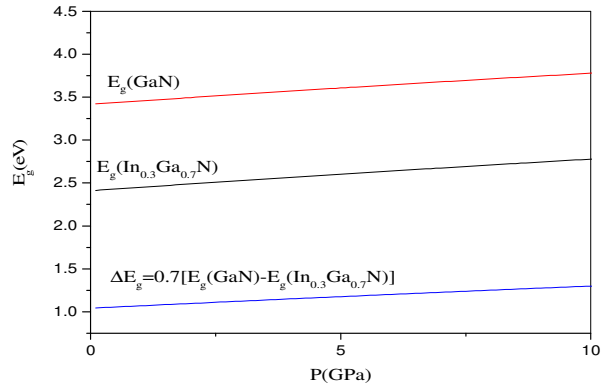

Figure 1. Bandgaps energy of InGaN, GaN, and conduction band offset of InGaN/GaN MQW solar cell as a function of pressure.

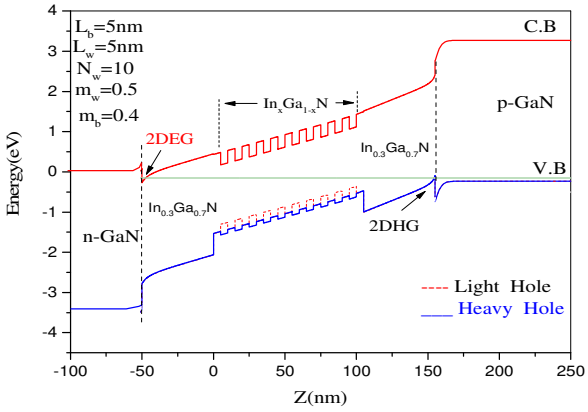

Figure 2. The conduction (C.B) and valance(V.B) bands energy of InGaN/GaN MQW solar cell as a function of the distance under different hydrostatic pressure.

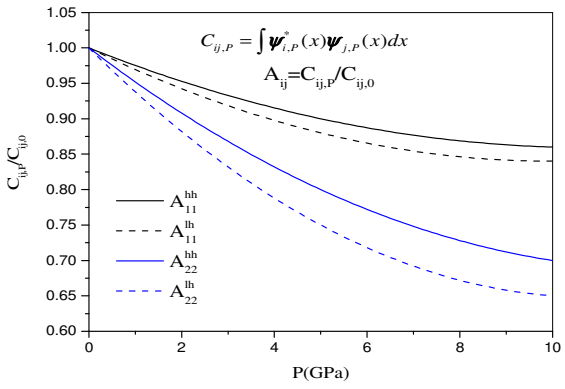

Figure 3. Normalized overlap of the electron–hole wave functions versus hydrostatic pressure. for InGaN/GaN MQW solar cell..

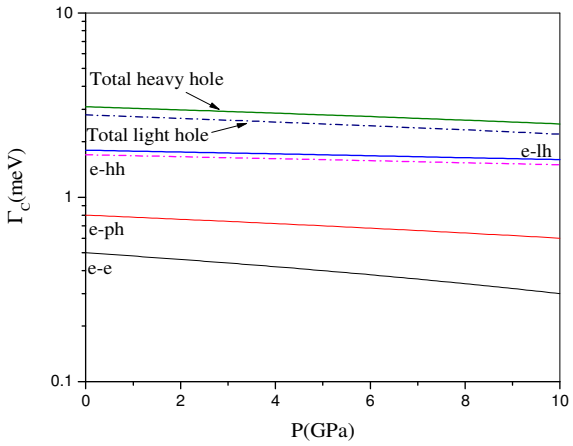

Figure 4. Conduction band linewidths as a function of hydrostatic pressure at subband adage $k_{\parallel}$ for InGaN/GaN MQW solar cell. In which all the scattering of electrons with other electrons (e-e), phonons (e-ph), light holes (e-lh) and heavy hole (e-hh) are considered.

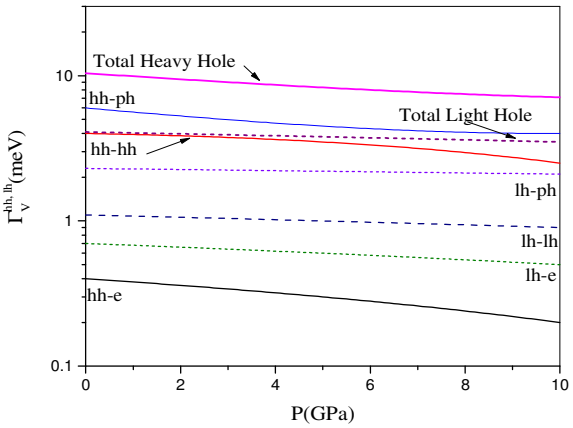

Figure 5. Valance band linewidths as a function of hydrostatic pressure at subband adage $k_{\parallel}$ for InGaN/GaN MQW solar cell. In which all the scattering of holes with other holes (hh-hh, lh-lh), phonons (lh-ph, hh-ph) and with other electrons (e-hh, e-lh) are considered.

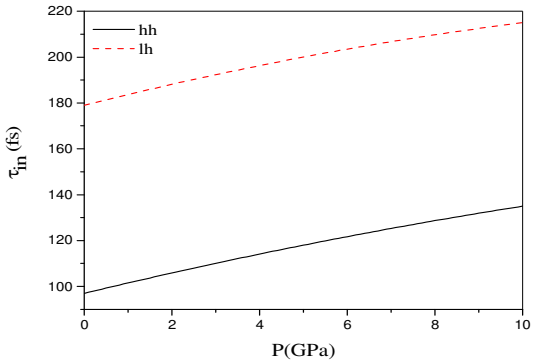

Figure 6. Intraband relaxation time as a function of hydrostatic pressure at subband adage $k_{\|}$ for InGaN/GaN MQW solar cell. In which heavy hole (solid line) and light hole (dashed line) are considered.

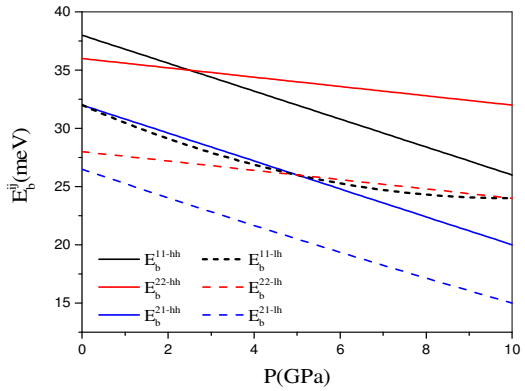

Figure 7. Exciton Binding energy of heavy holes and light holes as a function of hydrostatic pressure for InGaN/GaN MQW solar cells.

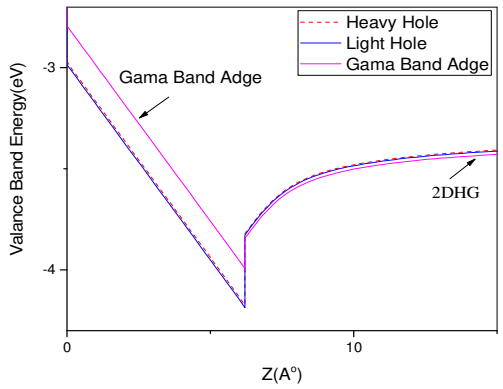

Figure 8. Transition energy as a function of hydrostatic pressure at subband adage $k_{\|}$ for InGaN/GaN MQW solar cell. In which heavy hole (solid line) and light hole (dashed line) are considered.

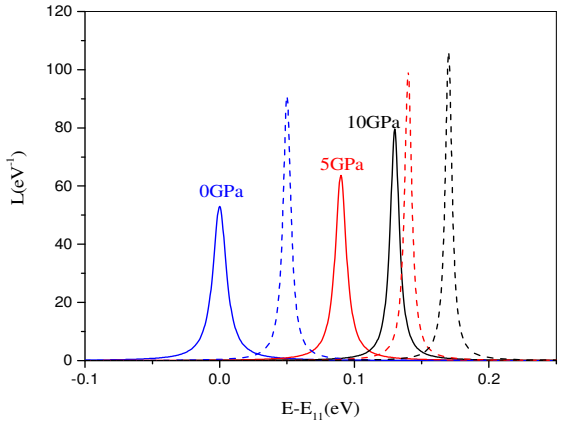

Figure 9. Heavy hole (solid line) and light hole (dashed line) Lorentzian function versus of the energy difference $(E - E_{11})$ under different hydrostatic pressures for InGaN/GaN MQW solar cell, In which the energy transition between the first subbands of electron energy levels with holes are considered.

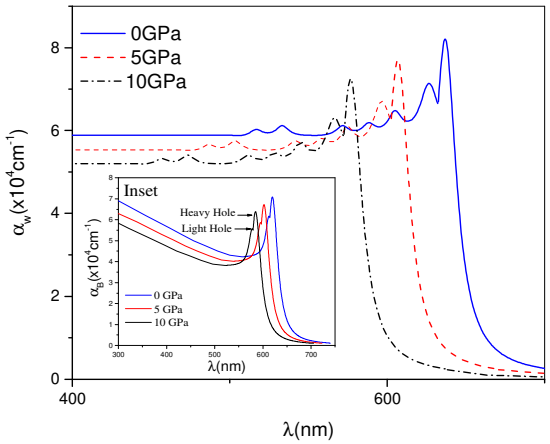

Figure 10. Quantum well optical absorption versus wavelength under different hydrostatic pressures for InGaN/GaN MQW solar cell. Inset: Quantum barrier optical absorption versus wavelength under different hydrostatic pressures for InGaN/GaN MQW solar cell.

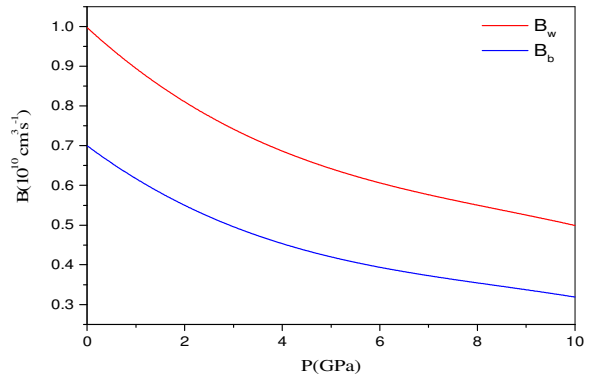

Figure 11. Recombination coefficients versus different hydrostatic pressures for InGaN/GaN MQW solar cell.

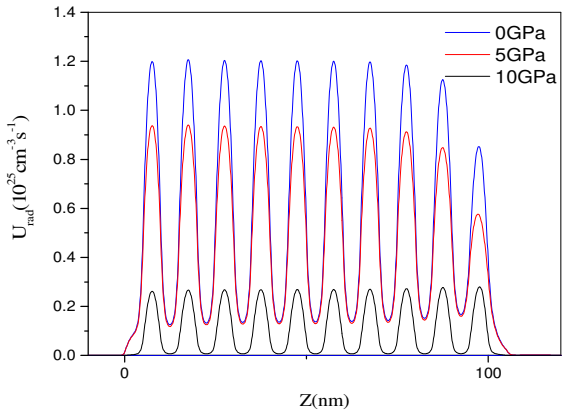

Figure 12. Radiative recombination rate of InGaN/GaN MQW solar cell as a function of the distance under different hydrostatic pressure.

4 Conclusions

In this study, we examined the optical absorption spectrum, absorption coefficient, and radiative recombination rate of InGaN/GaN multi-quantum-well solar cells (MQWSC) under hydrostatic pressure. The results showed that increasing the hydrostatic pressure in the range of 0-10 GPa would lead to an increase in (I) the intraband relaxation time up to 38fs for heavy holes and 40fs for light holes and (II) the height of the Lorentz function to $27eV^{-1}$ for heavy holes and $17eV^{-1}$ for light holes, as well as a reduction in (III) the overlap of normalized wave functions and excitonic binding energy (IV) the recombination coefficients to $0.5\times10^{10}cm^3s^{-1}$ for quantum wells and $0.4\times10^{10}cm^3s^{-1}$ for quantum barriers and (V) the radiative recombination rate up to $9.5\times10^{25}cm^{-3}s^{-1}$. Therefore, it can be concluded that all effective transitions of quantum wells should be considered for an accurate study of radiative recombination rate. Also, the absorption coefficient of a bulk quantum barrier is effective in obtaining an accurate radiative recombination rate.

Acknowledgements

The authors would like to thank Khoy Branch (Islamic Azad University) for the financial support of this research, which is based on the research project contract.

Appendix A: Intraband Relaxation Time

The linewidth due to the carrier-carrier scattering is obtained from the perturbation expansion of one-particle Green's functions. The linewidth for carrier-carrier scattering is given by:

$$\begin{aligned}&\Gamma_{njk_\parallel}^{c-c}\\&=\pi\sum_{n'=c,v}\sum_{k',p}\sum_{i,j}\left|V_{nm}(k_\parallel k'_\parallel,ii',jj')\right|\times\delta\big(E\\&+E_{n'ip_\parallel}-E_{nj'k_\parallel}-E_{n'i'p'_\parallel}\big)\\&\times\left[f_n\big(E_{nj'k_\parallel}\big)f_{n'}\big(E_{n'i'p'_\parallel}\big)\big\{1-f_{n'}\big(E_{n'ip_\parallel}\big)\big\}\right.\\&+\big\{1-f_n\big(E_{nj'k'_\parallel}\big)\big\}\{1\\&\left.-f_{n'}\big(E_{n'ip'_\parallel}\big)\big\}f_{n'}\big(E_{n'ip_\parallel}\big)\right],\end{aligned}\qquad(A1)$$

where n refers to conduction (n = c) or valence (n = v) bands, i, i', j, and j' are the subband numbers of the QW structure, and $f_n(E)$ is the Fermi distribution function. The interaction matrix element V_{nm} in a two-dimensional QW is given by

$$\begin{aligned}&V_{nm}(k_\parallel k'_\parallel,ii',jj')\\&=\frac{e^2}{2\varepsilon_{GaN}A}\frac{\delta(k_\parallel-k'_\parallel,p'_\parallel-p_\parallel)}{\sqrt{\left|k_\parallel-k'\right|+\lambda_s^2}}\\&\times\int\int\phi^*_{nj'}(z_1)\phi_{nj}(z_1)\phi^*_{ni'}(z_2)\phi_{n'i'}(z_1)\\&\times\exp\left(-|z_1-z_2|\sqrt{\left|k_\parallel-k'\right|^2+\lambda_s^2}\right)dz_1dz_2,\end{aligned}\qquad(A2)$$

where the z-axis is perpendicular to the well interface. A is the interface area of the sample while the δ notation represents momentum conservation within a plane parallel to the well interface. $\phi_{nj}(z_1)$ is the wave function of a carrier which is obtained by the self-consistent solution of the Schrodinger-Poisson equation

for electrons and k.p method for holes. λ_s is the inverse screening length and its relation is as follows [29]

$$\lambda_s^2 = \frac{e^2}{\pi^2\hbar^3\varepsilon_{GaN}}\sum_j\left[m_{cj}f_c(E_{cj})\sqrt{m_{cj}E_{cj}} + m_{vj}f_v(E_{vj})\sqrt{m_{vj}E_{vj}}\right]. \quad (A3)$$

Here m_{cj} and m_{vj} are the effective masses of electrons and holes in the conduction and valance bands, which will be explained in the following. For carrier-longitudinal optical (LO) phonon scattering, the linewidth broadening is obtained by taking the imaginary part of the one-phonon self-energy [30]

$$\Gamma_{njk_\parallel}^{c-ph} = \pi\sum_{k'_\parallel}\sum_{j'}\left|P_n(k_\parallel k'_\parallel, jj')\right|^2 \times\{n_q+1 - f_n(E_{nj'k_\parallel})\}\delta(E_{nj'k'_\parallel}-E+\hbar\omega_{LO}) + \{n_q - f_n(E_{nj'k'_\parallel})\}\delta(E_{nj'k'_\parallel}-E + \hbar\omega_{LO}), \quad (A4)$$

where $\hbar\omega_{LO} = 91.13meV^{-1}$ is the energy of the LO phonon and n_q is the phonon number per mode, given by $n_q = 1/[\exp(\beta\hbar\omega_{LO})-1]$. The matrix element P_n for carrier-LO phonon scattering in a two-dimensional QW is given by

$$\left|P_n(k_\parallel k'_\parallel, jj')\right|^2 = \sum_q \frac{e^2\hbar\omega_{LO}}{2V}\left(\frac{1}{\varepsilon_\infty}-\frac{1}{\varepsilon}\right)\frac{q^2}{(q^2+\lambda_s^2)} \times\left|\int \phi_{nj}^*(z)\phi_{nj}(z)\exp(-iq_z)dz\right|^2, \quad (A5)$$

where $\boldsymbol{\varepsilon}_\infty$ is the optical dielectric constants, q_z is the phonon wave vector perpendicular to the well interface and V is the volume of the system. The intraband relaxation time τ_{in} is obtained from Eqs. (A1) and (A4) as $\hbar/\tau_{in} = \Gamma_{cjk_\square}(E) + \Gamma_{vjk_\square}(E)$.

References

[1] C. Boudaoud, A. Hamdoune, Z. Allam, "Simulation and optimization of a tandem solar cell based on InGaN." Mathematics and Computers in Simulation, **167** (2020) 194.

[2] M. Kuc, L. Piskorski, M. Dems, M. Wasiak, A. K. Sokoł, Robert P. Sarzała, T. Czyszanowski, "Numerical Investigation of the Impact of ITO, AlInN, Plasmonic GaN and Top Gold Metalization on Semipolar Green EELs." Materials, **13** (2020) 1444.

[3] A. Tian, L. Hu, L. Zhang, J. Liu, H. Yang, "Design and growth of GaN-based blue and green laser diodes." Science China Materials, **63** (2020) 1348.

[4] A. Pandey, W. J. Shin, J. Gim, R. Hovden, Z. Mi, "High-efficiency AlGaN/GaN/AlGaN tunnel junction ultraviolet light-emitting diodes." Photonics Research, **8** (2020) 331.

[5] X. Huang, H. Chen et al, "Energy band engineering of InGaN/GaN multi-quantum-well solar cells via AlGaN electron- and hole-blocking layers." Applied Physics Letters, **113** (2018) 043501.

[6] A.G. Bhuiyan, K. Sugita, A. Hashimoto, A. Yamamoto, "InGaN solar cells: present state of the art and important challenges," IEEE J Photovoltaics, **2** (2012) 276.

[7] J. Wu, W. Walukiewicz et al., "Small band gap bowing in $In_{1-x}Ga_xN$ alloys." Applied Physics Letters, **80** (2002) 4741.

[8] R. Yahyazadeh, "Effect of hydrostatic Pressure on Optical Absorption Spectrum AlGaN/GaN Multi-quantum wells." Journal of Interfaces, Thin films, and Low dimensional systems, **3** (2021) 279.

[9] R. Yahyazadeh, Z. hashempour, "Effects of Hydrostatic Pressure and Temperature on the AlGaN/GaN High Electron Mobility Transistors." Journal of Interfaces, Thin films, and Low dimensional systems, **2** (2019) 183.

[10] Q. Deng et al., "An investigation on InxGa1−xN/GaN multiple quantum well solar cells," Journal of Physics D: Applied Physice, **44** (2011) 265103.

[11] R. Belghouthi, M. Aillerie, "Temperatur dependece of InGaN/GaN Multiple quantum well solar cell." Energy Procedia, **157** (2019) 793.

[12] B. Chouchen, M. H. Gazzah, A. Bajahzar, Hafedh Belmabrouk, "Numerical Modeling of the Electronic and Electrical Characteristics of InGaN/GaN-MQW Solar Cells." Materials, **12**, (2019) 1241.

[13] R. Yahyazadeh, "Numerical Modeling of the Electronic and Electrical Characteristics of InGaN/GaN Multiple Quantum Well Solar Cells." Journal of Photonics for Energy, **10** (2020) 045504.

[14] X. Huang, "Piezo-Phototronic Effect in a Quantum Well Structure." ACS Nano, **10** (2016) 5145.

[15] O. Ambacher, A. B. Foutz, J. Smart, J. R. Shealy, N. G. Weimann, K. Chu et al., "Two dimensional electron gases induced by spontaneous and piezoelectric polarization in undoped and doped AlGaN/GaN heterostructures." Journal of Applied Physics, **87** (2000) 334.

[16] O. Ambacher, J. Majewski, C. Miskys, et al, "Pyroelectric properties of Al (In) GaN/GaN hetero- and quantum well structures." Journal of Physics Condensed Matter, **14** (2002) 3399.

[17] Z. J. Feng, Z. J. Cheng, and H. Yue, 'Temperature dependence of Hall electron density of GaN-based heterostructures." Chinese Physics **13** (2004) 1334.

[18] V. Fiorentini, F. Bernardini, and O. Ambacher, "Evidence for nonlinear macroscopic polarization in III–V nitride alloy Heterostructures." Applied Physics Letters, **80** (2002) 1204.

[19] P. Perlin, L. Mattos, N. A. Shapiro, J. Kruger, W. S. Wong, T. Sands, N. W. Cheung, E. R. Weber, "Reduction of the energy gap pressure coefficient of GaN due to the constraining presence of the sapphire substrate." Journal of Applied Physics, **85** (1999) 2385.

[20] K. J. Bala, A. J. Peter, C. W. Lee, "Simultaneous effects of pressure and temperature on the optical transition energies in a Ga0.7In0.3N/GaN quantum ring." Chemical Physics, **495** (2017) 42.

[21] I. Vurgaftman, J. R Meyer, L. R. R Mohan, "Band parameters for III–V compound semiconductors and their alloys." Journal of Applied Physics, **8** (2001) 5815.

[22] B. Jogai, "Influence of surface states on the two-dimensional electron gas in AlGaN/GaN heterojunction field-effect transistors." Journal of Applied Physics, **93** (2003) 1631.

[23] B. Jogai, "Parasitic Hole Channels in AlGaN/GaN Heterojunction Structures." Physica status solidi b, **233** (2002) 506.

[24] V. B. Yekta, H. Kaatuzian, "Design considerations to improve high temperature characteristics of 1.3μm AlGaInAs-InP uncooled multiple quantum well lasers: Strain in barriers." Optik. **122** (2011) 514.

[25] J. Piprek. Semiconductor Optoelectronic Devices: Introduction to Physics and Simulation. Elsevier Science, San Diego.California, (2013) 121.

[26] P. S. Zory, Quantum well lasers. Academic San Diego, CA (1993) 58.

[27] C.D. Mahan, Many-body particle physics. Plenum press, New York and London, Chapter 3 (1990).

[28] W. Wei-Ying et al, "Effects of interface roughness on photoluminescence full width at half maximum in GaN/AlGaN quantum wells." Chinese Physics B, **23** (2014) 117803.

[29] R. yahyazadeh, Z. Hashempour. "Numerical Modeling of Electronic and Electrical Characteristics of Multiple Quantum Well Solar Cells $Al_{0.3}Ga_{0.7}N$/GaN." Journal of Optoelectronical Nanostructures, **5** (2020) 81.

[30] S. H. Ha, S. L. Ban, "Binding energies of excitons in a strained wurtzite GaN/AlGaN quantum well influenced by screening and hydrostatic pressure." Journal of Physics Condensed Matter. **20** (2008) 085218.

[31] J.G. Rojas-Briseno, I. Rodriguez-Vargas, M. E. Mora-Ramos, J.C. Martínez-Orozco, "Heavy and light exciton states in c-AlGaN/GaN asymmetric double quantum wells." Physica E, **124** (2020) 114248.

[32] P. Harrison, A. Valavanis, Quantum Wells, Wires and Dots: Theoretical and Computational Physics of Semiconductor Nanostructures, 4th edition, Wiley (2016).

[33] E. Kasapoglu, H. Sari, N. Balkan, I. Sokmen, Y. Ergun, "Binding energy of excitons in symmetric and asymmetric coupled double quantum wells in a uniform magnetic field." Semiconductor Science and Technology, **15** (2000) 219.

[34] J.G. Rojas-Briseño, J.C. Martínez-Orozco, M.E. Mora-Ramos, "States of direct and indirect excitons in strained zinc-blende GaN/InGaN asymmetric quantum wells." Superlattices and Microstructures, **112** (2017) 574.

[35] R Yahyazadeh, Z.Hashempour, "Effect of Hydrostatic Pressure and Temperature on Quantum Confinement of AlGaN/GaN HEMTs." Journal of Science and Technology, **13** (2021) 1.

[36] S.L. Chung, C.S. Chang, "k.p method for strained wurtzite semiconductor." Physical Review B, **54** (1996) 2502.

[37] S. Adachi, Physical Properties of III-V compounds, John Wiley & Sons (1992) 290.

[38] S. R. Chinn, P. S. Zory, A. R. Reisinger, "A Modal for Grin-SCH-SQW Diode Lasers." IEEE Journal of quantum Electronics, **24** (1988) 2191.

[39] I. Tan, G. L. Snider, L. D. Chang, E. L. Hu. "A self-consistent solution of Schrödinger–Poisson equations using a nonuniform mesh." Journal of Applied Physics, **68** (1990) 4071.

[40] X. Huang et al., "Piezo-Phototronic Effect in a Quantum Well Structure." ACS Nano, **10** (2016) 5145.

[41] S. L. Ruminates, M. S. Shur, "Material properties of nitrides summary." International Journal of High Speed Electronics and Systems, **14** (2004) 1.

[42] Chuang, Physics of Photonic Devices, 2nd ed., Wily & Sons (1995).

[43] J. Nelson, "The physics of solar cells." Imperial college press, London (2003)

[44] Z. Dongmei, W. Zongchi, X. Boqi, "Correlated electron–hole transitions in wurtzite GaN quantum dots: the effects of strain and hydrostatic pressure." Journal of Semiconductors, **33** (2012) 052002.

Journal of Interfaces, Thin films, and Low dimensional systems 4 (1) Summer and Autumn (2020) 323-329

Dynamics of the entanglement in a two-spin system with long-range interaction

Scientific research paper

Mohammad Reza Soltani[1*], Maryam Mahmoudi[1], Saeed Mahdavifar[2], and Arezu Jahanshir[3]

[1]*Department of Physics,Yadegar-e-Imam Khomeini (RAH) Shahre Rey Branch, Islamic Azad University, Tehran, Iran*

[2]*Department of Physics, University of Guilan, 41335-1914, Rasht, Iran*

[3]*Department of Physics and Engineering Sciences, Imam Khomeini International University, Buein Zahra Higher Education Centre of Engineering and Technology, Iran*

ARTICLE INFO

Article history:
Received 25 May 2021
Revised 24 July 2021
Accepted 9 August 2021
Available online 28 October 2021

Keywords:
Entanglement dynamics
Long range
Negativity
Dzyaloshinskii-Moriya interaction
Magnetic field

ABSTRACT

Introduction: In this study, we investigate the dynamics of the Entanglement in a two- spin system with long- range interaction.

Method: For this purpose, we use the negativity as the entanglement measurement. Using the time evolution operator, we obtain entanglement dynamics of the system at time t. We consider two different initial states and investigate the dynamical behavior of the system for all of them separately. Finally, we consider both J and D as a function of R and then study the time evolution of the entanglement in different R.

Results: We find that in the long range interaction, the R dependence of the dynamical behavior in the two systems is different. Depending on the initial states, the DM interaction and the magnetic field have no effect on the entanglement dynamics.

1 Introduction

One of the most important predictions of modern quantum physics is the quantum entanglement [1]. Quantum entanglement is a quantum phenomenon in which the quantum states of two or more objects have to be described with reference to each other, even though the individual objects may be spatially separated. This results in quantum correlations between the observed physical properties of objects. Much effort is devoted describing the nature of the entanglement [2]. Quantum entanglement plays an important role in quantum information processing [3], teleportation [4], communication systems [5], quantum computer [6,7], quantum spin networks [8], security cryptography [9]. Therefore, significant research has been performed to understand quantum entanglement behavior in spin systems, such as all various kinds of Heisenberg (XX, XY, XXZ and XYZ) models, similar Ising models [10-12], and systems with Dzisloshinski-Moriya interaction [13,14].

Real physical systems are never isolated, as the connection between the system and the environment is inevitable. The quantum dynamics of physical systems is always complicated by their coupling with a number of «environmental» modes. Then, for realistic quantum systems, the loss of coherence is inevitable due to the interaction with the environment [15]. Recently, there has been more and more research on the dynamics of quantum entanglement under environmental influence [16-20].

*Corresponding author.
Email address: m.r.soltani.em@gmail.com
DOI: 10.22051/jitl.2021.36221.1055

In this paper, Entanglement is thus taken as a dynamic quantity on its own, as we survey how it evolves due to the unavoidable interaction of the entangled system with its surroundings. We analyze several scenarios for various initial states. In addition, we study the impact of spin distance on the dynamics of entanglement. Actually, we look at the exchange interaction as a function of the distance between two spins. This kind of interaction is known as long-term interaction. In recent years, long-term interactions have attracted a great deal of attention because they may produce new interesting phenomena [21-23]. In addition, some research has focused on the experimental application of spin systems that interact over long distances. Indeed, the inverse-square, trigonometric and hyperbolic interacting particle systems [25,26] and their spin generalizations [27-30] are important models of many-body systems due to their exact solvability and intimate connection to spin systems in condensed matter [31,32] and in other areas in physics. Therefore, studying the dynamical behaviour of systems with such interaction could be important. A major aspect of our analysis is that the entanglement does not disappear over time.

The paper is organized as follows: in the next section, we introduce the model Hamiltonian and describe briefly the techniques used to obtain the results discussed in the subsequent sections. In section III, we present and discuss the numerical results of modeling. Finally, Section 4 contains the concluding remarks.

2 Model

Here, we consider a set of two localized spin- 1/2 particles coupled through exchange interactions J, subjected to an external magnetic field of strength h with Dzyaloshinskii-Moriya interaction:

$$H = J(R)S_1^xS_2^x + D\left(S_1^xS_2^y - S_1^yS_2^x\right) + h(S_1^z + S_2^z), \quad (1)$$

Where J(R) is the exchange interaction parameter that varies with the distance between spins, R, as $J(R) = 1/R^2$. D is the Dzisloshinski-Moriya interaction parameter, and S is the spin-1/2 operator. In the base ket of S_{tot}^z , the Hamiltonian matrix is formed as

$$H = \begin{bmatrix} h & 0 & 0 & \frac{J}{4} \\ 0 & 0 & \frac{J}{4}+\frac{iD}{2} & 0 \\ 0 & \frac{J}{4}-\frac{iD}{2} & 0 & 0 \\ \frac{J}{4} & 0 & 0 & -h \end{bmatrix}. \quad (2)$$

The eigenvalues and eigenstates are:

$$\begin{aligned} \varepsilon_1 &= \frac{x}{4}\ ,\ |1\rangle = \frac{1}{\sqrt{2}}(|\uparrow\downarrow\rangle + \alpha|\downarrow\uparrow\rangle) \\ \varepsilon_2 &= -\frac{x}{4}\ ,\ |2\rangle = \frac{1}{\sqrt{2}}(|\uparrow\downarrow\rangle - \alpha|\downarrow\uparrow\rangle) \\ \varepsilon_3 &= \frac{y}{4}\ ,\ |3\rangle = \frac{1}{\sqrt{1+\beta^2}}(\beta|\uparrow\uparrow\rangle + |\downarrow\downarrow\rangle) \\ \varepsilon_4 &= -\frac{y}{4}\ ,\ |4\rangle = \frac{1}{\sqrt{1+\beta'^2}}(\beta'|\uparrow\uparrow\rangle + |\downarrow\downarrow\rangle) \end{aligned}, \quad (3)$$

$$x = \sqrt{J^2 + 4D^2}, y = \sqrt{J^2 + 16h^2}, \alpha = \frac{J - 2iD}{x},$$

$$\beta = \frac{4h - y}{J}, \beta' = \frac{4h + y}{j}, \quad (4)$$

On the other hand, to study the entanglement, one should obtain the density matrix of the system:

$$\rho = |\Psi_0><\Psi_0|, \quad (5)$$

where $|\Psi_0>$is the initial state of the system Hamiltonian. In our system the density matrix is reduced to:

$$\rho = \begin{bmatrix} \rho_{11} & 0 & 0 & \rho_{14} \\ 0 & \rho_{22} & \rho_{23} & 0 \\ 0 & \rho_{32} & \rho_{33} & 0 \\ \rho_{41} & 0 & 0 & \rho_{44} \end{bmatrix}. \quad (6)$$

Using the eigenvalues of the partial transpose of the density matrix, one can obtain the negativity of this model. Negativity is given by:

$$N = \frac{\|\rho^T\| - 1}{2}, \tag{7}$$

where $\|\rho^T\|$ is the trace norm or the sum of the absolute values of the operator ρ^T. In following, we try to describe dynamics of the entanglement of this system. The dynamic evolution operator $U(t) = \exp(-iHt)$ can be obtained as [33]

$$\mathrm{U}=\begin{bmatrix} U_{11} & 0 & 0 & U_{14} \\ 0 & U_{22} & U_{23} & 0 \\ 0 & U_{32} & U_{33} & 0 \\ U_{41} & 0 & 0 & U_{44} \end{bmatrix}, \tag{8}$$

where

$$U_{11} = U_{44} = cos\frac{yt}{4} + \frac{4ih}{y} sin\frac{yt}{4},$$

$$U_{14} = U_{41} = \frac{ij}{y} sin\frac{yt}{4},$$

$$U_{22} = U_{33} = cos\frac{xt}{4}, \qquad U_{23} = -i\alpha sin\frac{xt}{4},$$

$$U_{32} = -i\alpha^* sin\frac{xt}{4}.$$

In the next section, we consider two different initial configurations and study the dynamics of the system for both configurations. We compare the results of each configuration.

3 Discussion

Now, we consider two different initial states of the system and survey the time evolution of entanglement of the system for different parameters such as J, D, and h. Also, we consider J and D as a function of distance between two spins, R.

Case 1:

Suppose that at time t = 0 the qubits are entangled together and initial state given by:

$$|\psi(0)\rangle = \frac{1}{\sqrt{2}}(|\uparrow\downarrow\rangle + |\downarrow\uparrow\rangle). \tag{9}$$

Now, by applying the evolution operator on the $|\Psi_0>$, we can obtainthe physical state of the system at time t as:

$$|\psi(t)\rangle = \frac{1}{\sqrt{2}}\left[\left(\cos\left(\frac{\mathrm{xt}}{4}\right) - \mathrm{i}\alpha\sin\left(\frac{\mathrm{xt}}{4}\right)\right)|\uparrow\downarrow\rangle + \left(\cos\left(\frac{\mathrm{xt}}{4}\right) - \mathrm{i}\alpha^*\sin\left(\frac{\mathrm{xt}}{4}\right)|\downarrow\uparrow\rangle\right)\right]. \tag{10}$$

It is noticeable that by selecting the above initial state, the role of the magnetic field disappears in the time evolution of the entanglement. In fact, the change of *h* does not affect the entanglement dynamics of the system. By having $|\psi(\mathrm{t})\rangle$, we can calculate the density matrix of the system at time t, and then get a formula for the negativity as a function of t:

$$N = \frac{\sqrt{1 - \frac{4D^2}{x^2}\sin^2\frac{xt}{2}}}{2}. \tag{11}$$

Figure 1 shows the evolution of the Negativity when J and D are constant. As seen in the figure, the system has a regular behavior over time. Although the amount of the negativity drops highly at some times, but it will never be zero.

Then, we investigate the effect of the DM interactions on the dynamics of the negativity. Figure 2 shows the D dependence of the negativity evolution. Increasing the DM interaction, increases the amplitude of the entanglement oscillations. Indeed, the weaker DM interaction leads to more stable oscillations of the entanglement over time. In addition, the rise of D, reduces the time period of negativity.

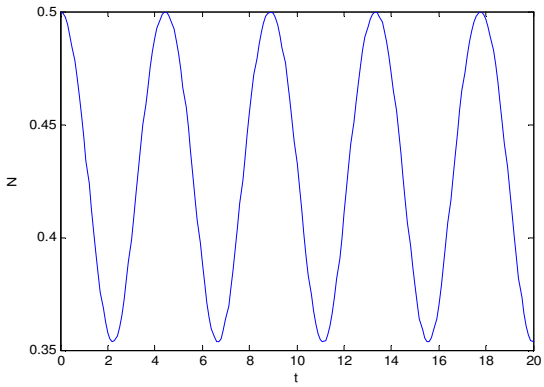

Figure 1. The time evolution of the negativity's in the system with initial state as $|\psi(0)\rangle = \frac{1}{\sqrt{2}}(|\uparrow\downarrow\rangle + |\downarrow\uparrow\rangle)$. We set J=1, D=0.5.

When we study the time period of these oscillations, we observe that for J>D the time period diminishes by increasing D. But, for J≤ D, the time period remains constant. In fact, it may be said that J=D is a point where the behavior of the entanglement dynamics has changed.

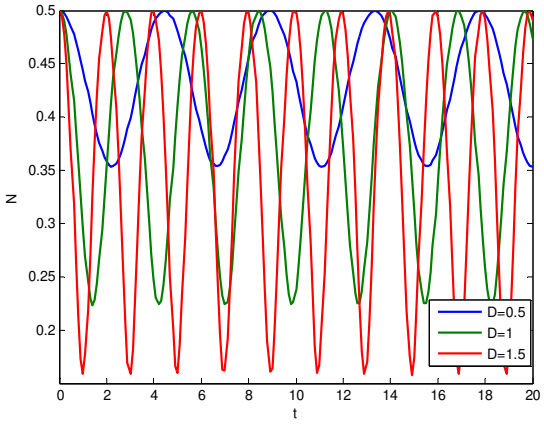

Figure 2. The D dependence of the negativity's time evolution with initial state as $|\psi(0)\rangle = \frac{1}{\sqrt{2}}(|\uparrow\downarrow\rangle + |\downarrow\uparrow\rangle)$. Set J=1.

Now, we investigate the dynamics of the negativity when the exchange interaction is a function of the spin distance, R as $J = \frac{1}{R^2}$. The effect of the long range exchange interaction on the negativity dynamics is noticeable. As seen in Fig. 3, when the distance between two interacting spins increases, the time evolution of the entanglement becomes more unstable and the amplitude and time period of the oscillations increase. It shows the entanglement dynamics depends upon the distance between qubits. The rapid oscillations show rapid energy exchange between spins at very small distances. Indeed, reducing R is a positive factor to avoid the sharp and unstable oscillations of the entanglement dynamics. If we study the time period of these oscillations, we observe that for J>D and then R< 1/D, the time period decreases by increasing D. But, for J≤ D and then R≥1/D, the time period remains constant.

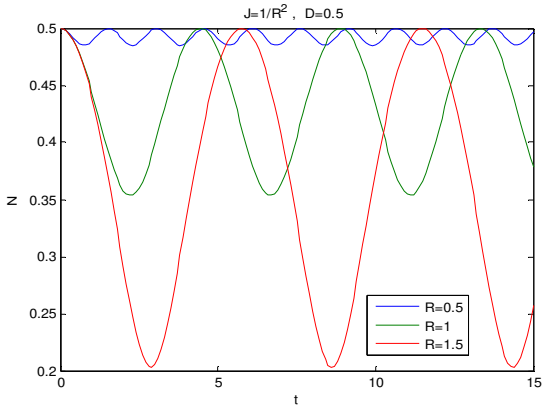

Figure 3. The R dependence of the entanglement's time evolution with initial state as $|\psi(0)\rangle = \frac{1}{\sqrt{2}}(|\uparrow\downarrow\rangle + |\downarrow\uparrow\rangle)$. Set $J = \frac{1}{R^2}$.

In the next step, we consider both J and D as functions of R. It is noticeable that in different values of R, the amplitude of the fluctuations of the entanglement is mostly the same. But, by increasing R, the time period increases, see Fig. 4.

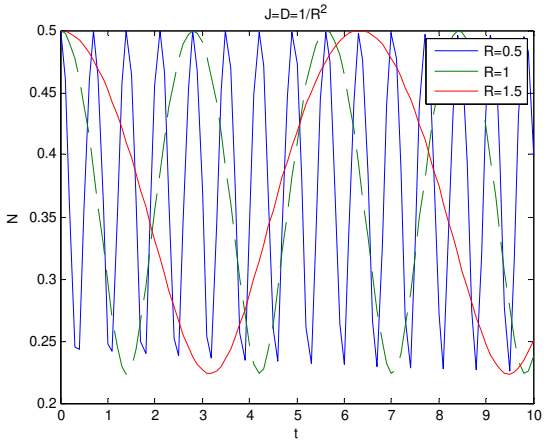

Figure 4. The R dependence of the entanglement's time evolution with initial state as $|\psi(0)\rangle = \frac{1}{\sqrt{2}}(|\uparrow\downarrow\rangle + |\downarrow\uparrow\rangle)$. Set $J = \frac{1}{R^2}$ and $D = \frac{1}{R^2}$.

Case 2:

Suppose that at time t = 0 the qubits are entangled together and initial state given by:

$$|\psi(0)\rangle = \frac{1}{\sqrt{2}}(|\uparrow\uparrow\rangle + |\downarrow\downarrow\rangle). \qquad (12)$$

Now, by applying the evolution operator on $|\Psi_0>$, we can obtain the physical state of the system at time t. This initial state makes the effect of the DM interaction remove from the dynamic behavior of the entanglement. The negativity of the system with this initial state is:

$$N = \frac{1}{2}\sqrt{(1-\frac{32h^2}{y^2}\sin^2\frac{yt}{4})^2+\frac{16h^2}{y^2}\sin^2\frac{yt}{2}} \quad . \quad (13)$$

Like the previous section, we study the entanglement dynamics of this initial state in three modes: a) J and D are constant, b) $=\frac{1}{R^2}$, and c) $J = D = \frac{1}{R^2}$. First, we consider $J = 1$ and $D = 1$. As seen in Fig. 5, the dynamic behavior of this kind of initial state is oscillatory. Compared to the previous initial state, the time period and amplitude drop of the negativity are lower.

When the exchange interaction is dependent on R, the dynamic behavior of the negativity is as illustrated in Fig. 6. By increasing R, and therefore reducing J, the oscillations amplitude increases. Indeed, the less distance between spins leads to a stronger exchange interaction that leads to a more stable behavior of the entanglement dynamics along the time. Compared to the previous initial state, the amplitude drop of the dynamic fluctuations, especially in large R, is more. Similar to the previous initial state, when we study the time period of these oscillations, we observe that for J>h the time period decreases by increasing D. But, for J≤ h, the time period remains constant. In fact, it can be said that J=h is a point at which the behavior of entanglement dynamics has changed.

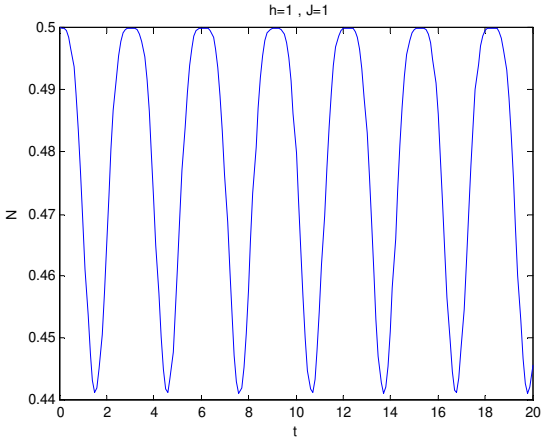

Figure 5. The time evolution of the entanglement in the system with initial state as $|\psi(0)\rangle = \frac{1}{\sqrt{2}}(|\uparrow\uparrow\rangle + |\downarrow\downarrow\rangle)$. We set J=1, h=1.

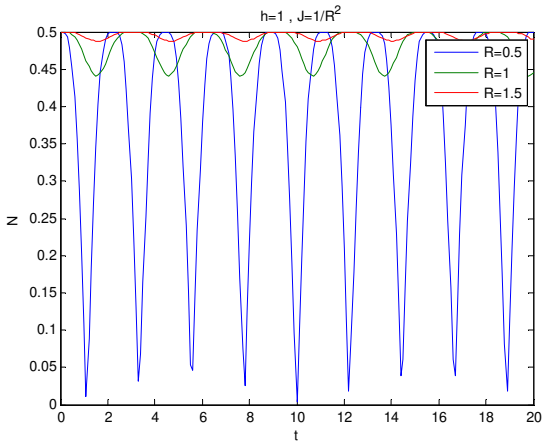

Figure 6. The R dependence of the entanglement's time evolution with initial state as $|\psi(0)\rangle = \frac{1}{\sqrt{2}}(|\uparrow\uparrow\rangle + |\downarrow\downarrow\rangle)$. Set $J = \frac{1}{R^2}$.

As mentioned previously, in the system with such an initial state, the DM interaction does not influence the dynamic behavior of the negativity. In contrary, the magnetic field influences the dynamics of the negativity in the system with this new initial state. Figure 7 shows that in a weak magnetic field, the oscillations of negativity are greater than when exposed to a strong magnetic field. It can be said that the magnetic field has a positive effect on the dynamics of the entanglement in this system. Similar to the previous section, until R has satisfied the condition of J≤h ($J=1/R^2$), the time period of the negativity oscillations is constant. As soon as J>R, the time period reduces by decreasing R (increasing J).

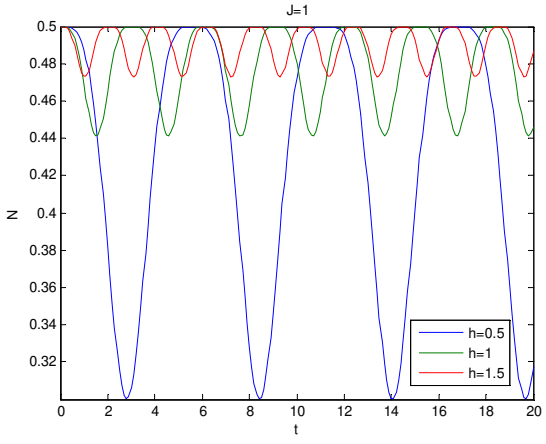

Figure 7. The time evolution of the entanglement in different magnetic fields in the system with initial state as $|\psi(0)\rangle = \frac{1}{\sqrt{2}}(|\uparrow\uparrow\rangle + |\downarrow\downarrow\rangle)$.

4 Conclusions

We considered two different initial states of the system and studied the dynamic behavior of the system for each of both situations, separately. It was interesting that in the system with initial state of $|\psi(0)\rangle = \frac{1}{\sqrt{2}}(|\uparrow\downarrow\rangle + |\downarrow\uparrow\rangle)$, the magnetc field didn't have any effect on the entanglement dynamics while the DM interaction had the negative effect on the time evolution of the entanglement. In contrast, in the dynamic behavior of the system with initial state of $|\psi(0)\rangle = \frac{1}{\sqrt{2}}(|\uparrow\uparrow\rangle + |\downarrow\downarrow\rangle)$, the DM interaction has no effect on the entanglement dynamics, while the magnetic field was a positive factor to decrease the amplitude of the oscillations of the entanglement with time. In addition, we found that in the long range interaction, namely the exchange interaction was a function of the distance between two spins, the R dependence of the dynamic behavior in the two systems was different. In the system with $|\psi(0)\rangle = \frac{1}{\sqrt{2}}(|\uparrow\downarrow\rangle + |\downarrow\uparrow\rangle)$ as the initial state, increasing the spin distance caused the sharp drop of the oscillation amplitude of the negativity with time. Indeed, we can say that the high R, namely the weak exchange interaction, causes the unstable fluctuations in the entanglement dynamics of the system. Whereas, in the system with $|\psi(0)\rangle = \frac{1}{\sqrt{2}}(|\uparrow\downarrow\rangle + |\downarrow\uparrow\rangle)$ as the initial state, increasing the spin distance led to a more stable dynamic behavior in the system. Furthermore, when both J and D were functions of R, the change of R did not have any effect on the oscillation amplitude of the entanglement dynamics but increased the time period of the oscillations.

References

[1] W. Wotters, "Entanglement of Formation of an Arbitrary State of Two Qubits." Physical Review Letters, **80** (1998) 2245.

[2] R. Horodecki, P. Horodecki, M. Horodecki, K. Horodecki, "Quantum Entanglement." Review of Modern Physics, **81** (2009) 865.

[3] J. Gruska, "Quantum entanglement as a new information processing resource." New Generation Computing, **21** (2003) 279.

[4] S. Mirzaei, A. R. Akbarieh, "Quantum Teleportation via Entangled State of Light in Schwarzschild Black Hole." International J Theoretical Physics, **59** (2020) 3583.

[5] L. Gyongyosi, S. Imre and H. V. Nguyen, "A Survey on Quantum Channel Capacities." in IEEE Communications Surveys & Tutorials, **20** (2018) 1149.

[6] X.-D. Cai, D. et al. "Entanglement-Based Machine Learning on a Quantum Computer" Physical Review Letters, **114** (2015) 110504.

[7] L. F. Santos, "Quantum computation with quantum dots." Physical Review A, **67** (2003) 062306.

[8] Peter J. Pemberton-Ross and Alastair Kay, "Perfect Quantum Routing in Regular Spin Networks." Physical Review Letters, **106** (2011) 020503.

[9] Yin, J., Li, YH., Liao, SK. et al. "Entanglement-based secure quantum cryptography over 1,120 kilometres." Nature, **582** (2020) 501.

[10] X. Wang, "Entanglement in the quantum Heisenberg XY model", Physical Review A, **64** (2001) 012313.

[11] S. Deniz, E. Aydiner, " Thermal entanglement in the mixed three-spin XXZ Heisenberg model on a triangular cell." Chinese Physics B, **2** (2014) 5.

[12] L. F. Santos, "Entanglement in quantum computers described by the XXZ model with defects." Physical Review A, **67** (2003) 062306.

[13] S. D. Han, E.Aydiner, " Thermal entanglement in the mixed three-spin XXZ Heisenberg model on a triangular cell." Chinese Physics B, **23** (2014) 050305.

[14] Z. Ming , X. Hui, L. Xiao-Xian, T. Qing, "The effects of the Dzyaloshinskii—Moriya interaction on the ground-state properties of the XY chain in a transverse field." Chinese Physics B, **22** (2013) 9.

[15] H. Breuer, F. Petruccione, "The Theory of Open Quantum-Systems", Oxford University Press, Oxford, New York (2002).

[16] T. Werlang, S. Souza, F. F. Fanchini , C. J. Villas Boas, " Robustness of quantum discord to sudden death." Physical Review A, **80** (2009) 024103.

[17] L. Mazzola, J. Piilo , S. Maniscalco, " Sudden Transition between Classical and Quantum Decoherence." Physical Review Letters, **104** (2010) 200401

[18] R. Vasile, P. Giorda, S. Olivares, G. A. Paris , S. Maniscalco, " Open Quantum Systems and entanglement." Physical Review A, **82** (2010) 012313.

[19] B. Wang, Z. Xu, Z. Chen , M. Feng, " Bell violation versus geometric measure of quantum discord and their dynamical behavior." Physical Review A, **81** (2010) 014101.

[20] F. Fanchini, T. Werlang, C. A. Brasil, L. G. E. Arruda , A. O. Caldeira, " Non-Markovian dynamics of quantum discord." Physical Review A, **81** (2010) 052107.

[21] M. R. Soltani, S. Mahdavifar, M. Mahmoudi, " Entanglement in a two-spin system with long-range interactions." Chinese Physics B, **25** (2016) 087500.

[22] P. Jurcevic, " Quasiparticle engineering and entanglement propagation in a quantum many-body system." Nature, **511** (2014) 202.

[23] J. Schachenmayer, B. P. Lanyon, C. F. Roos, A. Daley, "Entanglement Growth in Quench Dynamics with Variable Range Interactions." Physical Review X, **3** (2013) 031015.

[24] Samihr Hermes, Tony J. G. Apollaro, Simone Paganelli, Tommaso Macri, “Dimensionality-enhanced quantum state transfer in long-range-interacting spin systems.” Physical Review A, **101** (2020) 053607.

[25] Soltani M R, Mahdavifar S, Mahmoudi M. “Entanglement in a two-spin system with long-range interactions.” Chinese Physics B, **25** (2016) 087501.

[26] N. Zidan,” Entropic Uncertainty in Spin XY Model with Long-Range Interactions.” Entropy, **22** (2020) 837.

[27] J. Gibbons, T. Hermsen, " A generalisation of the Calogero-Moser system." Physica D, **11** (1984) 337.

[28] S. Wojciechowski, " Integrable one-particle potentials related to the Neumann system and the Jacobi problem of geodesic motion on an ellipsoid." Physics Letters A, **111** (1985) 107.

[29] F. D. Haldane, "Exact Jastrow-Gutzwiller resonating-valence-bond ground state of the spin-(1/2 antiferromagnetic Heisenberg chain with 1/r 2 exchange." Physical Review Letters, **60** (1988) 635.

[30] B. S. Shastry, "Exact solution of an S= 1/2 Heisenberg antiferromagnetic chain with long-ranged interactions." Physical Review Letters, **60** (1988) 639.

[31] H. H. Tu and Y. Wu, “Exactly Solvable Quantum Impurity Model with Inverse-Square Interactions.” Physical Review Letters, **123** (2019) 066406.

[32] H. Fakhri, S.B. SeyedeinArdebili, “Exact solutions for the ferromagnetic and antiferromagnetic two-ring Ising chains of spin-1/2.” Physica A: Statistical Mechanics and its Applications, **523** (2019) 557.

[33] T. Quan, Z. D. Wang , C. P. Sun, " Quantum critical dynamics of a qubit coupled to an isotropic Lipkin-Meshkov-Glick bath." Physical Review A, **76** (2007) 012104.

Journal of Interfaces, Thin films, and Low dimensional systems 4 (1) Summer and Autumn (2020) 331-338

The effect of laser parameters (frequency and fluency) on the optical and structural characteristics of ZnO films deposited by the PLD method

Scientific research paper

Faezeh Hassani[1], Batool Sajad[1*], Seyedeh Soraya Mousavi[1], Mehrnaz Simdar[1], and Mohammad Amin Bassam[2]

[1]*Department of Physics, Faculty of Physics and Chemistry, Alzahra University, Tehran, Iran*

[2]*Electronics Department, Malek Ashtar University, Tehran, Iran*

ARTICLE INFO

Article history:
Received 25 July 2021
Revised 29 September 2021
Accepted 29 September 2021
Available online 28 October 2021

Keywords:
Pulsed Laser Deposition
Pulse Repetition Rate
Zinc Oxide
Optical properties
Morphological Structure
Laser Fluency

ABSTRACT

The pulsed laser deposition is a practical synthesis route because of its unique advantages in growing various materials. Furthermore, the quality of thin films depends on different parameters in the deposition process. Meanwhile, ZnO has many applications in manufacturing optics, electronics, and optoelectronics instruments because of its exclusive properties. We have set up a PLD array to deposit the ZnO thin films on glass substrates. This study investigates the structural and optical characteristics of the films deposited at two different pulse repetition rates. Based on the optical-microscopic images and the scanning electron microscope (SEM) micrographs of films, increasing pulse repetition rate increases the uniformity of the particle size distribution and enhances film thickness. Also, the optical characterization performed by UV-Visible spectroscopy shows that the absorption and transmission rate, bandgap energy, and crystalline quality of the films can adjust by tuning the pulse repetition rate.

1 Introduction

Pulsed Laser Deposition (PLD) has emerged as a most popular synthesis technique because of its attractive principal features like simplicity implementation, high deposition rate, stoichiometric transfer material from target to the substrate, the possibility of deposition in a wide range of temperatures, and the possibility of depositing at different background pressures. PLD is a physical vapor deposition technique that can form various materials in various structures like thin films, multi-layers, nanostructures, and epitaxial films [1–3]. During the PLD process, carried out in a vacuum system, a high-energy beam of the pulsed laser focuses on the located target, resulting in evaporation/ablation on the target surface and removing a part of the material. Rejected materials produce a highly forwarded direct plume to the substrate, condense on it, and form the thin film [4].

ZnO has unique properties that make it a helpful semiconductor with its wide range of applications in optics, electronics, optoelectronics, and energy-saving industries. The direct wide bandgap (3.37 eV at room temperature) with a large exciton binding energy of 60 meV and high electron mobility and irradiation resistance makes it an ideal candidate for UV detection. The most common ZnO applications are luminescent materials, transparent conductive contacts, surface electro-acoustic wave devices, thin-film gas sensors, ultraviolet (UV) lasers, varistors, and solar cells [5–10]. Moreover, many different synthesis techniques prepare

*Corresponding author.
Email address: Bsajad@Alzahra.ac.ir
DOI: 10.22051/jitl.2021.37048.1058

ZnO thin films like sputtering, reactive thermal evaporation, spray pyrolysis, sol-gel [14], and PLD [12].

The mentioned benefits above make PLD an exciting route for researchers. As many papers reported, the quality of the deposited ZnO films is directly impressed by deposition parameters like background pressure, substrate temperature [15], irradiation parameters, and post-annealing conditions[16–18]. Laser beam energy, pulse duration, pulse repetition rate are the effective irradiation parameters on the film's quality [19].

Energy density plays a key role in the ablation process, and subsequently by related properties of laser-induced plasma plume would influence the film properties [20]. The fluency should override the binding energy of target material constituents to remove an atom from the target surface by a laser pulse. Therefore, the ablation rate from the target is a function of laser fluency [21].

The pulse repetition rates (PRR) mainly impress the final film quality via two different effects. On one side, the pulse laser frequency has particularly affected the time interval for the ZnO plume towards the substrate. As a result, the adatoms do not have enough time intervals to locate the proper position in the lattice structure for the high pulse repetition rates [22]. On the other hand, at the high pulse repetition rate, the time between two laser pulses is not enough, so the temperature of the target surface cannot decrease to its initial amount. Thus, the next pulse operates at a higher temperature. This thermal effect causes an increased ablation efficiency due to a higher repetition rate [23]. According to the simulation results, more and smaller islands can be formed at higher pulse frequencies. The reduced island size can enhance the diffusion of adatoms from the top of the growing islands to lower levels on the substrate, resulting in a smoother film surface. On the contrary, lower pulse frequencies can diminish surface smoothness due to the reduced island density and the elevated average island size [24]. This contradiction leads to an optimum PRR value.

Most PLD processes use the Excimer lasers with higher energy and lower wavelength (KrF: 248 nm) and higher vacuum orders. The ZnO films grown by the shorter wavelength lasers show much higher quality because the higher wavelengths lead to subsurface heating of the target and producing undesirable defects [20]. Since excimer lasers often have higher energies with an almost flat top energy profile compared to the Gaussian energy profile of Nd: YAG lasers, the fluency varies intrinsically. This variation is therefore included in the deposition parameters [25].

We have previously designed and set up a PLD system to optimize it with a well-known Zinc Oxide material [26]. A Q-switch Nd YAG laser (1064 nm wavelength (1 Jcm-2) and 10-5 mbar) was employed as the irradiation source. These conditions thoroughly result in different film characteristics. The optical band gap and Urbach energy were calculated for the samples deposited by various fluencies as effective parameters. Moreover, we investigated the annealing effect [26], substrate heating mode [27, 28], and the growing seed layer effect on the film quality.

Although most of the laser parameters have been investigated in some publications [20, 22], the effects of PRR and fluency on the film's optical properties (band gap and Urbach energy) have been rarely investigated. Instead, the publications studied the effects of deposition parameters on the growth of different ZnO structures [29], doping ZnO films with other materials [30, 31], or the other optical characteristics of the films (photoluminescence) [22].

This paper also investigates ZnO film properties for two different PRRs to study the impact of laser repetition rate on the optical and structural characteristics of the films.

2 Method

2.1 Experimental setup

A PLD set-up consists of a vacuum system and a Q-switch Nd: YAG laser irradiation source (up to 216 mJ/pulse, 5 ns pulse duration, 1-10 Hz PRR at the 1064 nm wavelength). The vacuum system includes a deposition chamber, a high vacuum-mixing table, and pressure measurement tools. As shown in Fig. 1a, the irradiation chamber was fabricated of stainless steel, ~300 cm^3, with triplet windows and the target and substrate holder facing each other. The target holder is positioned at a 45° angle with the incident laser beam (Fig. 1b).

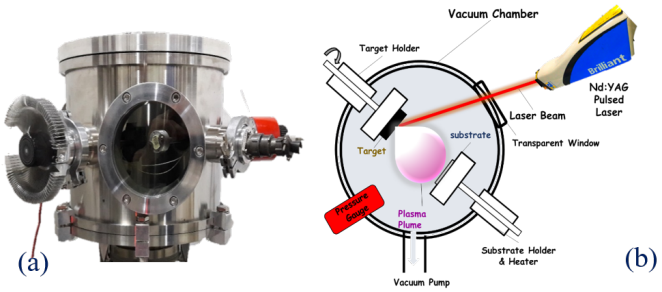

Figure 1. (a) The triplet- windows vacuum chamber. (b) The schematics of the PLD system mechanism

A ZnO tablet with 270 mm diameter and 3mm thickness is used as the target. It is prepared from the high purity ZnO powder (99.99%), pressed by 104 kPa hydrodynamic pressure at room temperature in a holder. The cubic glass slides (used as the substrates) were ultrasonically cleaned in soapsuds, acetone, and ethanol for 10 minutes per stage, dried in nitrogen flow, and then fixed on the substrate holder into the vacuum chamber distances 3.5 cm from the target.

2.2 Deposition Conditions

The chamber was evacuated up to the pressure of 5-10 mbar by a diffusion pump and a one-stage rotary backup pump. The background pressure was monitored by Pirani and penning gauges. The substrates were pre-heated to 350°C before starting the deposition process by an electric heater. Then the target was exposed by laser with 1 J/cm^2 fluency and the parameters summarized in Table 1. The final films post-annealed at 400° for 30 minutes after completing the deposition process.

Table 1- Laser irradiation parameters

Sample	P. R. R. (Hz)	Laser Fluence (J/cm^2)	Time exposure (min)
PRR 3.3	3.3	1	50:50
PRR 5	5.0	1	33:34

3 Results and discussion

Since the pulse frequency ranges between 1 to 10, we set 3.3 and 5 Hz as the studying cases located in the medium intervals. Therefore, PRR 3.3 and PRR 5 stand for the film deposited with 3.3 Hz and 5 Hz, respectively.

3.1 Structural and Morphological analysis

Figure 2 represents optical images of the film surfaces. It can be seen that the film deposited with the higher repetition rate (PRR 5) shows a highly condensed and uniform surface covering the whole substrate (Fig. 2b). In fact, by increasing the pulse repetition rate, the particles aggregate together and make films with higher density. The SEM images are another evidence for this claim.

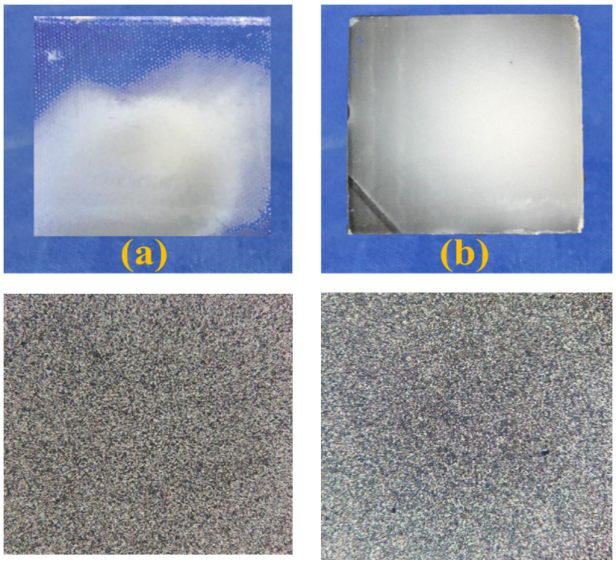

Figure 2. The photos and their optical microscopy images of: (a) PRR 3.3 and (b) PRR 5.

In Fig. 3, The SEM micrographs of the film surfaces represent the porous structure of the layers. It indicates that an increase in pulse repetition rate causes an increase in the average particle sizes. The grain size is estimated to be 20-40 nm and 60-80 nm for PRR 3.3 and PRR 5, respectively.

Therefore, accumulated nanoparticles during a higher deposition rate result in the creation of greater particles. In addition, the thermal effects, as mentioned before, increase the ablation efficiency for PRR 5. Therefore, the same laser fluency can ablate the greater particles. Furthermore, the cross-sectional SEM images in Fig. 3 show the estimated film's thickness to be 1 µm and 1.18 µm for PRR 3.3 and PRR 5, respectively. This thickness growth (18%) occurred during the high pulse repetition when the subsequent deposition process occurs before the activated states are energetically released [29].

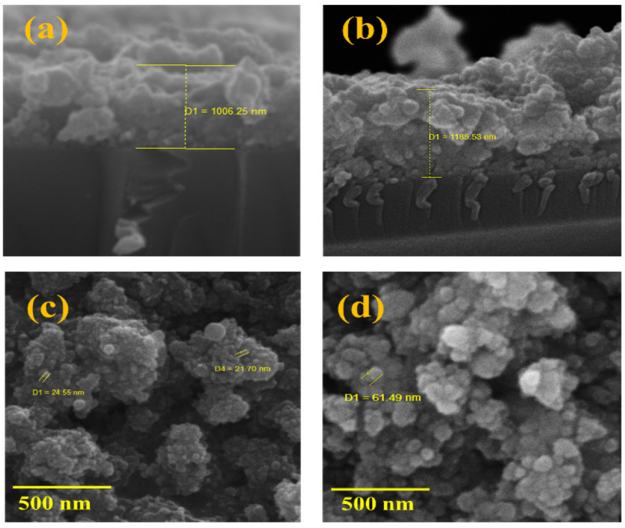

Figure 3. The morphological SEM micrographs of the film's surface (a) PRR 3.3 and (b) PRR 5. The cross-sectional SEM images of (c) PRR 3.3and (d) PRR 5.

3.2 Optical analysis

3.2.1 Effect of the Pulse Repetition Rate

Figure 4 shows the UV-Vis spectrum of the films. The inner picture relates to the films' absorbance. Both samples have an absorption peak near the UV region contributed to the ZnO bandgap. However, there is a blue shift in the absorption peak wavelength for PRR 3. It is at a value of 343 nm whereas 346 nm for the other one (about 0.03 eV). This partial shift results from the increasing size of the film's particle confirmed in SEM images (Fig. 3) [32].

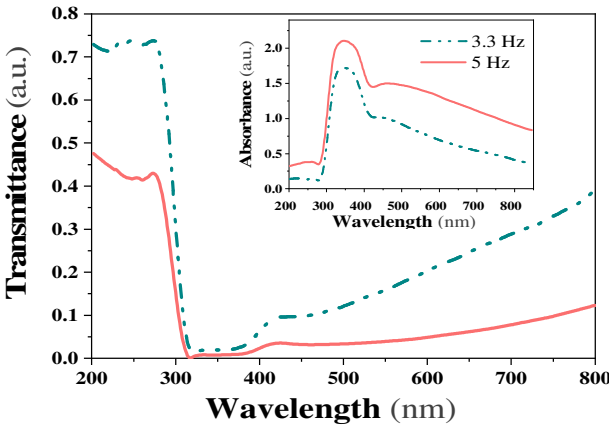

Figure 4. Absorbance and Transmittance spectra of films in ultraviolet and visible region

Compare the films' absorbance spectra at a glance, determine that the absorption of the films deposited with higher pulse laser frequency increased in the ultraviolet and visible region. This enhancement can be caused by increasing deposition rate, which leads to a rise in film's thickness, thereby enhancing the absorption of incident photons in the film and the scattering at the film surface that lower the optical transmittance [17].

Since the measured reflectance was negligible, the transmittance spectrum came from Eq (1), where A and T return to the absorbance and transmittance, respectively:

$$T = 10^{-A}. \quad (1)$$

As shown in Fig. 4, the optical transmittance of films sharply decreases in the near UV region due to bandgap absorption. According to the transmittance spectra, the film's absorbance reduces by 25% in the ultraviolet region and 10-30% in the visible region for PRR 3.3 compared to the other one. The lower transmittance value could be due to several factors such as film defects, particulates onto the surface, and light scattering at the rough surface, high thickness [33].

For the materials having direct transition like ZnO, the optical band gap energy is determined by the Tauc relation as follows (Eq. (2)):

$$\alpha h\nu = A(h\nu - E_g)^n, \quad (2)$$

$$T = e^{-\alpha t}, \quad (3)$$

Where α is the absorption coefficient, t attributes to film's thickness obtained from cross-sectional SEM images, hν equals to incident photon's energy, E_g is the energy gap, and n is a constant at a value of 0.5 for ZnO. The Tauc graph plotted in Fig. 5a, with $(\alpha h\nu)^2$ along the y-axis and hν along the x-axis, gives the optical bandgap with a sharp edge absorption using linear approximation. As shown in Fig. 5, the bandgap narrowed by 0.09 eV in the film with a higher pulse frequency. According to the references, a blue shift in the optical band gap occurs due to the relatively higher carrier concentration [34].

Presence of tail absorption profile in the visible region (Fig. 4, inner Pic), induced by optical absorption on intrinsic defects of the film's structure, so-called

"Urbach energy or Urbach tail width." The Urbach tail occurs due to a structural disorder. This energy characterizes as a consequence of all created defects in the film [33]. The Urbach energy can be estimated by the Urbach low as:

$$\ln \alpha = \ln \alpha_0 + \left(\frac{\nu}{E_u}\right), \quad (4)$$

where α_0 is a constant, and E_u Urbach energy is obtained from the slope of linear fit on the plot of lnα versus hν (Fig. 5b). The numerical value of the Urbach energy is 0.50 and 0.25 related to PRR 3.3 and PRR 5, respectively. As mentioned, this reduction in E_u value is due to a decrease in the number of defects in the film deposited with a higher pulse repetition rate. These results were well agreed with the similar works. They both indicated the formation of a higher quality film with the lower defect concentrations for the samples that depend on the pulse repetition rate. Thus, the results confirm each other; however, the approaches used for analyzing the samples are different [22].

3.2.2 Effect of the Laser Fluency

Laser fluency describes the optical energy delivered per unit of area (laser energy density). It comes from Eq. (5) for each laser pulse:

$$\text{Fluency} = \frac{\text{Laser Energy}\,(\text{J})}{\text{Beam Area}\,(\text{cm}^2)}. \quad (5)$$

According to the above equation, fluency can be controlled by energy per pulse and the effective laser spot area. Therefore, we study four different fluencies (F1, F2, F6, and F14) by changing these two parameters. The parameters are summarized in Table 2.

Although the deposition rate varies linearly with the fluency, it has not affected the film texture, in 1064 nm wavelength, as also concluded by other publications [35].

Figure 6 shows the optical images of the samples. All samples were deposited in the same condition; however, F6 and F14 (with the higher fluency) indicated poor coverages. Such that some separated particles were settled on the substrate without a film formation. This is due to the high kinetic energy of the materials, which does not allow particles to locate on the substrate surface.

Table 2- Laser parameters

Sample	*F1*	*F2*	*F6*	*F14*
Energy per Pulse (mJ)	216	216	47	112
Laser Spot (mm)	5.2	4	1	1
Fluency (J/cm²)	1	2	6	14

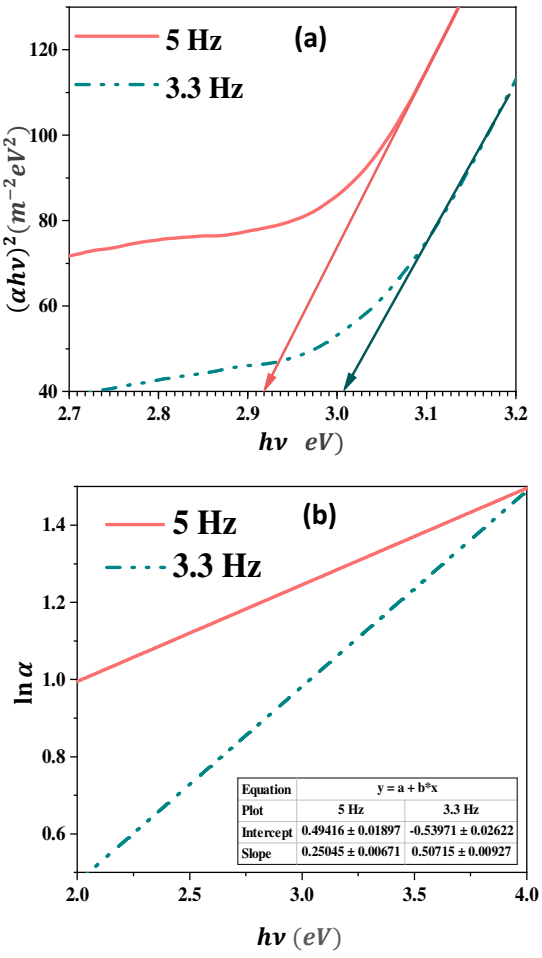

Figure 5. (a) Tauc graph ($(\alpha h\nu)^2$ versus hν) for ZnO samples; (b) Logarithmic plot of absorption coefficient versus photon energy.

The absorbance and transmittance spectra of the films in the ultraviolet and visible region are shown in Fig. 7. As we expected, F6 and F14, with their low surface coverage, have a little absorption and a small peak in the absorption edge at about 335 nm wavelength. According to information obtained from films' structure and UV-Vis spectra, the optical properties have been investigated for F1 and F2 (the films with the higher quality) using the Tauc plot and Urabch tail.

The Tauc plot in Fig. 8 obtains the films' optical bandgap. There is a slight blue shift in absorption edge

for F1 and shows an enhancement in its band gap by 0.05 eV. Consequently, the average size of the particles in this sample is smaller than that of F2.

According to the absorbance tail in the visible region for both samples, defects in the films' structures are expected. Thus, Urbach energy is estimated based on Eq. (4) and plotted in Fig. 8. The Urbach energies are obtained about 0.8 and 0.6 for F1 and F2, respectively. As a result, it can be concluded that the concentration of defects decreased in the film deposited with higher fluency. These results are in good agreement with the published results regarding the defects prior to the present study [21, 25].

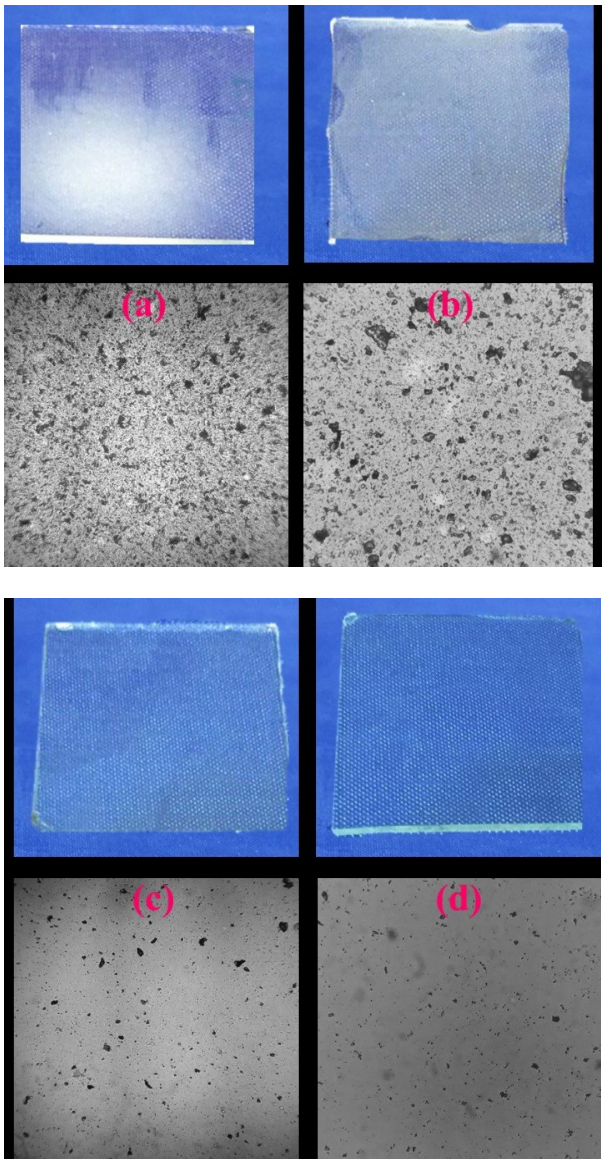

Figure 6. The photos and their optical microscopy images of: (a) F1, (b) F2, (c) F6, and (d) F14.

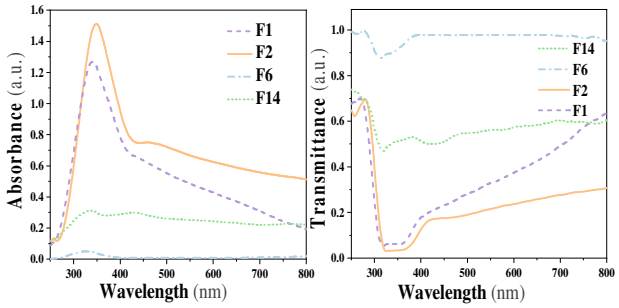

Figure 7. Absorbance and Transmittance spectra of films in ultraviolet and visible region

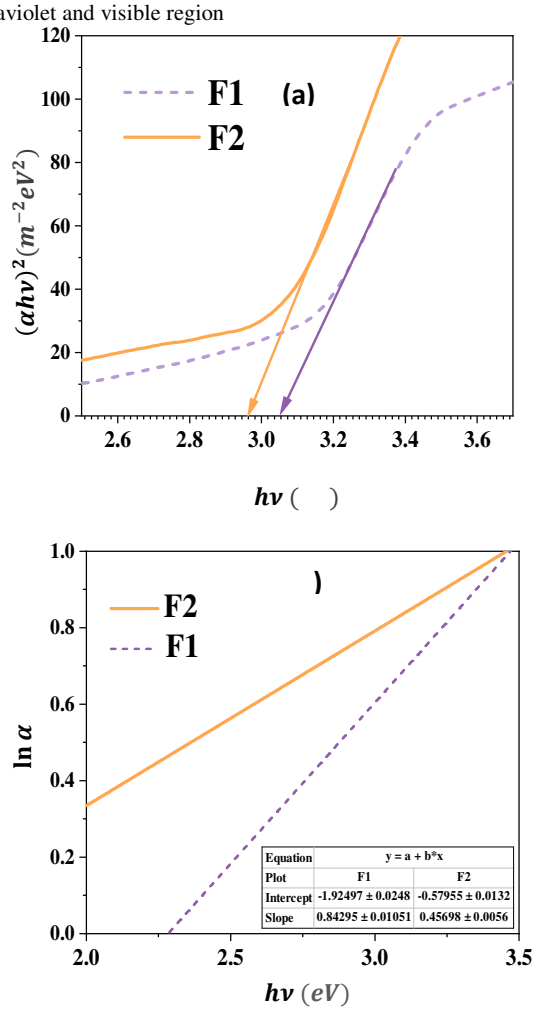

Figure 8. **(a) Tauc graph for ZnO samples; (b) Logarithmic plot of absorption coefficient versus photon energy**.

4 Conclusions

In summary, ZnO films are successfully prepared by pulsed laser deposition technique on the glass substrate. Structural and morphological results are affected by deposition rates based on SEM micrographs. The pulse repetition rate increases the deposition rate, the island density, and the film thickness. Furthermore, pulse

repetition rate influences the optical properties of the ZnO films by affecting the number of defects in their structures. As the results indicated, the laser fluency can affect the bandgap energy of the films and their defect densities.

References

[1] Sun, X. W., and Hoi Sing Kwok. "Optical properties of epitaxially grown zinc oxide films on sapphire by pulsed laser deposition." Journal of applied physics 86 (1999) 408.

[2] Kumar, Rajesh, et al. "ZnO nanostructured thin films: Depositions, properties and applications A review." Materials Express 5 (2015) 3.

[3] Alexiadou, M., et al. "Pulsed laser deposition of ZnO thin films decorated with Au and Pd nanoparticles with enhanced acetone sensing performance." Applied Physics A 123 (2017) 262.

[4] R. Eason, Pulsed laser deposition of thin films: applications-led growth of functional materials. seventh ed., John Wiley & Sons, 2007.

[5] Mousavi, Seyedeh Soraya, Batool Sajad, and Mohammad Hossein Majlesara. "Fast response ZnO/PVA nanocomposite-based photodiodes modified by graphene quantum dots." Materials & Design, 162 (2019) 249.

[6] Yu, Xinge, Tobin J. Marks, and Antonio Facchetti. "Metal oxides for optoelectronic applications." Nature materials, 15 (2016) 383.

[7] Efafi, Babak, et al. "A method for optimizing the electrical conductivity of Al: ZnO TCO films." Materials Letters, 195 (2017) 52.

[8] Mousavi, Seyedeh Soraya, et al. "Practical optimization of highly sensitive azo photoconductor with circular electrode scheme." Journal of Lightwave Technology, 36 (2018) 5800.

[9] Efafi, Babak, et al. "Fabrication of high-performance UVC photodiodes by Al+ 3 ion adjustment in AZO/Si heterostructures." Optical Materials, 81 (2018) 7.

[10] Liu, Y. C., S. K. Tung, and J. H. Hsieh. "Influence of annealing on optical properties and surface structure of ZnO thin films." Journal of crystal growth, 287 (2006) 105.

[11] Hussain, Saleem Azara, and Awatif Jabbar Radi. "Study the effect of film thickness on the structural and optical of (ZnO) thin film prepared by pulsed laser deposition." Journal of Physics: Conference Series, 1294 2 IOP Publishing (2019).

[12] Kumar, Rajesh, Girish Kumar, and Ahmad Umar. "Pulse laser deposited nanostructured ZnO thin films: a review." Journal of nanoscience and nanotechnology, 14 (2014) 1911.

[13] Soni, Ankit, Komal Mulchandani, and K. R. Mavani. "Crystallographically oriented porous ZnO nanostructures with visible-blind photoresponse: controlling the growth and optical properties." Materialia, 6 (2019): 100326.

[14] Jahromi, Khalil Eslami, et al. "Investigation of a reliable ohmic contact to n-type ZnO thin films prepared by sol-gel method." IEEE Electron Device Letters, 37 (2015) 43.

[15] Ji Nan Zeng, et al. "Effect of deposition conditions on optical and electrical properties of ZnO films prepared by pulsed laser deposition." Applied surface science, 197 (2002) 362.

[16] Ma, Shouzhi, et al. "Controlling the band gap of ZnO by programmable annealing." The Journal of Physical Chemistry C, 115 (2011) 20487.

[17] Lei Zhao, et al. "Structural and optical properties of ZnO thin films deposited on quartz glass by pulsed laser deposition." Applied surface science, 252 (2006) 8451.

[18] J. B. Franklin, et al. "Optimised pulsed laser deposition of ZnO thin films on transparent conducting substrates." Journal of Materials Chemistry, 21 (2011) 8178.

[19] Y. Esqueda-Barrón, M. Herrera, S. Camacho-López. "ZnO synthesized in air by fs laser irradiation on metallic Zn thin films." Applied Surface Science, 439 (2018) 681.

[20] Andrej Vincze, et al. "Growth and characterization of pulsed laser deposited ZnO thin films." Open Physics, 5 (2007) 385.

[21] Adawiya J. Haider, Allaa A. Jabbar, Ghalib A. Ali, "A review of Pure and Doped ZnO Nanostructure Production and its Optical Properties Using Pulsed Laser Deposition Technique." Journal of Physics: Conference

Series, 1795 IOP Publishing (2021).

[22] Wang Zhaoyang, Sun Liyuan, Hu Lizhong, "Effect of laser repetition frequency on the structural and optical properties of ZnO thin films by PLD." Vacuum, **85** (2010) 397.

[23] Francois Brygo, et al. "Laser fluence, repetition rate and pulse duration effects on paint ablation." Applied surface science, **252** (2006) 2131.

[24] Li Guan, et al. "Role of pulse repetition rate in film growth of pulsed laser deposition." Nuclear Instruments and Methods in Physics Research Section B: Beam Interactions with Materials and Atoms, **266** (2008) 57.

[25] Alejandro Ojeda-G-P, Max Döbeli, Thomas Lippert. "Influence of plume properties on thin film composition in pulsed laser deposition." Advanced Materials Interfaces, **5** (2018) 1701062.

[26] F. Hasani, M. Simdar, M. Amin Bassam, S. Soraya Mousavi, and B. Sajad, "Annealing Effects on Optical Properties Zinc Oxide (ZnO) Thin Films."Optics and Photonics Society of Iran, **25** (2019) 661.

[27] M. Simdar, F. Hassani, S. S. Mousavi, B. Sajad. "The effects of stable substrate temperature on the quality of ZnO films prepared by pulsed laser deposition." Nanoscale, **7** (2020) 25.

[28] Mehrnaz Simdar, et al. "Distinctive ZnO film's structures and morphologies for different modes of the heating substrate." Materials Letters, **297** (2021) 129914.

[29] P. S. Shewale, Y. S. Yu. "The effects of pulse repetition rate on the structural, surface morphological and UV photodetection properties of pulsed laser deposited Mg-doped ZnO nanorods." Ceramics International, **42** (2016) 7125.

[30] Jaroslav Bruncko, et al. "Pulsed laser deposition of Ga doped ZnO films-Influence of deposition temperature and laser pulse frequency on structural, optical and electrical properties." Vacuum, **159** (2019) 134.

[31] P. S. Shewale, S. H. Lee, and Y. S. Yu. "Pulse repetition rate dependent structural, surface morphological and optoelectronic properties of Ga-doped ZnO thin films grown by pulsed laser deposition." Journal of Alloys and Compounds, **725** (2017) 1106.

[32] Doris Segets, et al. "Analysis of optical absorbance spectra for the determination of ZnO nanoparticle size distribution, solubility, and surface energy." ACS nano, **3** (2009) 1703.

[33] S. Lemlikchi, et al. "Study of structural and optical properties of ZnO films grown by pulsed laser deposition." Applied Surface Science, **256** (2010) 5650.

[34] G. Wisz, et al. "Structural, optical and electrical properties of zinc oxide layers produced by pulsed laser deposition method." Nanoscale Research Letters, **12** (2017) 1.

[35] N. J. Ianno, et al. "Characterization of pulsed laser deposited zinc oxide." Thin Solid Films, **220** (1992) 92.

Journal of Interfaces, Thin films, and Low dimensional systems 4 (1) Summer and Autumn (2020) 339-346

Spin-orbit interactions at finite temperature in low dimensional bound states

Scientific research paper

Arezu Jahanshir

Department of Physics and Engineering Sciences, Imam Khomeini International University, Buein Zahra Higher Education Centre of Engineering and Technology, Iran

ARTICLE INFO

Article history:
Received 15 July 2021
Revised 4 August 2021
Accepted 5 August 2021
Available online 26 October 2021

Keywords:
Bound state
Excitation
Relativistic mass
Spin interactions

ABSTRACT

Spin-orbit interactions of exciton relativistic bound states at a finite temperature in the framework of the projective unitary representation in a physics model with the Coulomb potential have been investigated. The ground state of the system in order to describe the temperature effect in a low dimension environment has been defined. The bound state, with electron-hole pair, has attracted a great deal of interest in thin-films and nanophysics. The reality of the state has been the subject of intense concern among theoreticians and experimenters in recent years. Spin-orbit interactions of exciton are considered to be in an electron-hole pair bound state. The problem of spin interactions of coupled states based on the quantum field theory in its widest sense is a method to control and achieve reasonable goals; and in this article, the problem is examined in details. The structure of the interaction Hamiltonian with the Coulomb type potential at finite temperatures is defined and then the mass and energy spectra of an exciton based on the spin interactions are determined theoretically. The defined properties at finite temperature can be used for new high technology materials of semi-conductive features for electronics, microelectronics, photovoltaic or solar cell manufacturing, and semiconductor chips.

1 Introduction

One of the well-known methods of considering interactions of the exciton state in low dimension thin films and materials was proposed in 1995, where the asymptotic of Green's function was obtained in the exponential form of propagators in an external field [1,2]. The method is applied to the basic fundamental model of quantum electrodynamics and quantum field theory. The polarization closed loop function through a functional integral is presented in this approach; this functional integral cannot be calculated as usual; in this case, we have to simplify physical assumptions as done in [1-4]. An alternative method of calculating the functional integral and determining the exciton properties at finite temperatures is defined in the quantum field theory. The finite temperature-dependent in a low dimension environment like thin films is a very important subject in theoretical and experimental physics.

Progress of exotic bound state physics in low dimensional transition semiconductor quantum dots allows exotic constructions, including poly-excitonic

*Corresponding author.
Email address: jahanshir@bzeng.ikiu.ac.ir
DOI: 10.22051/jitl.2021.36935.1057

systems, to be synthesized [1,2]. Specifically, a finite number of poly-excitons can be confined in a bounded volume of the order of normal-sized low-dimensional materials at a finite temperature. Therefore, the poly-excitonic environments have recently gained attention in theoretical investigations and experimental explorations. Theoretical physicists are interested in the possibility of controlling the properties of these materials at finite temperatures that could be implemented in new high technology materials of semi-conductive and conductive features for electronics, microelectronics, fuel cell production, photovoltaic or solar cell manufacturing, and semiconductor chips. The electron-hole state is the simplest model of bounding states to use when studying the essential features of ploy excitonic systems. Recently, the study of excitons has progressed significantly.

Among poly excitonic systems in low dimensional thin films, spin-orbit interactions of two exciton pairs are especially interesting because of their interaction effects in bound states. Many new poly excitonic bound states have been recently discovered following developments at finite temperatures and higher bandgaps making poly excitonic states to become the main topic of studies on low dimension materials and thin films. Many theoretical works have focused on determining or predicting the relativistic properties and conditions of poly excitonic states.

The present article investigates the asymptotic behavior of the correlation functions of charged fields and the analytic method for determining properties of poly excitonic states in a low dimension material at a finite temperature. According to the results, in the poly excitonic system, the total mass of the bound state differs from hole and electron masses in a free state. This work represents a theoretical and analytical effort where its outcome provides fundamental quantities of the poly excitonic electron-hole bound states. This outcome leads to make several predictions of the excitons in low dimension thin films and semiconductor quantum dots at a finite temperature. We choose to use the strong Coulomb interaction at a finite temperature as it plays a significant role in thin-film physics. The Schrodinger equation solutions for the Coulomb potential are known and can be obtained using various methods. In this article, we calculate the effect of the spin-orbit interaction in the bound state of poly excitonic systems in the ground state. Various analytical or numerical approximation methods have been developed to compensate for the fact that the relativistic Schrodinger equation for such a system does not produce solutions. In this way, one can demonstrate the projective unitary representation in physics [3,4] when calculating the properties of poly excitonic states. This technique can be used to accurately describe the characteristics of poly excitonic systems in thin films at finite temperatures. Thus, it is essential to develop the projective unitary representation in low dimension physics, as it describes the bound-state characteristics of systems such as exciton, diexciton, and poly excitonic systems.

2 Materials and methods

2.1 Mass spectrum in the relativistic limit

To define spin-orbit interactions in the poly-excitonic bound states at low dimensional materials at a finite temperature based on quantum electrodynamic filed and photon interaction wave function between electron-hole, we have to describe the main formula which contains the mass and energy eigenvalues. The temperature relation for the one-photon exchange (Coulomb potential) describes the new characteristic of the poly excitonic bound state in low dimension thin films and materials [2,5,6].

We try to describe interaction in temperature-dependent conditions by modified radial Schrödinger equation and using the analytic method based on the behavior of the correlation function of a photon at a finite temperature in the electromagnetic field. The determination of mass spectrum of poly excitonic systems is suggested within this idea where the binding energy and mass of the bound states are determined. The exciton-exciton, three excitons, etc. states include those which fit in the well-known states. They include in the multi-electron-hole states.

The exciton bound system is an electron-hole state that has been studied in the electrostatic field and framework methods such as the Gaussian expansion method, the quantum electrodynamics sum rules, and the Lattice quantum dynamics. Therefore, based on the quantum electrodynamic models and quantum field theory we can determine that the electron-hole system is one of the most crucial states which makes it possible to form

bound states of gauge bosons at low/high finite temperatures.

In this article, we show that the mass spectrum of the exciton state is extremely higher than predicted in theory at a finite temperature. We study exciton spin-orbit interactions at a finite temperature using the Gaussian asymptotic [2,3] behavior of the correlation functions of the corresponding field currents for the determination of the energy and mass spectrum in the ground state with the spin interactions in the Coulomb potential at a finite temperature. The mass spectrum and the constituent mass of the electron-hole system are determined from the modified Schrödinger equation for Hamiltonian of the Schrödinger equation [5,6]

$$\widehat{H}R(r) = MR(r) = E_0(\mu)R(r). \quad (1)$$

Now we describe the method: as we know, in the quantum field, the mass of the coupled particles is presented by the Gaussian shape of the correlated-current function and the exact orbital quantum numbers. The statistical correlation, in terms of the Green function $G(r)$, is expressed. It is defined as a functional integral and allows the necessary Gaussian limit to be allocated before one can carry out the average value of the external gauge field.

In nonrelativistic quantum mechanics, the resulting image of presentation is similar to the Feynman functional path integral. Hence, the mass of coupled electron-hole is determined by the polarization function (statistical correlation)

$\Pi(r) = \left\langle G_e(r|A)G_h^*(r|A)\right\rangle_A$, and the Green's function $G(r)$ [5]. We know, the current of scalar charged particles is $J(r) = R^+(r)R^-(r)$ where it is convenient to represent the considered correlators as the average over the gauge field $A(r)$ of a product of the Green's functions of the scalar charged electron hole in the electromagnetic field. The Green's function of the scalar charged electron and hole is defined by the equation

$$\left[\left(i\frac{\partial}{\partial r} + \frac{g}{c\hbar}\right)^2 + \frac{c^2m^2}{\hbar^2}\right]G(r|A) = \delta(r). \quad (2)$$

Solution of the Green's function is described in the functional integral form (for full detail see [2])

$$G(r|A) = \int_0^\infty dt\, \exp\{-m^2\alpha\}T_\tau \times \exp\left\{-t\int_0^1 d\tau\left(i\frac{\partial}{\partial r(\tau)} + gA\left(r(\tau)\right)\right)^2\right\}\delta(r). \quad (3)$$

Also, we know the coupled gluon-gluon mass spectrum is explain in relativistic-quantum theory by the polarization function (for full detail see [2])

$$\Pi(x) = A\cdot J_\mu(\mu) = \int_0^\infty\int_0^\infty \frac{du_1 du}{(8r\pi)^2}\exp\left\{-r\left(\frac{m^2}{\mu} + \mu\right)\right\}J_\mu(\mu),$$

where

$$J(\mu) = = N_1N_2\iint \delta r_1\delta r_2\exp\left\{-\frac{1}{2}\int_0^r d\tau\left(\mu\dot{r}_1^2(\tau) + \mu\dot{r}_2^2(\tau)\right)\right\}\exp\{-W_{1,1} + W_{1,2} - W_{2,2}\}.$$

The functional integral $J(\mu)$ looks like the Feynman path integral in nonrelativistic quantum mechanics for four-dimensional motion of particles with reduced mass μ. The interaction of these particles is defined by the nonlocal functional $W_{i,j}$ which contains potential and nonpotential interactions. The asymptotic of the function $J_\mu(\mu)$ looks like $J_\mu(\mu)\sim e^{(-rE_\ell(\mu))}$. Thus, we obtain:

$$\Pi(r) \cong\Rightarrow \exp\left(-M\sqrt{\Pi(r)^2}\right),$$

$$M = -\lim_{|r|\to\infty}\frac{\ln\Pi(r)}{|r|}. \quad (4)$$

After simplifying the equation, the mass spectrum reads ($i = 1,2$)

$$M = \frac{\partial}{\partial\mu_i}\left(\left(\frac{\mu_2m_1^2 + \mu_1m_2^2}{2\mu_1\mu_2}\right) + \frac{\mu}{2} + E(\mu)\right). \quad (5)$$

Therefore, the electron-hole system with the rest mass ($m_1 = m_e, m_h = m_2$), the exciton bound state mass in the stationary state reads

$$M = \frac{\partial}{\partial \mu_1}\left(\frac{\mu_2 m_1^2 + \mu_1 m_2^2}{2\mu_1\mu_2} + \frac{\mu}{2} + E_\ell(\mu)\right),$$

$$M = \frac{\partial}{\partial \mu_2}\left(\frac{\mu_2 m_1^2 + \mu_1 m_2^2}{2\mu_1\mu_2} + \frac{\mu}{2} + E_\ell(\mu)\right),$$

$$\mu = \frac{\mu_1 + \mu_2}{\mu_1\mu_2}. \tag{6}$$

By using the Taylor approximation one can determine the parameters $i = 1,2$ as follows

$$\mu_i = \frac{\partial M}{\partial \mu_{1i}} = 0 \Rightarrow$$

$$\mu_{1=}\sqrt{m_1^2 + \mu^2\left(\frac{e^2}{\mathcal{D}\pi\varepsilon_r}\right)^2} \rightarrow$$

$$\mu_{e=}\sqrt{m_e^2 + \mu^2\left(\frac{e^2}{\mathcal{D}\pi\varepsilon_r}\right)^2} \rightarrow$$

$$\mu^*{}_{e=}\sqrt{m_e^{*2} + \mu^2\left(\frac{e^2}{\mathcal{D}\pi\varepsilon_r}\right)^2},$$

and

$$\mu_{2=}\sqrt{m_2^2 + \mu^2\left(\frac{e^2}{\mathcal{D}\pi\varepsilon_r}\right)^2} \rightarrow$$

$$\mu_{h=}\sqrt{m_h^2 + \mu^2\left(\frac{e^2}{\mathcal{D}\pi\varepsilon_r}\right)^2} \rightarrow$$

$$\mu^*{}_{h=}\sqrt{m_h^{*2} + \mu^2\left(\frac{e^2}{\mathcal{D}\pi\varepsilon_r}\right)^2}, \tag{7}$$

where m_e^*, m_h^* are the electron and hole effective mass, and m_e, m_h are the electron and hole rest mass. Based on the electron-hole interaction we use the effective mass, constituent mass, and reduced mass as expressed by $m_e^* = m_e, m_h^* = m_h$, in the following expressions

$$\mu = \mu^* = \frac{\mu^*{}_1 + \mu^*{}_2}{\mu^*{}_1\mu^*{}_2},$$

$$\mu^*{}_1 = \mu{}_1.\mu^*{}_2 = \mu{}_2,$$

and also from Eq. (4) we define

$$E_\ell(\mu) = M - \frac{1}{2}((\mu_e + \mu_h) - \frac{m_e^2\mu_h + m_h^2\mu_e}{2\mu_e\mu_h},$$

$$E'_\ell = \frac{dE_\ell}{d\mu}. \tag{8}$$

as we know that $J_\mu(\mu) \sim e^{(-rE_\ell(\mu))}$.

In Eq. (7) the particle's effective mass (denoted by m^*} is the mass that it seems to have when responding to forces, or the mass that it seems to have when interacting with other identical particles in a thermal distribution. One of the results from the bound state theory of exciton is that the movement of electron-hole in a potential field can be very different from their motion in a vacuum [7]. The effective mass is a quantity that is used to describe exciton's bound states by modeling the behavior of a free particle (electron-hole) with that mass. For some purposes and some nanomaterials, the effective mass can be considered to be a simple constant of a material while the value of effective mass depends on the purpose for which it is used, and can vary depending on several factors [7] especially in nano quantum dots. For electrons or electron holes in a solid, the effective mass is usually stated in units of the rest mass of an electron (9.11×10−31 kg). In these units, it is usually in the range 0.01 to 10, but can also be lower or higher—for example, reaching 1000 in exotic heavy fermion materials, or anywhere from zero to infinity (depending on definition) in graphene. As it simplifies the more general band theory, the electronic effective mass can be seen as an important basic parameter that influences measurable properties of a solid, including everything from the efficiency of a solar cell to the speed of an integrated circuit.

3 Schrödinger equation for the bound state

The radial Schrödinger equation for the multiplex system with Coulomb interaction is [5]:

$$H = H_0 + \hat{H}_{spin} =$$

$$\frac{1}{2}\sum_{i=1}^{n} m_i\, v_i^2 + \sum_{i=1}^{n-1} V_{i<j} + \hat{H}_{spin}. \qquad (9)$$

Now, for defining characteristics of the excitonic systems in the electromagnetic field interactions, we use the bound state in the electrical confining potential at the finite temperature $V(r,T) = -\frac{a(r,T)}{r}$ [7]. In this case, using the modified radial relativistic Schrödinger equation (Eq. (9)), we have

$$\hat{H}R(r) = MR(r) = E_\ell(\mu)R(r).$$

$$MR(r) = \left(\sqrt{m_e^2 + \hat{p}_r^2} + \sqrt{m_h^2 + \hat{p}_r^2} + \right.$$

Now, we explain the relativistic effects on the bound states using explanations *I* and *II*:

$$I.\ \sqrt{m^2 + \hat{p}_r^2} = m\sqrt{1 + \frac{\hat{p}_r^2}{m^2}} \approx$$

$$\approx m + \frac{\hat{p}_r^2}{2m} - \frac{\hat{p}_r^4}{8m^3} + \cdots,$$

$$II.\ \sqrt{m^2 + \hat{p}_r^2} \approx \min_{\mu}\left(\mu + \frac{m^2 + \hat{p}_r^2}{\mu}\right).$$

Two approximate methods are usually used for predicting the structure of the bound states before obtaining the Hamiltonian of the bound state as ($\hbar = c = 1$)

$$\left[\frac{1}{2}\left(\mu_1 + \frac{m_e^2 + \hat{p}_r^2}{\mu_e}\right) + \frac{1}{2}\left(\mu_2 + \frac{m_h^2 + \hat{p}_r^2}{\mu_h}\right) + \frac{a(r.T)}{r}\right]R(r) = MR(r). \qquad (11)$$

or

$$\left[\frac{\hat{p}_r^2}{2\mu} + \frac{a(r.T)}{r}\right]R(r) = \left[M - \frac{1}{2}(\mu_e + \mu_h) - \frac{m_e^2\mu_h + m_h^2\mu_e}{\mu_e\mu_h}\right]R(r), \qquad (12)$$

where μ is the reduced mass and $\mu_{e,h} is$ the constituent mass of particles in the bounding system. The n-dimensional modified Schrödinger equation could be presented using [8-10]

$$\frac{1}{2r^{n-1}}\frac{d}{dr}\left(r^{n-1}\frac{d}{dr}\right)R(r) - \frac{\ell(\ell+n-2)}{2r^2}R(r) + \mu V(r.T)R(r) + \mu\left(M - \frac{1}{2}(\mu_e + \mu_h) - \frac{m_e^2\mu_h + m_h^2\mu_e}{\mu_e\mu_h}\right)R(r) = 0. \qquad (13)$$

Spin-orbit interactions at finite temperature in low dimensional bound states can be presented in the potential types: Cornell, Coulombic, and strong interactions by the exponential relations [8]. The Coulomb-temperature potential is described by the exponential function $V(r,T) \approx -\frac{1}{r}\exp(-a(T)\mu(T)r)$ the reduced mass [7] at $T \neq 0$. Using the approximation of the exponential function

$$\exp(-a(T)\mu(T)r) = \sum_{n=0}^{\infty}\left(\frac{(-a(T)\mu(T)r)^n}{n!}\right),$$

we obtain

$$V(r,T) \approx -\frac{1}{r} + \alpha(T)\mu(T) - \beta(T)(\mu(T))^2 r + \ldots$$

Therefore, the Hamiltoni of the exciton system is as follows [11,5]

$$\left[\frac{-1}{2\mu}\left[\frac{\partial^2}{\partial r^2} + \frac{2}{r}\frac{\partial}{\partial r} - \frac{\hat{\ell}}{r^2}\right] + + \frac{(-1 + \alpha(T)\mu(T)r - \beta(T)(\mu(T)r)^2)}{r} + H_{spins}\right]R(r) = E_0(\mu)R(r). \qquad (14)$$

One can describe the exact temperature relation in the Coulomb potential by

$$V(r,T) = Be^{-\mu(T)r} =$$

$$= B\left(1 - \mu(T)r + \frac{(\mu(T)r)^2}{2}\right).$$

We modify the variables in the starting Schrödinger equation based on the projective unitary representation method in the quantum field theory for the ground state at a finite temperature with described spin-orbit interactions. This state is described as an infinite number of oscillators that keep their oscillating character in interactions.

To use quantum field methods, we have to change variables in Eq. (14) for the linear interaction terms of the Coulomb potential by replacing a new variable in the $\mathcal{D}$-dimensional axillary space. Now, based on the asymptotic properties $(r \to \infty, r \to 0)$ of Gaussian type $r = q^{2\rho}$ and $R(r) \to R(r) = q^{2\rho}R(q^2)$, where ρ is a parameter to be determined; in the charge potential such a modification is performed by $\rho \cong 1$ where the electron-hole wave function becomes an oscillator. Using the radial Laplacian operator in the n-dimension space one can define the radial Laplacian operator in the $\mathcal{D}$-dimensional ($\mathcal{D} = 2\rho + 2$) axillary space [2]:

$$\Delta_r = \frac{d^2}{dr^2} + \frac{n-1}{r}\frac{d}{dr} \to$$

$$\Delta_q = \frac{d^2}{dq^2} + \frac{\mathcal{D}-1}{q}\frac{d}{dq}.$$

where

$$\frac{d}{dr} = \frac{dq}{dr}\frac{d}{dq} = \left(\frac{d}{dr}\left(r^{\frac{1}{2\rho}}\right)\right)\frac{d}{dq} = \left(\frac{1}{2\rho}q^{1-2\rho}\right)\frac{d}{dq},$$

$$\frac{d^2}{dr^2} = \frac{d}{dr}\frac{d}{dr} = \left(\frac{1}{4\rho^2}q^{2-4\rho}\right) \times \left(\frac{d^2}{dq^2} + \frac{1-2\rho}{q}\frac{d}{dq}\right).$$

Here, the wave function should have the Gaussian type solution for large distances and we apply the projective unitary representation method variables from $R(r) \to q^{2\rho}R(q^2)$ and the transformation canonical variables as Wick ordering creation and annihilation operators (see [2] for more details) $\hat{q} = \frac{\hat{a}^- + \hat{a}^+}{\sqrt{2\omega_0}}$, $\hat{p}_q = \sqrt{\frac{\omega_0}{2}}\frac{\hat{a}^- - \hat{a}^+}{i}$, then determine

$$q^2 = \frac{\mathcal{D}}{2\omega_0}, \quad q^4 = \frac{\mathcal{D}(\mathcal{D}+2)}{4\omega_0^2}, \quad p^2 = \frac{\mathcal{D}\omega_0}{2}$$

and define the Hamiltonian (14). Equation (14) in a new auxiliary space is obtained

$$\begin{aligned}\varepsilon_0(E_\ell, T) = \frac{\hat{p}_q^2}{2}R(q^2) \\ + 4\mu q^2 H_{spin}R(q^2) - 4\mu q^2 E_0 R(q^2) \\ + (-4\mu + 4\alpha\mu^2 q^2 - 4\beta\mu^3 q^4)R(q^2) \\ = 0\,. \end{aligned} \quad (17)$$

Now, we can find the renormalization of the bound state parameters like wave function which allows us to introduce the zero approximation in the projective unitary representation method and then find the eigenvalue of the ground state energy $\varepsilon_0(E_0)$. Thus, Eq. (17) is written in the form

$$\varepsilon_0(E_0.T) = X(T.\omega_0) - E_0 Y(T.\omega_0) = 0,$$

or

$$\varepsilon_0(E_0.T) = \left(\frac{\mathcal{D}}{4}\omega_0 - 4\mu + \right.$$

$$+\frac{2\mu\mathcal{D}}{\omega_0}[3\nabla_r V(r)](\hat{L}\hat{S}) + \frac{2\mu\mathcal{D}}{\omega_0}[\Delta_r V(r)](\hat{S}_e\hat{S}_h)$$

$$\left. +\frac{2\alpha\mu^2\mathcal{D}}{\omega_0} - \frac{\beta\mu^3\mathcal{D}(\mathcal{D}+2)}{\omega_0^2}\right) - \frac{2\mu\mathcal{D}}{\omega_0}E_0 = 0, \quad (18)$$

where we suppose $\hat{S}_+ = \hat{S}_1 + \hat{S}_2$ $(\hat{S}_1 = S_e\,,\ \ \hat{S}_2 = S_h)$ for the sum of two particles' spin in the exciton system (spin-orbital and spin-spin equations) where we will have

$$H_{spin} = H_{LS} + H_{SS} \to$$

$$H_{LS} = \frac{2\mu\mathcal{D}}{\omega_0}[3\nabla_r V(r)](\hat{L}\hat{S}),$$

$$H_{LS} = \frac{2\mu\mathcal{D}}{\omega_0}[\Delta_r V(r)](\hat{S}_1\hat{S}_2),$$

$$j = \ell + S,$$

$$(\hat{S}_1\hat{S}_2) = \frac{\left(S(S+1) - S_1(S_1+1) - S_2(S_2+1)\right)}{2}, \qquad (19)$$

$$(\hat{L}\hat{S}) = \frac{\left(j(j+1) - S(S+1) - \ell(\ell+1)\right)}{2},$$

where based on the projective unitary representation conditions (Eq. (18)), we find

$$\varepsilon_0(E_0, T) = 0, \quad \frac{d\varepsilon_0(E_0,)}{d\omega_0} = 0, \qquad (20$$

)and the ground state energy$E_0 = E_0(\mu.T)$ and also the pure oscillator frequency of the exciton system in the ground state $\omega_0 = \omega_0(E_0, T)$ at a finite temperature. The pure oscillator frequency of the exciton system in the Coulomb potential without temperature relation reads $\omega_0 = \sqrt{-8\mu\, E(\mu)}$. Thus, using formulas (18, 20) and (7), then one can determine the mass spectrum of the predicted bound state. Based on Eq. (20), the electron-hole system as an exciton bound state solution by the radial modified Schrödinger equation at a finite temperature has been described. For this opinion, the projective unitary method of the Schrödinger equation is used. The behavior of the exciton bound state at a high temperature is very important in low dimension materials and thin-film environments. We have presented the bound state spin-orbit and relativistic mass spectrum based on quantum field theory and have determined the relationship between mass spectrum and temperature in the Coulomb type potential at a finite temperature. The temperature-dependent radial modified Schrödinger equation is investigated by applying the projective unitary method in the ground state wave function of the exciton bound system ($\ell = 0, \mathcal{D} = 3$). Now, we determine the finite temperature as described by [2,12] nonzero and zero temperature spin interactions and mass spectrum of the electron-hole. Theoretically, results for the spin-orbit interactions are presented. Results are used for describing

$$R_0 = A(\mu\,\omega_0(E_0, T))^{\frac{3}{2}} \exp\left(-\mu\frac{3}{4}\right). \qquad (21)$$

The temperature-dependent of exotic electron-hole bound state in Molybdenum disulfide (or moly) QDs are currently fascinating subjects in SQDs physics. Therefore, based on Eqs. (17)-(19) we calculate the mass spectrum of moly QDs with and without spin-orbit interactions at the finite temperature that corresponds to the in-plate directions of the dielectric constant ($\varepsilon_{r||}$). The mass spectrum of exciton in the 1s, 2s, and 3s states for Molybdenum disulfide quantum dots as a function of temperature based on spin-orbit interactions is presented in Fig. 1. We may conclude that our current results as presented in Fig. 1, are in good agreement with currently available experimental data for all states of exotic exciton bound state in nano quantum dots [15]. The present paper proposed a method for theoretically determining the relativistic mass spectrum of exciton at finite a temperature with spin interactions and also energy eigenvalue within the framework of the QFT, QED. An analytic expression was given for masses of exotic systems while considering relativistic corrections.

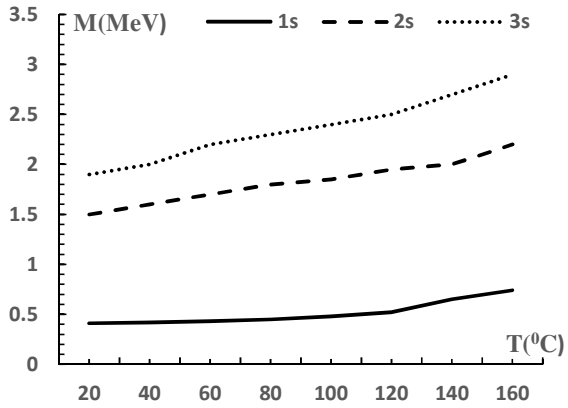

Figure 1. The mass spectrum of exciton in 1s, 2s, and 3s states as a function of temperature based on spin-orbit interactions.

4 Conclusions

The spin-orbit interactions and the relativistic correction to the mass of the electron-hole bound state at a finite temperature in low dimension materials and thin-films under the projective unitary representation are defined theoretically. For determining the spin-orbit interactions at a finite temperature we used the Coulomb potential-temperature relation as an exponential function and modified the radial Schrödinger equation. The formulas show that the high-temperature environment, can be affected by the characteristics of the electron-hole bound state in thin firms.

Based on the description method one can conclude that the theoretical results of this work are expected to define new possibilities and properties of thin films at a finite

temperature which can be used for new materials, microelectronics production, and semiconductor chips.

The obtained theoretical data can be useful in today's researches and can open high perspectives to determine the new characteristics of poly-excitonic systems. We have studied the exciton properties in thin films at finite temperatures. We have calculated the constituent mass of particles based on relativistic correction to the mass. In the above calculations, we have theoretically found that the relativistic behavior on the mass of electron-hole in the exciton system increases with increasing temperature. The mass of the exciton system in 1s, 2s and 3s states as a function of temperature based on spin-orbit interactions are determined and calculated. Based on $\omega_0 = \sqrt{-8\mu\, E(\mu)}$. The ground state amplitude at finite temperature $T > T_0$ will be higher than the amplitude at T_0 (T_0 is the laboratory or room temperature or usually either (T_0 =20÷25 C).

Acknowledgements

This work was supported by scientific programs of the department of physics and engineering sciences, Buein Zahra Technical University.

Funding

This work was supported by scientific programs of the department of physics and engineering sciences, Buein Zahra Technical University under the grant 1999 for developing research.

References

[1] M., Rushka, J., Freericks, "A completely algebraic solution of the simple harmonic oscillator". Am. J. Phys. **88** (11) (2019) 976.

[2] M. Dienykhan, G. Efimov, G. GanboldS, N. Nedelko, "Oscillator Representation in Quantum Physics (Lecture Notes in Physics Monographs)." 1st ed. Springer International Publishing (1995).

[3] D. Fujiwara, "Rigorous Time Slicing Approach to Feynman Path Integrals." 1st ed. Springer International Publishing (2017).

[4] J. Kelley, J. Leventhal, "Ladder Operators for the Harmonic Oscillator. Problems in Classical and Quantum Mechanics." Springer International Publishing (2017).

[5] A. Jahanshir, "Quanto-Optical Effects of Exciton-Polariton System." American Journal of Optics and Photonics, **3** (2015) 89; W. Lucha, F. F. Schoberl, D. Gromes, "Bound states of quarks." Physics Reports, **200** (1991) 127.

[6] R. Gould, "Quantum Electrodynamics. Electromagnetic Processes." 1st ed. Springer-Verlag (2020).

[7] A. Jahanshir, "Relativistic Modification of the Exciton's Mass in Monolayer TMDCs Materials." Journal of Advanced Materials and Processing, **8** (2020) 45.

[8] A. Maireche, "A theoretical investigation of nonrelativistic bound state solution at finite temperature using the sum of modified Cornell plus inverse quadratic potential." Sri Lankan J Physics, **21** (2020)11.

[9] F. Rodríguez-Dueñas, "Optical and transport properties of cuasi-one dimensional electronic systems." Revista de la Academia Colombiana de Ciencias Exactas, Físicas y Naturales, **46** (2018) 150.

[10] R. Meulenberg et al., "Determination of the exciton binding energy in CdSe quantum dots," ACS Nano, **3** (2009) 325.

[11] K. Heyong-chan et al., "New Variational Perturbation Theory Basedonq−Deformed Oscillator." International Journal of Theoretical Physics, **45** (2006) 1017.

[12] A. Taqi, J. Diouri, "A theoretical model for exciton binding energies in rectangular and parabolic spherical finite quantum dots." Semiconductor physics quantum electronics & optoelectronics, **15** (2012) 365.

[13] M. Richard et al., "Exciton-polariton Bose-Einstein condensation: advances and issues", International journal of nanotechnology, **7** (2010) 668.

[14] M. Dharma-wardana et al., "Correlation functions in electron-electron and electron-hole doublequantum wells: temperature, density and barrier-width dependence." arXiv:1901.00895v1 [cond-mat.mes-hall] (2019).

[15] A., Tanveer Karim, et al., " Temperature dependency of excitonic effective mass and charge carrier conduction mechanism in $CH_3NH_3PbI_{3-x}Cl_x$ thin films", Scientific Reports, **11** (2021) 1.

Journal of Interfaces, Thin films, and Low dimensional systems 4 (1) Summer and Autumn (2020) 347-356

The influence of deposition rate on optical and microstructural characteristics of nanostructured ZnSe films prepared by thermal evaporation technique

Scientific research paper

Soodeh Momeni[1], Mohsen Ghasemi[1,2*], and Afrouz Taherian[3]

[1]*Department of Physics, Faculty of Sciences, Shahrekord University, Shahrekord, Iran*

[2]*Nanotechnology Research Institute, Shahrekord University, Shahrekord, Iran*

[3]*Faculty of Physics, University of Isfahan, Isfahan, Iran*

ARTICLE INFO

Article history:
Received 24 May 2021
Revised 18 August 2021
Accepted 28 August 2021
Available online 30 October 2021

Keywords:
Thermal evaporation technique
Nanostructured ZnSe films
Deposition rate
Optical properties
Microstructural properties

ABSTRACT

In this research, ZnSe thin films were deposited on glass substrate by the thermal evaporation method with deposition rates of 0.2, 0.4, 0.6, and 0.8 nm/s and with a constant thickness of 250 nm. All samples were annealed for 100 minutes at a temperature of 400 °C. Various techniques such as UV–Vis spectrophotometer, X-ray diffraction (XRD) analysis, and scanning electron microscope (SEM) were used to investigate different physical parameters such as energy band gap, refractive index, extinction coefficient, dielectric constant, and porosity of the ZnSe thin films. The influence of the deposition rate on the mentioned parameters was investigated. The XRD patterns showed that the ZnSe thin films have a cubic structure. The structural parameters such as lattice constant, crystallite size, strain, and dislocation density were determined for different samples. The maximum average transmittance of %93.1 in the visible wavelength region was obtained for the deposition rate of 0.6 (nm/s). The optical band gap was calculated using the derivation of absorption spectrum fitting (DASF) method, and the values of the energy band gap were obtained in the range of 3.71 ± 0.01 to 3.98 ± 0.01 eV. The XRD results acquired from the Williamson-Hall method showed that the crystallites size and strain of different samples were achieved in the range of 21.6 ± 1.1 to 42.9 ± 2.3 nm and $(0.61\pm0.02)\times10^{-3}$ to $(2.89\pm0.04)\times10^{-3}$, respectively. Finally, the relation between the optical and microstructural properties of the ZnSe films was studied.

1 Introduction

In recent years, thin-film science has grown considerably among various scientific domains as much research has been done in this field. Among optical thin films, semiconductors play an important role. ZnSe is a semiconductor of two known compounds with a bright yellow color that has two hexagonal and cubic crystalline structures [1]. This compound has high chemical stability, and it's interesting properties include a wide band gap, high refractive index, and high optical sensitivity [2–5]. Based on these special properties, ZnSe has various applications in thin film solar cells as buffer layer [6–8], cell imaging, humidity and gas sensors [9], thin film transistors [10], lasers [11], photo-detectors [12], blue-green zone of visible wavelength in light-emitting diodes [13], field emitter [9], and hydrophobic coating [14]. Therefore, the study of optical properties and detailed structural analysis are important to provide knowledge on the promising ZnSe material. Different methods have been used to

*Corresponding author.
Email address: Ghasemi.mohsen@sku.ac.ir, mphdghasemi@Gmail.com
DOI: 10.22051/jitl.2021.36255.1054

deposition of ZnSe thin films, such as RF magnetron sputtering [15], spray pyrolysis [16], chemical bath deposition [17], molecular beam epitaxy [18], and vacuum evaporation [19].

The ZnSe thin film prepared with the thermal evaporation technique are uniform and adherent. The optical and microstructural properties of ZnSe thin films have been investigated by some growth conditions such as substrate temperature, thickness, and post-deposition annealing temperature [20]. To the best of our knowledge, according to the literature, less attention has been paid to the effect of deposition rate on optical and microstructural properties of ZnSe thin films deposited by the thermal evaporation technique. In this research, the effect of deposition rate on the various parameters such as transmittance, reflectance, optical band gap, extinction coefficient, refractive index, real and imaginary dielectric constants, lattice constant, crystallite size, strain, and dislocation density of the ZnSe thin films, is investigated. Since the relationship between them is not yet fully understood and requires further research, in this work, an appropriate correlation is established between the various parameters, including the optical and microstructural properties of ZnSe thin films. We also attempt to express the interpretation for each of the phenomena that occurrs in different sections.

2 Experimental details

In this study, ZnSe thin films are deposited on the glass substrate. The cleanliness of the substrate surface is very important and affects the uniformity, optical and structural properties of the film. For cleaning of the substrate surface, the substrates were washed sequentially, in acetone, ethanol, isopropanol, Methanol, and then deionized water in an ultrasonic apparatus (Parsonic 2600s, Pars Nahand Engineering Company) for ten minutes. The substrates were placed in a vacuum chamber after drying with nitrogen gas flow. The thermal evaporation system (Yar Nikan Saleh Company, Iran) was used for film deposition. The vacuum chamber is depleted to the base pressure of $2\times10^{-5}\,mbar$. The ZnSe powder (Sigma Aldrich Company) was used as the target material with 99.99% purity. The thickness of the films and deposition rate were controlled using the quartz crystal system. Samples were prepared at ambient temperature and deposition rates of 0.2, 0.4, 0.6 and 0.8 nm/s and in the same thickness of 250 nm. All samples were annealed in a vacuum with the same conditions at 400 °C for 100 minutes after the growth process to improve the optical properties of ZnSe thin films. The image of the fabricated samples at different deposition rates, before and after the annealing process, is shown in Fig. 1. Transmittance data and optical reflection of the films were measured by a double-beam spectrophotometer (Shimadzu UV-3100 model). The microstructure of ZnSe films was determined using X-ray diffraction (XRD, X′ Pert-Pro MPD, Panalytical Company) and the surface morphology of ZnSe films was determined using Scanning Electron Microscope (SEM, VEGA-TESCAN-LMU model).

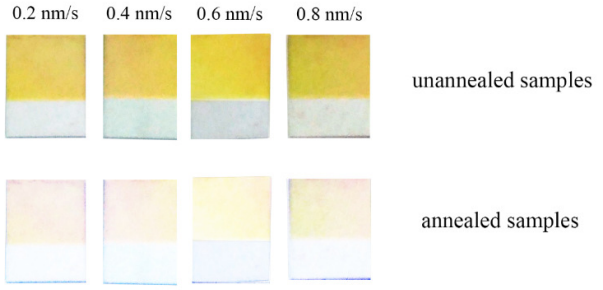

Figure 1. Image of the fabricated ZnSe thin films at different deposition rates, before and after the annealing process.

3 Discussion

The transmission (T) of ZnSe thin films was measured versus wavelength (λ) using a spectrophotometer apparatus. The transmittance of the samples, with various deposition rates before and after the annealing process, is shown in Figs. 2a and 2b, respectively. The presence of ripples in Fig. 2a can illustrate the interference effects inside the film. Thin film interference is a phenomenon in which light waves reflected from the upper and lower boundaries of a thin film interfere with each other, and their interference can be constructive or destructive. Following this phenomenon, maxima and minima occur in the transmission spectrum, and its diagram shows the oscillating behavior.

Figure 2b shows the transmittance spectrum of the films after annealing at 400 °C. According to this figure, by increasing the deposition rate, the absorption edge has been shifted towards a longer wavelength. This change in the transmittance spectrum can be

related to a change in the structural nature of the films [20]. The absorption edge is located in the ultraviolet region for all samples. As shown in Fig. 2b, transmission in the visible region is uniform due to heat treatment, and its value is more than %83 for all samples in this region. According to the figure, its average value in the visible wavelength region for the deposition rates of 0.2, 0.4, 0.6 and 0.8 nm/s, is %83.5, %90.5, %93.1 and %86.9, respectively.

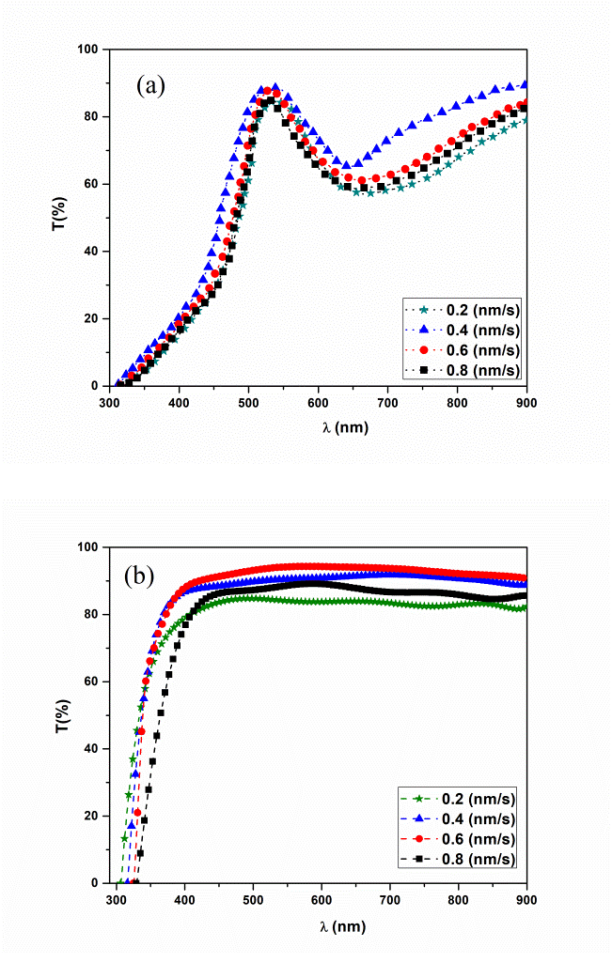

Figure 2. Plot of the transmission as a function of wavelength with different deposition rates (a) before annealing, (b) after annealing at 400 °C.

In general, the transparency of the films has improved after the annealing process. The reflection of the samples after the annealing process is shown in Fig. 3. As can be seen, the amount of the reflection in the visible region is less than %20, which is due to the dispersion and more transmission of these films in this region [21].

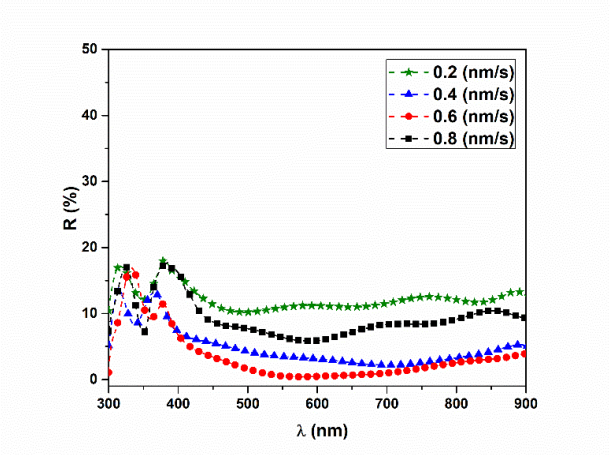

Figure 3. Plot of reflection of ZnSe thin films deposited at different deposition rates after annealing at 400 °C.

The absorption coefficient ($\alpha(\lambda)$) can be obtained from reflection and transmission data as follows [22]:

$$\alpha = \frac{1}{d}\ln\left(\frac{(1-R)^2}{T}\right), \quad (1)$$

Where α, d, R, and T are the absorption coefficient, film thickness, reflectance and transmittance, respectively.

To further investigate the optical properties of the samples, the extinction coefficient (k) and refractive index (n) were calculated. The extinction coefficient (k) is obtained as follows:

$$k = \frac{\alpha\lambda}{4\pi}. \quad (2)$$

In this equation λ is the photon wavelength. The extinction coefficient as a function of wavelength is shown in Fig. 4a. According to this plot, the extinction coefficient of the samples in the ultraviolet region is higher than its value in the visible region, which indicates that the films are transparent in the visible region. For all samples, the extinction coefficients are almost constant and uniform, which shows that the annealing of the samples are well done and the samples are more regularized after heating [23].

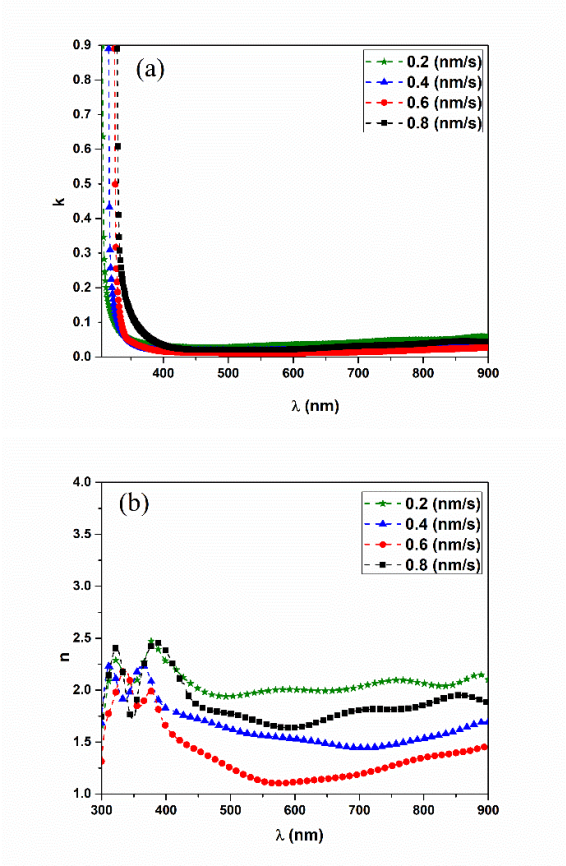

Figure 4. (a) Extinction coefficient, and (b) refractive index versus wavelength for the samples with different deposition rates, after annealing at 400 ℃.

The refractive index is one of the essential properties of an optical material because the refractive index is attributed to the electron polarization of the ions and the local field within the material [24]. The refractive index (n) was calculated using Eq. (3), which is written as a function of reflection (R) and extinction coefficient (k):

$$n = \left(\frac{1+R}{1-R}\right) + \sqrt{\left(\frac{4R}{(1-R)^2} - K^2\right)}. \quad (3)$$

The variation of refractive index versus wavelength are shown in Fig. 4b. Their values at the absorption edge with deposition rates of 0.2, 0.4, 0.6 and 0.8 nm/s are 2.09±0.17, 2.11±0.13, 2.13±0.09 and 2.14±0.15, respectively. The high refractive index for the ZnSe film makes it suitable for use in optoelectronic applications [3]. Furthermore, according to Fig. 4b, the refractive index at shorter wavelengths has a higher value for all samples, which may be associated with the fundamental band gap absorption [25]. It is observed that for all samples, the refractive index has fluctuated with decreasing wavelength, which can be applied in infrared tools [26].

Table 1: The porosity and optical parameters of the ZnSe thin films prepared at different deposition rates

Deposition rate (nm/s)	n (at absorption edge)	Porosity	E_g (eV)
0.2	2.09±0.17	0.52 ±0.17	3.98±0.01
0.4	2.11±0.13	0.73±0.26	3.86±0.01
0.6	2.13±0.09	0.82±0.26	3.76±0.01
0.8	2.14±0.15	0.65±0.28	3.71±0.01

Deposition rate (nm/s)	ε_2 (λ= 550 nm)	ε_1 (λ= 550 nm)	K (λ= 550 nm)
0.2	0.118±0.017	3.91±0.67	0.030±0.002
0.4	0.055±0.007	2.65±0.41	0.017±0.001
0.6	0.029±0.004	2.10±0.42	0.010±0.001
0.8	0.074±0.009	3.16±0.52	0.021±0.001

The refractive index of the films has a direct effect on the porosity of the films. The porosity of the films is obtained by using Eq. (4) [27]:

$$\text{porosity} = \left(1 - \frac{n^2-1}{n_d^2-1}\right). \quad (4)$$

In this equation, n is the refractive index, n_d is the refractive index of pore-free ZnSe where its value is 2.67 [9]. The results of the calculations are presented in Table 1. The porosity of the sample with a deposition rate of 0.6 nm/s is the highest porosity of the films which can show a smaller packing density in this sample. The dielectric constant was calculated in ZnSe thin films according to the following equations:

$$\varepsilon_1 = n^2 - k^2, \quad (5)$$
$$\varepsilon_2 = 2nk. \quad (6)$$

The lower dielectric constant values can lead to induction polarization in material [12]. In the above equations, ε_1 and ε_2 are real and imaginary parts of the dielectric constant, respectively. The variations of the real dielectric constant as a function of wavelength for annealed samples at various deposition rates are shown in Fig. 5. As can be seen, the real dielectric constant with increasing deposition rate up to 0.6 nm/s decreases and thereafter increases.

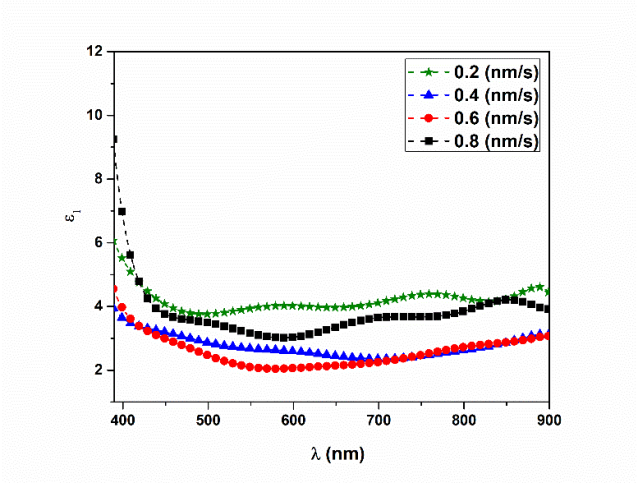

Figure 5. Variation of the real dielectric constant versus the wavelength for samples with different deposition rates.

The values obtained for dielectric constants at 550 nm are shown in Table 1. The real part of the dielectric function reflects the permittivity of the material lattice and the imaginary part is related to the absorption.

In addition, the optical band gap energy was determined based on the derivation of the absorption spectrum fitting (DASF) method. The absorption coefficient ($\alpha(\lambda)$) can be written in terms of λ by the following equation [28]:

$$\alpha(\lambda) = B(hc)^{m-1}\lambda\left(\frac{1}{\lambda}-\frac{1}{\lambda_g}\right)^m, \qquad (7)$$

where λ_g, B, h, c, and m are the wavelengths attributed to the energy gap, a constant, Planck's constant, the velocity of the light, and the optical transition index of charge carrier, respectively. We can substitute $\lambda = \frac{c}{\nu}$ (ν is the light frequency) in Eq. (7) and after some simplifications, we obtain the following equation:

$$\alpha(\lambda)h\nu = B(h\nu - h\nu_g)^m, \qquad (8)$$

and then:

$$\ln(\alpha h\nu) = lnB + m\, ln(h\nu - E_g). \qquad (9)$$

By differentiating both sides of Eq. (9) with respect to $h\nu$ gives:

$$\frac{d\{l\, n(\alpha h\nu)\}}{d(h\nu)} = \frac{m}{(h\nu - E_g)}. \qquad (10)$$

The plot of $\frac{d\{l\, n(\alpha h\nu)\}}{d(h\nu)}$ versus $h\nu$ is shown in Fig. 6. It is clear that this plot has a discontinuity in a certain amount of energy, which is the band gap energy ($h\nu = E_g$). The band gap values of the samples are presented in Table 2. As can be seen, the energy gap decreases from about 3.98±0.01 to 3.71±0.01eV with increasing the deposition rate, which is probably due to the increase of the crystallite size and effect of quantum confinement [29]. The range of optical band gap in our samples is well matched to the optical band gap of ZnSe thin films grown by the chemical bath deposition (CBD) method [30].

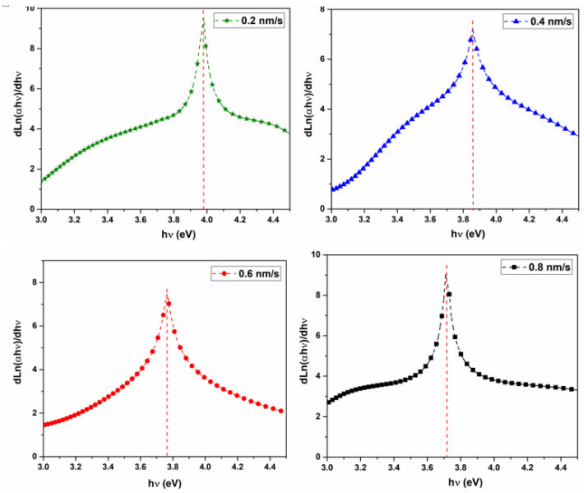

Figure 6. Discontinuity plot of $\frac{d\{l\, n(\alpha h\nu)\}}{d(h\nu)}$ versus $h\nu$ for the ZnSe films deposited at different deposition rates.

The relationship between the refractive index (n) at the absorption edge and the energy band gap of the films can also be investigated according to the Herve–Vandamme model as [31]:

$$n = \sqrt{1 + \left(\frac{13.6}{E_g + 3.47}\right)^2}. \qquad (11)$$

According to this model, n^2 is directly proportional to $(E_g + 3.47)^{-2}$. Fig. 7 shows that the variation of n^2 follows this model well. As can be seen, the refractive index trend at the absorption edge is inversely proportional to the optical band gap trend. Similar behavior is also observed in ZnSe layers fabricated by the chemical bath deposition method (CBD) [30]. It is also well known that the nonlinear optical susceptibility ($\chi^{(3)}$) is inversely related to the energy

band gap and therefore increases with decreasing the energy band gap [32]. According to the literature, materials with higher $\chi^{(3)}$ and lower E_g are suitable options and promising samples in optical device manufacturing and different applications such as fast optical switching devices, optical limiting, and high-speed communication devices [33].

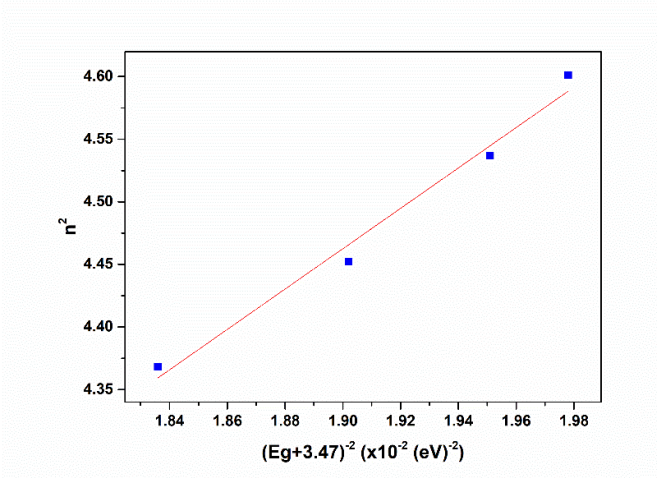

Figure 7. Variations of n^2 as a function of $(E_g + 3.47)^{-2}$.

3.1 Microstructural properties

The structural and microstructural properties of ZnSe thin films, such as the lattice constant, crystallite size, strain, and dislocation density, were also investigated with different deposition rates. In order to specify the mechanisms and determine the structure of these films, the XRD pattern was prepared (see Fig. 8). By studying the XRD analysis of samples, the peaks intensity at the angles of 27.16˚, 45.30˚, and 53.21˚ are related to preferential orientation of the planes (111), (220), and (311), respectively. In addition, by increasing the deposition rate, another peak is created at 72.67˚, which indicates the reflection of the (331) plane. Ion et al. [34] have observed similar peaks for ZnSe films deposited by the Rf-sputtering method. The peaks are in good agreement with JCPDS card No. 37-1463 and the XRD results show that these films crystallize in the cubic structure.

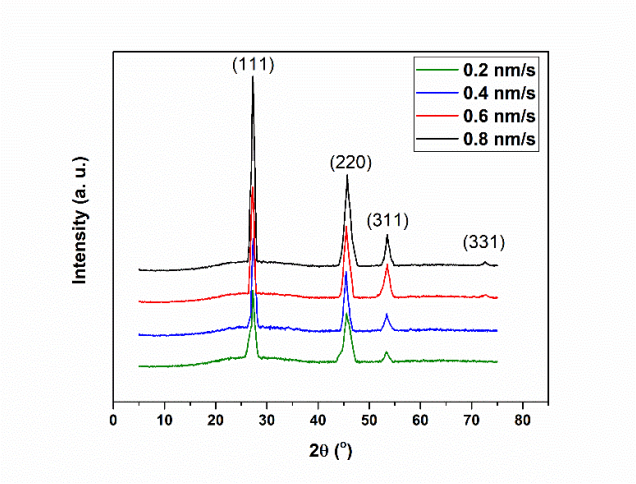

Figure 8. The XRD patterns of the ZnSe samples with different deposition rates.

The crystallite size (D) is also calculated with the help of XRD pattern data using the Williamson-Hall formula from the following equation [35]:

$$\beta \cos\theta = \frac{k\lambda}{D} + 4\varepsilon \sin\theta, \qquad (12)$$

where λ = 1.54056 Å, K is a shape factor which is 0.9 for spherical grains, β is the full width at half maximum (FWHM) in radian, Bragg's diffraction angle (θ) of XRD peak is in degrees, and ε is the strain. The relationship between $\beta \cos\theta$ and $\sin\theta$ for the samples grown at different deposition rates is shown in Fig. 9.

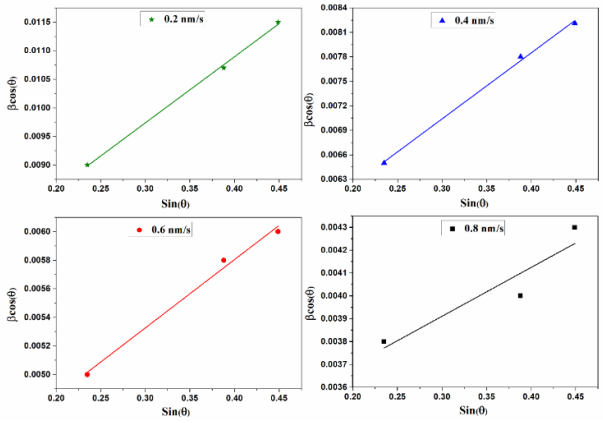

Figure 9. Relationship between $\beta \cos\theta$ and $\sin\theta$ for different samples.

Since a good linear relationship was observed, the strain and crystallite size can be attained from the slope and y-intercept of the linear relationship between

$\beta \cos\theta$ and $\sin\theta$. Also, the lattice constant (a) for the cubic lattice of ZnSe can be obtained from the following equation [30]:

$$a = d\sqrt{h^2 + k^2 + l^2}, \quad (13)$$

where h, k, and l represent the Miller's indexes and d is the lattice spacing. The dislocation density (δ) which is defined as the length of dislocations lines per unit volume of the crystal is calculated from the fallowing relation [36]:

$$\delta = \frac{2\sqrt{3} < \varepsilon^2 >^{\frac{1}{2}}}{b < D >}, \quad (10)$$

where Burgers vector (b) is equal to $\frac{a\sqrt{3}}{2}$. The structural properties of the thin films of ZnSe with four different deposition rates (0.2, 0.4, 0.6, and 0.8nm/s) for the preferential orientation of (111) are given in Table 2.

Table 2: Structural and microstructural properties of ZnSe films with different deposition rates.

Deposition rate (nm/s)	Distance between planes (d) (111) (Å)	Lattice constant (a) (Å)	crystallite size (D) (nm)	Strain (ε) ($\times 10^{-3}$)	Dislocation density (δ) ($\times 10^{-4}$) (nm^{-2})
0.2	3.277±0.063	5.67±0.11	21.6±1.1	2.89±0.04	9.43±0.79
0.4	3.271±0.086	5.66±0.15	28.3±1.4	1.80±0.04	4.49±0.36
0.6	3.265±0.075	5.65±0.13	34.6±1.8	1.14±0.04	2.33±0.25
0.8	3.277±0.092	5.67±0.16	42.9±2.3	0.61±0.02	1.00±0.11

By increasing the deposition rate from 0.2 to 0.6 nm/s, the distance between the planes (111) and the value of the lattice constant decreases and thereafter increases. Among these samples, the sample grown with a deposition rate of 0.6 nm/s is closer to ZnSe bulk lattice constant (5.65 Å). For comparison, the lattice constant values for the samples are in good agreement with the ZnSe thin films grown by the electron beam deposition technique [37].

The dislocation density and strain reduce with the deposition rate. The plot of the dislocation density and the crystallite size versus the deposition rate is shown in Fig. 10. As can be seen, the dislocation density decreases almost linearly by increasing the deposition rate. The crystallite size increases linearly with an increase in the deposition rate.

The results demonstrated that the deposition rate plays an important role in the microstructural properties of ZnSe films, and the crystallinity of the film can be controlled by choosing a suitable deposition rate. A typically SEM image of a ZnSe sample with a thickness of 250 nm and deposition rate of 0.6 nm/s is shown in Fig. 11. According to this image, the average size of grains is about 64 nm (calculated with software), which perfectly confirms the Nano-structure of the sample.

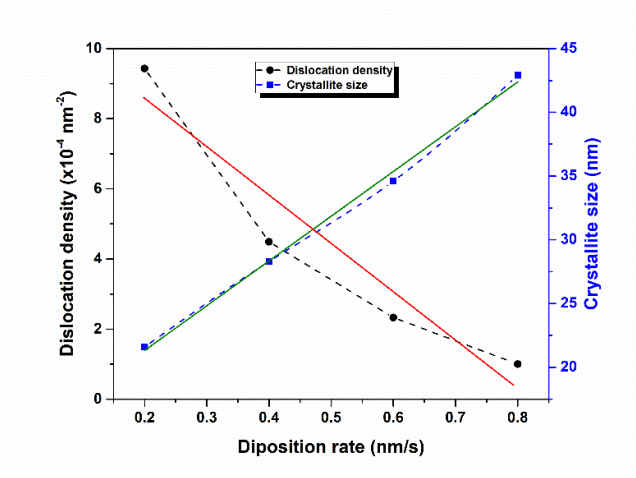

Figure 10. Dislocation density and the crystallite size versus deposition rate.

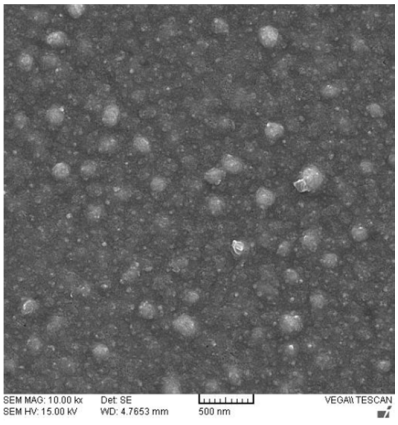

Figure 11. SEM image of the sample with deposition rate of 0.6 nm/s.

4 Conclusions

The ZnSe thin films were deposited on the glass substrate with the thermal evaporation method. The optical parameters of the thin films are generally different from the bulk of the same material. This difference in optical parameters is strongly dependent on the growth conditions of the film. The dependence of the optical and microstructural properties of ZnSe films on the deposition rate was studied and the optical constants of the samples were determined. By increasing the deposition rate between 0.2 and 0.8 nm/s, the refractive index at the absorption edge was changed from 2.09±0.17 to 2.14±0.15. The results showed that the refractive index and band gap energy had an inverse behavior. From the microstructure analysis, it could be concluded that ZnSe films crystallize in a cubic structure, and the dislocation density and crystallite size almost linearly change with the deposition rate. Also, the dislocation density decreased from $(9.43\pm0.79)\times10^{-4}$ to $(1.00\pm0.11)\times10^{-4}$ (nm^{-2}) by increasing the deposition rate. The surface morphology of the films was determined by SEM, which demonstrated the nanostructure of the sample with a deposition rate of 0.6 nm/s. Finally, as a consequence, the deposition rate has a key role in controlling the optical and microstructural properties of ZnSe thin films, and it is necessary for developing a deeper understanding of the performance of devices utilizing these layers.

Acknowledgment

The authors would like to thank the Nanotechnology Research Institute of Shahrekord University for their Laboratory Support.

Conflict of Interest

The authors declare that they have no conflict of interest.

References

[1] L. G. Valluzzi, M. G. Valluzzi, G. N. Darriba, M. Meyer, and L. C. Damonte, “Surfactant and Dopant Addition Effect on Optical and Structural Properties of ZnSe (Te) Nanostructured Semiconductors.” Journal of Alloys and Compounds, **829** (2020) 154488.

[2] M. Imran, A. Saleem, N. A. Khan, A. A. Khurram, and N. Mehmood, “Amorphous to Crystalline Phase Transformation and Band Gap Refinement in ZnSe Thin Films.” Thin Solid Films, **648** (2018) 31.

[3] E. R. Sharaf, I. S. Yahia, M. I. Mohammed, H. Y. Zahran, and E. R. Shaaban, “High Refractive Index and Third-Order Nonlinear Optical Susceptibility of Nanostructured ZnSe/FTO Thin Films: Towards Smart Multifunctional Optoelectronic Materials.” Physica B: Condensed Matter, **602** (2021) 412595.

[4] F. Yao, X. Zhou, and A. Xiong, “Tunable Electronic and Optical Properties of Two-Dimensional ZnSe/AlAs van Der Waals Heterostructure.” Applied Physics A, **126** (2020) 1.

[5] H. H. Yudar, S. Pat, Ş. Korkmaz, S. Özen, and V. Şenay, Zn/ZnSe Thin Films Deposition by RF Magnetron Sputtering, Journal of Materials Science: Materials in Electronics, **28** (2017) 2833.

[6] S. Chuhadiya, R. Sharma, S. L. Patel, S. Chander, M. D. Kannan, and M. S. Dhaka, Thermal Annealing Induced Physical Properties of ZnSe Thin Films for Buffer Layer in Solar Cells, Physica E: Low-Dimensional Systems and Nanostructures, **117** (2020) 113845.

[7] T. D. Lee and A. U. Ebong, A Review of Thin Film Solar Cell Technologies and Challenges, Renewable and Sustainable Energy Reviews **70** (2017) 1286.

[8] H. I. Elsaeedy, A. A. Hassan, H. A. Yakout, and A. Qasem, “The Significant Role of ZnSe Layer Thickness in Optimizing the Performance of ZnSe/CdTe Solar Cell for Optoelectronic Applications.” Optics & Laser Technology, **141** (2021) 107139.

[9] Q. Zhang, H. Li, Y. Ma, and T. Zhai, “ZnSe Nanostructures: Synthesis, Properties and Applications.” Progress in Materials Science, **83** (2016) 472.

[10] S. E. Al Garni and A. F. Qasrawi, "Absorption and Optical Conduction in InSe/ZnSe/InSe Thin Film Transistors." Functional Materials Letters, **9** (2016) 1650019.

[11] S. Ning, G. Feng, H. Zhang, W. Zhang, S. Dai, and S. Zhou, "Fabrication, Structure and Optical Application of Fe2+: ZnSe Nanocrystalline Film." Optical Materials, **89** (2019) 473.

[12] S. Thirumavalavan, K. Mani, and S. Sagadevan, "A Study of Structural, Morphological, Optical and Electrical Properties of Zinc Selenide (ZnSe) Thin Film." Materials Today: Proceedings, **3** (2016) 2305.

[13] F. M. Tezel and İ. A. Kariper, "Effect of PH on the Structural and Optical Properties of Polycrystalline ZnSe Thin Films Produced by CBD Method." International Journal of Modern Physics B, **33** (2019) 1950024.

[14] R. K. Jain, J. Kaur, A. Khanna, and A. K. Chawla, "Tailoring the Structural, Electrical, Optical and Wettability Properties of ZnSe Films by Oblique Angle Thermal Evaporation." Materials Research Express, **6** (2019) 116451.

[15] M. M. Mezdrogina, A. Y. Vinogradov, Y. V Kozhanova, and E. A. Borsuk, "LED Structures Based on ZnO Films Obtained by RF Magnetron Sputtering for the UV Spectral Range." Technical Physics, **65** (2020) 434.

[16] D. V Savin, T. S. Tomilova, S. V Kurashkin, V. B. Ikonnikov, and E. M. Gavrishchuk, "Photoluminescence and Laser Properties of Active Media Based on ZnSe Doped with Cr, Al, Na from Spray Pyrolysis Deposited Films." Laser Physics Letters, **17** (2020) 125802.

[17] D. D. Hile, H. C. Swart, S. V Motloung, R. E. Kroon, K. O. Egbo, and L. F. Koao, "The Effect of Annealing Time on Zinc Selenide Thin Films Deposited by Photo-Assisted Chemical Bath Deposition." Journal of Physics and Chemistry of Solids, **140** (2020) 109381.

[18] Z. Fan, K. Yaddanapudi, R. Bunk, S. Mahajan, and J. M. Woodall, "Interface Studies of Molecular Beam Epitaxy (MBE) Grown ZnSe–GaAs Heterovalent Structures." Journal of Applied Physics, **127** (2020) 245701.

[19] M. R. A. Bhuiyan, M. A. H. Miah, and J. Begum, "Substrate Temperature Effect on the Structural and Optical Properties of ZnSe Thin Films," Journal of Bangladesh Academy of Sciences, **36** (2012) 233.

[20] K. Ou, S. Wang, G. Wan, M. Huang, Y. Zhang, L. Bai, and L. Yi, "A Study of Structural, Morphological and Optical Properties of Nanostructured ZnSe/ZnS Multilayer Thin Films." Journal of Alloys and Compounds, **726** (2017) 707.

[21] Y. Fang, D. Jayasuriya, D. Furniss, Z. Q. Tang, C. Markos, S. Sujecki, A. B. Seddon, and T. M. Benson, "Determining the Refractive Index Dispersion and Thickness of Hot-Pressed Chalcogenide Thin Films from an Improved Swanepoel Method." Optical and Quantum Electronic, **49** (2017) 1.

[22] G. I. Rusu, M. Diciu, C. Pirghie, and E. M. Popa, "Structural Characterization and Optical Properties of ZnSe Thin Films." Applied Surface Science, **253** (2007) 9500.

[23] Z. K. Heiba, A. A. Albassam, and M. B. Mohamed, "Effect of Zn/S Non-Stoichiometric Ratio on the Structural, Optical and Electronic Properties of Nano-ZnS." Applied Physics A, **126** (2020) 1.

[24] A. A. Akl, "Thermal Annealing Effect on the Crystallization and Optical Dispersion of Sprayed V2O5 Thin Films." Journal of Physics and Chemistry of Solids, **71** (2010) 223.

[25] K. V. Saravanan and K. C. J. Raju, "Quasi-Rapid Thermal Annealing Studies on Barium Strontium Titanate Thin Films Deposited on Fused Silica Substrates." Journal of Alloys and Compounds, **571** (2013) 43.

[26] D. Prakash, E. R. Shaaban, M. Shapaan, S. H. Mohamed, A. A. Othman, and K. D. Verma, "Thickness-Dependent Dispersion Parameters, Energy Gap and Nonlinear Refractive Index of

ZnSe Thin Films." Materials Research Bulletin, **80** (2016) 120.

[27] S. B. Khan, Z. Zhang, and S. L. Lee, "Annealing Influence on Optical Performance of HfO2 Thin Films." Journal of Alloys and Compounds, **816** (2020) 152552.

[28] D. Souri and Z. E. Tahan, "A New Method for the Determination of Optical Band Gap and the Nature of Optical Transitions in Semiconductors." Applied Physics B, **119** (2015) 273.

[29] Y. Jiang and N. Bahlawane, "Effect of Nucleation and Growth Kinetics on the Electrical and Optical Properties of Undoped ZnO Films." The Journal of Physical Chemistry C, **114** (2010) 5121.

[30] R. Khalfi, D. Talantikite-Touati, A. Tounsi, and H. Merzouk, "Effect of Deposition Time on Structural and Optical Properties of ZnSe Thin Films Grown by CBD Method." Optical Materials, **106** (2020) 109989.

[31] P. Herve and L. K. J. Vandamme, "General Relation between Refractive Index and Energy Gap in Semiconductors." Infrared Physics & Technology, **35** (1994) 609.

[32] D. Souri, A. R. Khezripour, M. Molaei, and M. Karimipour, "ZnSe and Copper-Doped ZnSe Nanocrystals (NCs): Optical Absorbance and Precise Determination of Energy Band Gap beside Their Exact Optical Transition Type and Urbach Energy." Current Applied Physics, **17** (2017) 41.

[33] S. Ebrahimi, D. Souri, and M. Ghabooli, "Third Order Non-Linear Optical Susceptibility (χ (3)) and Evaluation of Antibacterial Activity of Cu-Doped ZnSe Nanocrystals Fabricated by Hydro-Microwave Technique." Journal of Cluster Science, **30** (2019) 677.

[34] L. Ion, S. Iftimie, A. Radu, V. A. Antohe, O. Toma, and S. Antohe, "Physical Properties Of Rf-Sputtered Znse Thin Films For Photovoltaic Applications: Influence Of Film Thickness." Proceedings of The Romanian Academy Series A-Mathematics Physics Technical Sciences Information Science, **22** (2021) 27.

[35] D. Nath, F. Singh, and R. Das, "X-Ray Diffraction Analysis by Williamson-Hall, Halder-Wagner and Size-Strain Plot Methods of CdSe Nanoparticles-a Comparative Study." Materials Chemistry and Physics, **239** (2020) 122021.

[36] V. Soleimanian and M. Mojtahedi, "A Comparison between Different X-Ray Diffraction Line Broadening Analysis Methods for Nanocrystalline Ball-Milled FCC Powders." Applied Physics A, **119** (2015) 977.

[37] D. N. Papadimitriou, "Vacuum and Liquid-Phase Processing of ZnSe Buffer-Layer for Chalcopyrite Absorber Based Photovoltaic Technology." ECS Journal of Solid State Science and Technology, **7** (2018) 541.

Journal of Interfaces, Thin films, and Low dimensional systems 4 (1) Summer and Autumn (2020) 357-364

Deposition of TiCrN on silicon substrate using radio frequency magnetron sputtering

Scientific research paper

Samira Nassiri and Eslam Ghareshabani*

Faculty of Physics, Sahand University of Technology, Tabriz, Iran

ARTICLE INFO

Article history:
Received 30 March 2021
Revised 26 August 2021
Accepted 27 August 2021
Available online 30 October 2021

Keywords:
Titanium chromium nitride,
RF magnetron sputtering
Bias voltage
GIXRD
FE-SEM

ABSTRACT

The ternary titanium chromium nitride (TiCrN) thin film on Si (100) substrate without any external temperature was deposited by radio frequency (RF) magnetron sputtering. The substrate was kept at a distance of 35 mm from the target. The growth morphology, crystalline structure, roughness, contact angle, and thickness of the coatings were studied as a function of the input RF power and negative bias voltage. The grazing incident X-ray diffraction (GIXRD) results show that TiCrN diffraction peaks appeared only in samples with substrate bias = -70 V. The surface morphology was investigated by Atomic force microscopy (AFM) and field emission scanning electron microscopy (FESEM). The films change from hydrophilic to hydrophobic with the increase of negative bias voltage. The roughness and contact angle of the samples increase with the decrease in the RF power from 300 W to 200 W. In both cases (a) and (b), the deposition rate increases as a result of increase in the target power.

1 Introduction

Of the physical methods to construct ternary metal nitrides coatings on an appropriate substrate is the physical vapor deposition (PVD) method, that magnetron sputtering method is one of the PVD methods that include direct current (DC) sputtering and radio frequency (RF) sputtering [1, 2]. The physical vapor deposition technique for deposition of hard coatings has developed because of their wide range of applications in industry and research such as machine parts and cutting tools [3]. The thickness of the coating can also be entirely controlled by this method [4].

The binary nitrides coatings such as TiN, CrN, and ZrN are commonly utilized to improve the chemical and mechanical properties like high hardness, low friction coefficient, and good corrosion resistance of materials. Despite their perfect properties, the coatings show insufficient properties for some applications. For example, TiN and CrN coatings are degraded by oxidation during machining process at high temperatures above 600° C and 800° C, respectively [5]. Therefore, in order to suppress this problem, by incorporation additional metals such as Al, Zr, Cr, and V, coatings consisting of ternary mixed phases with improved properties can be obtained. However, the stability of the physical-mechanical features of such coatings under irradiation is inadequately studied which prevents their possible use as radiation-resistant protective coatings [6]. By Comparing with binary nitride hard coatings, the ternary coatings are very flexible due to their performances which may be tailored for various applications [7, 8]. Furthermore, the nanocrystalline structure more easily is created in ternary multi-coatings than binary coatings, because of addition atoms impede the base-phase growing in the

*Corresponding author.
Email address: e.ghareshabani@Gmail.com
DOI: 10.22051/jitl.2021.35578.1052

deposition. Most of the transition ternary metal nitrides such as TiAlN, TiCrN, and AlCrN are multi-phase materials by different PVD techniques [7]. Among these films, the TiCrN thin film because of its excellent features such as high hardness, high temperature oxidation resistance, low friction coefficient, and high chemical wear resistance [9-11] has attracted more attention.

In general, ternary nitride films such as TiAlN [12-15], TiZrN [16, 17], TiVN [9], TiCrN [10] and CrAlN [18-27] were investigated by different techniques. For example, by reactive DC magnetron co-sputtering on a silicon substrate [3], ion beam assisted deposition [28], medium frequency magnetron sputtering [29], cathodic arc deposition [30], arc ion plating [31], and closed – field unbalanced magnetron sputtering [32, 33]. In this study, we deposited the TiCrN thin films on Si (100) substrates by the radio frequency (RF) magnetron sputtering method without any external temperature. We reported effects of the RF power and bias voltage on structural properties, thickness, and surface roughness of thin films.

2 Experimental setup

In this study, the TiCrN thin films on the Si (100) substrate were deposited using RF magnetron sputtering at room temperature. This device (Fig. 1) includes a cylindrical stainless steel chamber, two pumps, a pressure gauge device to control inside of the deposition chamber pressure, and a power supply connected to the deposition chamber. Inside the deposition chamber, there is a Ti-Cr target with 2 inches diameter and a substrate holder that was mounted in the upper part of the chamber.

During the coating process, high purity Ar (99.999 wt %) and N_2 (99.999 wt %) were used as process gases while their flow rates were regulated by mass flow controllers. Since the substrate that we used, the Si (100) has an oxide layer (SiO_2) at its surface, we washed it in hydrofluoric acid (HF) to remove the oxide layer for about one minute. Then, washed the substrate in the ultrasonic bath acetone, ethanol, and distilled water respectively for approximately 10 minutes to remove contaminations and impurities. After cleaning the substrate, it was thoroughly dried and installed at the sample holder. The vacuum chamber was evacuated to base pressure of 10^{-5} mbar using a diffusion pump. Before deposition process, Ar gas was introduced into the vacuum chamber to pre-sputter for 15 min to remove any impurity on the Ti-Cr target. The deposition pressure and the distance between target and substrate were kept at 0.02 mbar and35 mm, respectively. The detailed deposition parameters for the TiCrN thin films on the Si (100) substrate were presented in Table 1. All the deposition processes were carried out at an ambient temperature. All the samples were deposited for 1 h.

Table 1. The deposition parameters for the TiCrN thin films on the Si (100) substrate.

	Sample Number	Base pressure (mbar)	Power (W)	Bias voltage (V)	Ar/N_2 Ratio	Deposition time (min)	Working pressure (mbar)
(a)	1	10^{-5}	300	-	1	100	0.02
	2	10^{-5}	250	-	1	100	0.02
(b)	3	10^{-5}	300	-70	1	100	0.02
	4	10^{-5}	250	-70	1	100	0.02

In this article, we report the synthesis of TiCrN thin films using the radio frequency (RF) magnetron sputtering method. The structural properties of the deposited thin films were evaluated using grazing incidence X-ray diffractometer (GIXRD; Philips X'pert PW1730, Netherlands) analysis equipped with a Cu Kα X-radiation (40 kV, 40 mA, 0.15406 nm), step size of 0.05°, and count time of one second per step. Field emission scanning electron microscopy (FESEM; FEI ESEM QUANTA 200) equipped with an EDX analysis working at an acceleration voltage of 12 kV was provided to analyze the morphological properties and the chemical composition of the samples.

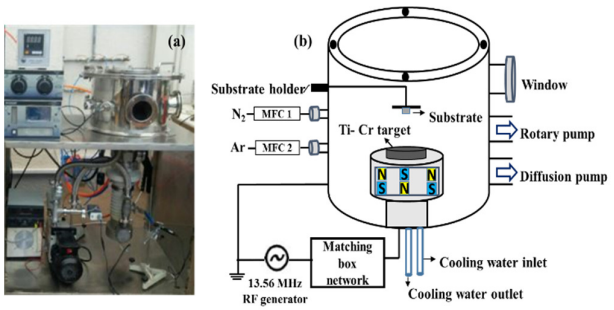

Figure 1. (a) RF magnetron sputtering device and (b) A scheme from inside this device.

The roughness of the samples was obtained using an atomic force microscope (AFM; Bruker, Billerica, USA) with a scan size of 5×5 μm^2 and a scan rate of 1

Hz. The wettability of the surface of the coatings was also evaluated by measuring the contact angle of deionized water on the specimens using a contact angle measurement instrument.

3 Results and discussion

3.1 GIXRD analysis

Figure 2 shows the results of GIXRD patterns of the TiCrN thin films deposited on Si (100) substrates for the input power of 250 W (samples 2 and 4). In these patterns, four compounds, including TiCrN, TiN, Ti_2N, and CrN are seen. In sample 2, the pattern exhibits the diffraction peaks associated with CrN, Ti_2N, and Si. The diffraction peaks 2Θ =25° (Powder Diffraction Patterns: 96-110-0032), 37.50, 43.6^0 and 63.4^0 (Powder Diffraction Patterns: 96-100-8957) are related to Ti_2N (110), CrN (111), CrN (200) and CrN (220), respectively. The diffraction peaks 2Θ = 33^0 and 45.1^0 are related to Si (211) and Si (400), respectively. In sample 4, the pattern exhibits the diffraction peaks related to TiCrN, TiN, CrN, and Si. Considering the TiN (200) at diffraction angle 2Θ = 42.5^0, CrN and Ti_2N peaks, it is observed that the TiCrN (200) and TiCrN (220) peaks are in the range of these compounds [3,30,32].

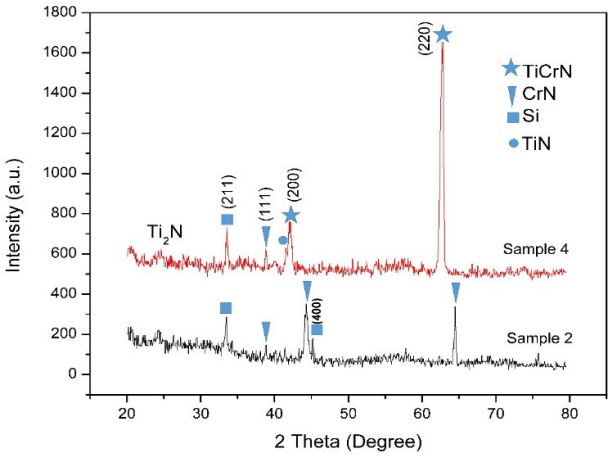

Figure 2. GIXRD patterns of samples 2 and 4 (input power of 250 W).

Figure 3 shows the results of GIXRD patterns of the TiCrN thin films deposited on Si (100) substrates for the input power of 300 W (samples 1 and 3). In sample 1, CrN (111), TiN (200) and TiN (220) compounds and Si (211), and in sample 3, CrN (111), TiCrN (200), Ti_2N (110), Si (002) and TiCrN (220) compounds are seen. When the bias voltage increases from 0 V to -70 V, two phases related to TiCrN are observed. The emergence of these new induced phases can be due to the fact that the energy and flux of the ions are increased. As a result, a large number of target ion species arrived on the growing film that lead to the stoichiometry changes at the film to form a new phase TiCrN. Also, thin film thickness and the intensity of TiCrN (220) diffraction peak decrease as the RF power increases from 250 W in sample 4 to 300 W in sample 3. This can be attributed to the etching effect.

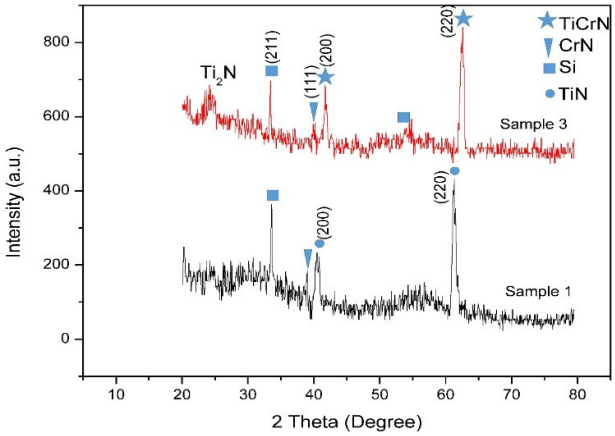

Figure 3. GIXRD patterns of samples 1 and 3 (input power of 300 W).

3.2 FESEM and EDS Analysis

In this study, the ternary nitride nanostructured TiCrN thin films were deposited successfully on Si (100) substrates at two cases: (a) without any bias voltage; (b) with a bias voltage = -70 V with the same deposition parameters. The field emission scanning electron microscopy micrographs are shown in Fig. 4. The morphology of all samples shows an entirely homogeneous and uniform surface of the TiCrN thin films. By comparing the samples without bias and samples with bias voltage, we observe that for the samples with bias voltage, the grain size becomes larger while the shape of the particles change. By comparing the input power, we see that as the input power increases in both cases (a) and (b), the grain size becomes smaller and the particle agglomeration increases.

From the cross-sectional FE-SEM images, as shown in Fig. 5, it turns out that the thickness of the coating in samples without bias voltage is greater than

the bias voltage samples. We observe that as the input power increases in both cases (a) and (b), the coating

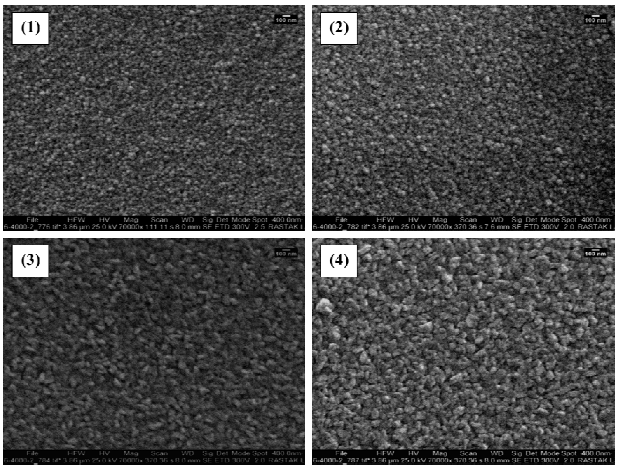

Figure 4. FE-SEM micrographs of the TiCrN thin films.

thickness increases. With increasing the input power from 250 W to 300W, the coating thickness increases from 662 nm to 782 nm in case of without any bias voltage, and from 599 nm to 719 nm in case of with bias voltage. Also, by comparing (a) and (b) samples, we observed a decrease in coating thickness in the samples with a bias voltage.

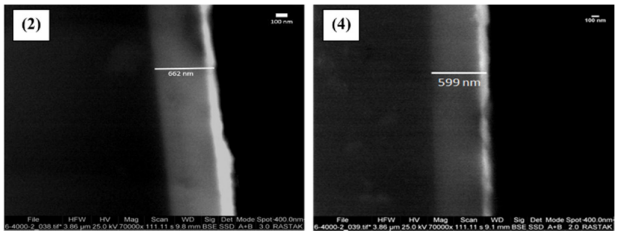

Figure 5: Cross-sectional FE-SEM morphology of the TiCrN thin films for samples 2 and 4.

According to results of the EDS analysis, it is observed that under the same conditions, in the sample without the bias voltage, more atoms of titanium, chromium, and nitrogen are deposited on the substrate. By comparing the input power, we observe that with increasing the input power in both cases, the number of atoms deposited on the substrate increases. Figure 6 shows a typical EDS spectrum and atomic percentages of Ti, Cr, N, and Si for sample 2.

In Fig. 7, the distribution of each of the atoms is shown, which is taken by mapping analysis. Images represent the successful deposition of all atoms on the substrate. Also, line scan analysis results show the successful deposition of TiCrN thin films on the Si (100) process. This analysis exhibit that with approaches to the sample surface, the presence of Ti, Cr, and N atoms increase. The images for this analysis is shown in Fig. 8.

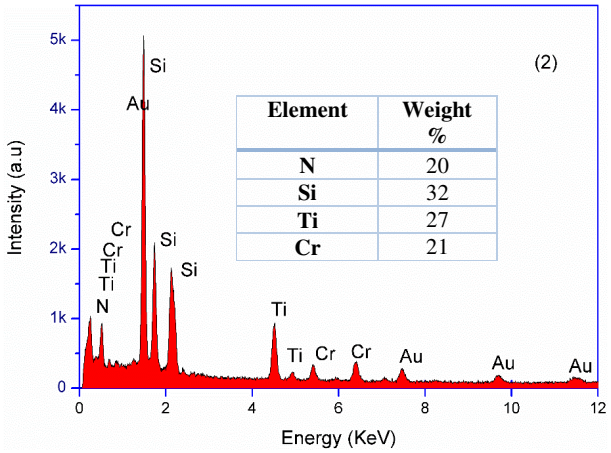

Element	Weight %
N	20
Si	32
Ti	27
Cr	21

Figure 6: Typical EDS spectrum of the sample 2.

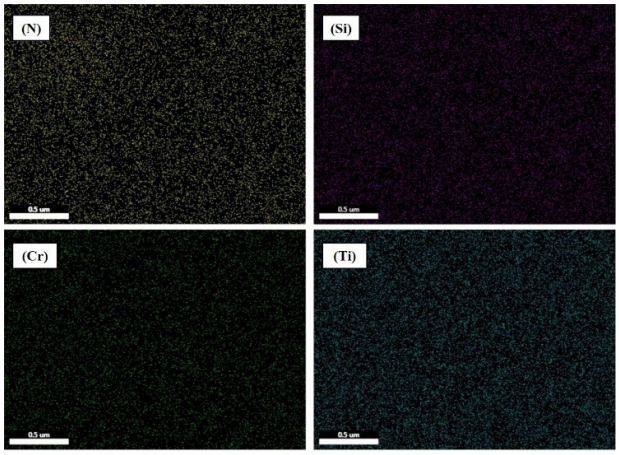

Figure 7: Typical elemental mapping analysis of nitrogen, silicon, chromium, and titanium on the surface of sample 2.

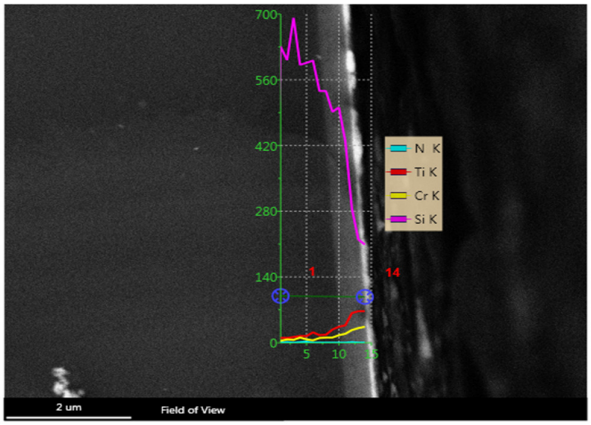

Figure 8. Line scan analysis image of TiCrN thin films related to sample 2.

3.3 AFM results

Atomic force microscopy (AFM) images of TiCrN thin films are shown in Fig. 9 (Fig. 9A: 2D and Fig. 9B: 3D images). In this study, the AFM in contact mode is used to scan the area of 5 µm ×5 µm.

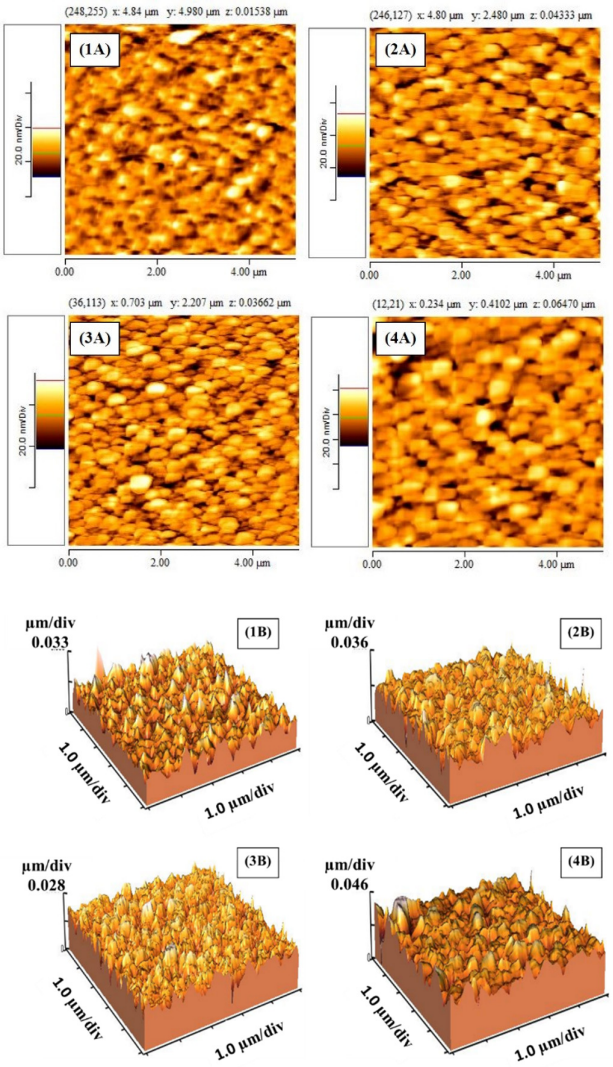

Figure 9. (A) 2D-AFM images of the samples deposited and (B) 3D-AFM images of the samples deposited.

With increasing the input power, we observe that the root mean square (RMS) roughness and average roughness (Ra) values of TiCrN thin films decreases. in case (a), by increasing the input power from 250 W to 300 W, the RMS values decrease from 5.57 nm to 4.70 nm and average roughness values decrease from 4.35 nm to 3.63 nm. In case of (b), by increasing the input power from 250 W to 300 W, the RMS values decrease from 7.86 nm to 6.55 nm and average roughness values decrease from 5.98 nm to 5.13 nm. By comparing the samples without bias voltage and samples with a bias voltage, we observe that the samples without bias voltage have lower RMS. It can be seen (Fig. 5) that the thickness of the film decreases with a bias voltage. An increase in the substrate bias voltage causes an increase in the flux and energy of the ions bombardment of the substrate surface. The atoms etch the film, penetrate, will be trapped, and lead to film growth defects. Therefore, it increases the roughness of the films.

As the RF power increases from 250W to 300 W, the roughness of the film decreases. The ionization degree of target materials is small at lower RF power. The relative concentration of large-mass species is more than that of small-mass species. Meanwhile, at low RF power, the ion kinetic energy is low, the species reaching the substrate or the film surface are mainly larger-mass species. These larger-mass species are appropriate to form clusters and aggregates in the gas phase before deposition. Such clusters form preferentially on the surface. It leads to more defects such as the asperities on the film surface. The roughness values of the films deposited are given in Table 2.

Table 2: Roughness parameters of deposited TiCrN thin films.

Sample number	RMS (nm)	R_a (nm)
1	4.70	3.63
2	5.57	4.35
3	6.55	5.13
4	7.86	5.98

3.4 Contact angle results

We measured the contact angle of TiCrN thin films using the sessile drop method, before and after deposition. As seen in Fig. 10, before the deposition process, our Si substrate had a contact angle value of fewer than 90 degrees (~ 61.7^0) and it is a hydrophilic surface. After the deposition process, the contact angle of all samples increased. The interesting point is the relationship between the roughness and the contact angle values of the coatings. As the roughness of the surfaces increases, their contact angle increases, and vice versa. The results show that the contact angle of the samples with a bias voltage is more than the samples without any bias voltage. This means that by

giving the bias voltage to the substrate, the surface of the coating is being hydrophobic, whereas it has previously been hydrophilic. On the other hand, with increasing the input power in both sets of samples, the contact angle decreases. As can be seen the Fig. 10, sample 4 has the highest contact angle value and is more hydrophobic than the rest of the samples.

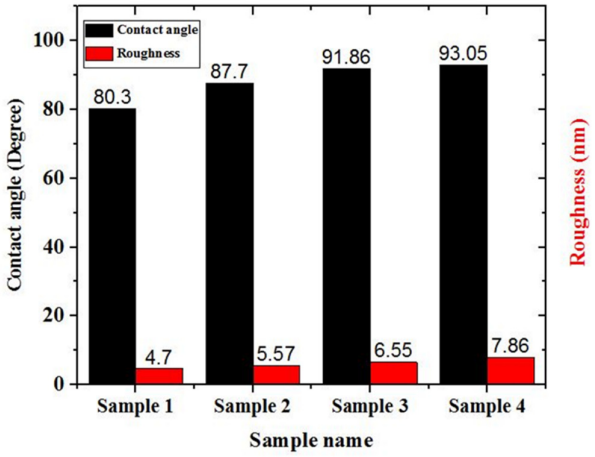

Figure 10. Variation of sample contact angle with different samples.

The water contact angle depends on the surface roughness, while can be explained by two models: Wenzel and Cassie-Baxter models [34]. Based on the Cassie-Baxter model, when the roughness of the surface increase, the proportion of air pocket increases correspondingly, and the contact angle should increase in the order of surface roughness from small to large. This is consistent with our results.

4 Conclusions

The ternary nitride TiCrN nanostructured coatings were deposited successfully on Si (100) substrate at room temperature using the RF magnetron sputtering method. The effects of the input RF power and bias voltage on the structure and properties of the TiCrN coatings has been studied. The results of the GIXRD analysis show that the TiCrN thin film peaks appeared in samples with substrate bias=-70 V. The intensity of TiCrN (220) diffraction peak decreases as the RF power increases from 250 W in sample 4 to 300 W in sample 3. When the bias voltage increased from 0 V to -70 V, two phases related to TiCrN were observed. The FESEM images demonstrate quite a uniform surface with the homogenous distribution of the grain sizes. The cross-sectional FESEM images show that the thickness of the film decreases with a bias voltage. With increasing the input RF power from 250 W to 300 W without bias voltage, deposition rate increases from 11 nm/min to 13 nm/min. As the RF power increases from 250W to 300 W, the roughness of the film decreases. The contact angle of the samples with bias voltage was more than the samples without voltage.

References

[1] A. K. Tareen, G. S. Priyanga, S. Behara, T. Thomas, M. Yang, "Mixed ternary transition metal nitrides: A comprehensive review of synthesis, electronic structure, and properties of engineering relevance. Progress in Solid State Chemistry, **53** (2019) 1-26.

[2] P. J. McGinn, "Thin-Film Processing Routes for Combinatorial Materials Investigations—A Review." ACS Combinatorial Science, **21** (2019) 501.

[3] N. Witit-Anun, A. Teekhaboot, "Effect of Ti Sputtering Current on Structure of TiCrN Thin Films Prepared by Reactive DC Magnetron Co-Sputtering." Key Engineering Materials, **675-676** (2016) 181.

[4] N. Bensalah, F.Z. Kamand, N. Mustafa, M. Matalqeh, "Silicon–Germanium bilayer sputtered onto a carbon nanotube sheet as anode material for lithium–ion batteries." Journal of Alloys and Compounds, **811** (2019) 152088.

[5] B. Navinšek, P. Panjan, A. Cvelbar, "Characterization of low temperature CrN and TiN (PVD) hard coatings." Surface and Coatings Technology, **74-75** (1995) 155.

[6] S. Kislitsin, I. Gorlachev, V. Uglov, "Effects of Irradiation with Low-Energy and High-Energy Krypton Ions on the Structure of TiCrN Coatings." Acta Physica Polonica A, **128** (2015) 818.

[7] S. Chen, D. Luo, G. Zhao, Investigation of the Properties of TixCr1-xN Coatings Prepared by Cathodic Arc Deposition, Physics Procedia, **50** (2013) 163.

[8] C. Mendibide, P. Steyer, J. Fontaine, P. Goudeau, "Improvement of the tribological behaviour of PVD nanostratified TiN/CrN coatings — An explanation." Surface and Coatings Technology, **201** (2006) 4119.

[9] T. Deeleard, S. Chaiyakun, A. Pokaipisit, P. Limsuwan, "Effects of Vanadium Content on Structure and Chemical State of TiVN Films Prepared by Reactive DC Magnetron Co-Sputtering." Materials Sciences and Applications, **4** (2013) 556.

[10] H. S. M. J. G. Han, H. M. Lee, L. R. Shaginyan, "Microstructure and mechanical properties of Ti–Ag–N and Ti–Cr–N superhard nanostructured coatings." Surface and Coatings Technology, **743** (2003) 174738

[11] H. S. Choi, D. H. Han, W. H. Hong, J. J. Lee, "(Titanium, chromium) nitride coatings for bipolar plate of polymer electrolyte membrane fuel cell." Journal of Power Sources, **189** (2009) 966.

[12] A. Buranawong, N. Witit-anun, S. Chaiyakun, A. Pokaipisit, P. Limsuwan, "The effect of titanium current on structure and hardness of aluminium titanium nitride deposited by reactive unbalanced magnetron co-sputtering." Thin Solid Films, **519** (2011) 4963.

[13] X. Z. Ding, A.L.K. Tan, X.T. Zeng, C. Wang, T. Yue, C.Q. Sun, "Corrosion resistance of CrAlN and TiAlN coatings deposited by lateral rotating cathode arc." Thin Solid Films, **516** (2008) 5716.

[14] A. Obrosov, R. Gulyaev, M. Ratzke, A. Volinsky, S. Bolz, M. Naveed, S. Weiß, "XPS and AFM Investigations of Ti-Al-N Coatings Fabricated Using DC Magnetron Sputtering at Various Nitrogen Flow Rates and Deposition Temperatures." Metals, **7** (2017) 52.

[15] A. Z. Ait-Djafer, N. Saoula, H. Aknouche, B. Guedouar, N. Madaoui, "Deposition and characterization of titanium aluminum nitride coatings prepared by RF magnetron sputtering." Applied Surface Science, **350** (2015) 6.

[16] S. Chinsakolthanakorn, A. Buranawong, S. Chiyakun, P. Limsuwan, Effects of Titanium Sputtering Current on Structure and Morphology of TiZrN Films Prepared by Reactive DC Magnetron Co-Sputtering, Materials Sciences and Applications, **4** (2013) 689.

[17] V. V. Uglov, D. P. Rusalski, S. V. Zlotski, A. V. Sevriuk, G. Abadias, S. B. Kislitsin, K. K. Kadyrzhanov, I. D. Gorlachev, S. N. Dub, "Stability of Ti–Zr–N coatings under Xe-ion irradiation." Surface and Coatings Technology, **204** (2010) 2095.

[18] J. Lin, B. Mishra, J. J. Moore, W. D. Sproul, J. A. Rees, "Effects of the substrate to chamber wall distance on the structure and properties of CrAlN films deposited by pulsed-closed field unbalanced magnetron sputtering (P-CFUBMS)." Surface and Coatings Technology, **201** (2007) 6960.

[19] X. S. Miao, Y. C. Chan, E. Y. B. Pun, "Protective AlCrN film for organic photoconductors." Thin Solid Films, **324** (1998) 180.

[20] X. Chen, Y. Xi, J. Meng, X. Pang, H. Yang, "Effects of substrate bias voltage on mechanical properties and tribological behaviors of RF sputtered multilayer TiN/CrAlN films." Journal of Alloys and Compounds, **665** (2016) 210.

[21] Q. M. Mehran, A. R. Bushroa, M. A. Fazal, M. M. Quazi, "Scratch adhesion characteristics of PVD Cr/CrAlN multilayer coating deposited on aerospace AL7075-T6 alloy." Pigment & Resin Technology, **44** (2015) 364.

[22] Q. M. Mehran, A. R. Bushroa, M. A. Fazal, "Evaluation of CrAlN multilayered coatings deposited by PVD magnetron sputtering." Journal of Adhesion Science and Technology, **29** (2015) 2076.

[23] C. Zhuang, Z. Li, S. Lin, "Effect of annealing process on atomic-scale structure, dislocation and mechanical behaviour of nano-grained Al–Cr–N thin films." Surface Engineering, **33** (2016) 204.

[24] Y. Lv, L. Ji, X. Liu, H. Li, H. Zhou, J. Chen, "The structure and properties of CrAlN films deposited by mid-frequency unbalanced magnetron sputtering at different substrate bias duty cycles." Surface and Coatings Technology, **206** (2012) 3961.

[25] X. Wang, L. S. Wang, Z. B. Qi, G. H. Yue, Y. Z. Chen, Z. C. Wang, D. L. Peng, "Investigation on the structure and properties of AlxCr1−xN coatings deposited by reactive magnetron co-sputtering." Journal of Alloys and Compounds, **502** (2010) 243.

[26] M. Fellah, L. Aissani, M. A. Samad, S. Mechacheti, M. Z. Touhami, A. Montagne, A. Iost, "Characterisation of R.F. magnetron sputtered Cr-N, Cr-Zr-N and Zr-N coatings." Transactions of the IMF, **95** (2017) 261.

[27] S. Khamseh, H. Araghi, "A study of the oxidation behavior of CrN and CrZrN ceramic thin films prepared in a magnetron sputtering system." Ceramics International, **42** (2016) 9988.

[28] S. M. Aouadi, K. C. Wong, K. A. R. Mitchell, F. Namavar, E. Tobin, D. M. Mihut, S. L. Rohde, "Characterization of titanium chromium nitride nanocomposite protective coatings." Applied Surface Science, **229** (2004) 387.

[29] G. A. Zhang, P. X. Yan, P. Wang, Y. M. Chen, J. Y. Zhang, "The structure and tribological behaviors of CrN and Cr–Ti–N coatings." Applied Surface Science, **253** (2007) 7353.

[30] C. H. Hsu, C. K. Lin, K. H. Huang, K. L. Ou, "Improvement on hardness and corrosion resistance of ferritic stainless steel via PVD-(Ti,Cr)N coatings." Surface and Coatings Technology, **231** (2013) 380.

[31] M. Huang, Z. Chen, M. Wang, Y. Li, Y. Wang, "Microstructure and properties of TiCrN coatings by arc ion plating." Surface Engineering, **32** (2016) 284.

[32] Q. Wang, F. Zhou, J. Yan, "Evaluating mechanical properties and crack resistance of CrN, CrTiN, CrAlN and CrTiAlN coatings by nanoindentation and scratch tests." Surface and Coatings Technology, **285** (2016) 203.

[33] S. Y. Lee, G. S. Kim, J. H. Hahn, "Effect of the Cr content on the mechanical properties of nanostructured TiN/CrN coatings." Surface and Coatings Technology, **177-178** (2004) 426.

[34] W. M. Sigmund, S. H. Hsu, Cassie–Baxter Model, in: E. Drioli, L. Giorno (Eds.) Encyclopedia of Membranes, Springer Berlin Heidelberg, Berlin, Heidelberg (2016) 310-311.